An Approximate Analytical Model for the Discharge Performance of a Primary Zinc/Air Cell

By

Leo J. White

A thesis
Submitted to the faculty
of the

WORCESTER POLYTECHNIC INSTITUTE

In partial fulfillment of the requirements for the degree of
Master's of Science
In
Chemical Engineering
by

_____
January 12, 2005

Approved:

_____
Dr. Ravindra Datta, Department Head

ABSTRACT

The characteristics of a Zinc/Air (Zn/Air) primary cell are discussed. In addition, current technologies and the corresponding electrical performance are introduced. The basic principles of operation of a Zn/Air primary cell are discussed, focusing on the anode, cathode, and electrolyte. Basic kinetic and transport expressions are developed for the two main components of the cell: the anode and cathode compartments, based on which an overall formula for the cell polarization is developed. Input parameters are selected and approximated where possible to observe the model's ability to predict potential versus current density. Time-dependent anode performance is accomplished through the use of the shrinking core reaction model for the discharge of the zinc particles. The time-dependent dimensionless radius of the zinc particle (ξ) is then used in conjunction with the developed transport and kinetic expressions for the prediction of the overall cell performance as a function of time. Plots of cell voltage prediction versus time and percent capacity versus time are presented. The simulations indicate an adequate approximate analytic model valid for a variety of drain rates corresponding to current hearing instrument devices in the market.

ACKNOWLEDGEMENTS

I would first like to thank Professor Ravindra Datta for his guidance and support throughout the course of this thesis. Our discussions throughout the course of this endeavor lead to significant insight into the mathematical derivations that have made this thesis successful. Without his assistance the completion of this thesis would have been impossible and for this help I am indebted.

There have been many individuals who have given significant emotional support and encouragement. My parents have played an instrumental role in my academic pursuits from my childhood and through adulthood. The foundations that they have instilled in me have lead me down this path and are the sole reason for my success. Their unyielding belief that I can accomplish whatever I set my mind to has helped me to make it through the tough times. I would also like to acknowledge my friends, Dan Hebert, Frank Dunn, Chris Kingston, Chris Cheverie, Bob Hutchinson, Matt Woodcock, Fabien Ramat, and Pascal Eyries, for their support and nights of relaxation that prevented me from going insane.

Without the support of my employer, Duracell - A Gillette Co., and my direct management, the pursuit of my Master's Degree would not have been possible. I am grateful for the flexibility of working hours afforded to me by Sean Sargeant, Mike Garris, and Erik Weenink when I first began this journey. This flexibility has transcended on to David Pappas and Steven Specht, for which I am grateful.

Many individuals within the Duracell organization have shown a great interest in this work and have contributed in many ways. Dr. Huk Cheh, Matt Hull, Keith Buckle, and Dan Gibbons have had significant input via theoretical and technical discussions, as

well as many reviews of draft versions of this work. I would like to thank Dmitriy Dergachev for his assistance in completing various figures through his vast artistic skill. Sue Allsop, Maceij Majewski, Christopher Brown, Sherri Davies, Max Uditnarian, and the Duracell Life and Abuse Test Staff have been instrumental in allowing the collection of physical and performance data, without which this work would not be complete.

Finally, the attention afforded to me by the Gillette Legal Department has been excellent. Without their guidance and direction, the publication of this work and my subsequent completion of degree requirements would not have been possible. I am especially grateful for the guidance given by our late friend Paul I. Douglas. You will be missed.

TABLE OF CONTENTS

LIST OF FIGURES

LIST OF TABLES

LIST OF SYMBOLS

a_i activity of species *I*

A geometric area of membrane-electrode assembly

$c_{i\alpha}$ concentration of species *i* in layer α, mol/cm^3

C specific capacity = Q_t/m_T, C/g or A.s/g

$D^e_{i\alpha}$ effective diffusion coefficient of species *i* in layer α, cm^2/s

$E_{A,\Phi_\circ}$ effective activation energy of $i_{A,0}$ or $\vec{k}^*_{A,\Phi_\circ}$

F Faraday's constant, 96,487 C/eq

i current density, A/cm^2 of geometric electrode area

i_A anodic current density, A/cm^2 of geometric electrode area

$i_{A,L}$ anodic limiting current density, A/cm^2 of geometric electrode area

i_C cathodic current density, A/cm^2 of geometric electrode area

$i_{C,L}$ cathodic limiting current density, A/cm^2 of geometric electrode area

i_0 exchange current density, A/cm^2 of geometric electrode area

$i_{A,0}$ anodic exchange current density, A/cm^2 of geometric electrode area

$i_{C,0}$ cathodic exchange current density, A/cm^2 of geometric electrode area

i^* current density, A/cm^2 of active material surface

i^*_o exchange current density, A/cm^2 of active material surface

$i^*_{A,o}$ anodic exchange current density, A/cm^2 of active material surface

$i^*_{C,o}$ cathodic exchange current density, A/cm^2 of active material surface

k_B Boltzmann constant

k^*_A effective rate constant of overall anode reaction per cm^2 of active area

$\vec{k}^{*}_{A,\Phi_\circ}$ rate constant of anode reaction at equilibrium electrode potential per cm^2 of active area

k^{*}_{C} effective rate constant of overall cathode reaction per cm^2 of active area

$\vec{k}^{*}_{C,\Phi_\circ}$ rate constant of cathode reaction at equilibrium electrode potential per cm^2 of active area

L_α thickness of layer α

m_E electrolyte loading in catalyst layer, g/cm^2 geometric electrode area

m_M active material loading, g/cm^2 geometric electrode area

m_T total cell mass, g/cm^2 geometric electrode area

N_i flux of species i, mol/cm^2 geometric electrode area

P power density, W/cm^2 geometric electrode area

P_{ia} permeability of layer α for species i, $= D_{i\alpha}\kappa_{i\alpha}/L_\alpha$, cm/s

Q_t capacity = $i \times t$, C/cm^2 or $A.s/cm^2$

r_i net rate of reversible reaction i, $= \vec{r}_i - \bar{r}_i$, mol/cm^3 active material particles·sec

$\vec{r}_{io}$ rate of forward reaction under open circuit conditions, mol/cm^3 active material particles·sec

r^{*}_{i} net rate of reversible reaction i, = mol/cm^2 active material areas·sec

r^{*}_{A} net rate of anodic reaction, mol/cm^2 active material area·sec

r^{*}_{C} net rate of cathodic reaction, mol/cm^2 active material area·sec

$r_{\rho 0}$ = reaction rate at open circuit

R universal gas constant, 8.3143 J/mol.K

R_I interfacial resistance, $\Omega \cdot cm^2$

R_α initial radius of unreacted shrinking core of particles of electrode α

$R_{\alpha,0}$ overall radius of particles of electrode α

T temperature, K

V battery potential, $=\phi_{MC}-\phi_{MA}$, V

V_0 open circuit potential, $=\Phi_{o,C}-\Phi_{o,A}$, V

$\overline{V}_i$ partial molar volume of i, cm^3/mol

Greek Letters

$\vec{\alpha}_A$ effective transfer coefficient of overall anode reaction = ½

$\vec{\alpha}_A$ effective transfer coefficient of overall cathode reaction = ½

$\nu_{\rho i}$ stoichiometiric coefficient of species i in reaction ρ

$\nu_{\rho e^-}$ stoichiometiric coefficient of electrons in reaction ρ

η overpotential, $=\Phi-\Phi_o$, V

η_A anodic overpotential, V

η_C cathodic overpotential, V

$\kappa_{i\alpha}$ partition coefficient of species i in layer α, $=(c_{i\alpha}/c_{iG})_{\text{eq}}$

φ_I fraction of accessible catalyst surface participating in electrocatalysis

φ_M fraction of metal crystallite surface that is accessible

Φ electrode potential, V

Φ_o equilibrium electrode potential, V

Φ_o^o standard equilibrium electrode potential for unit activities, V

ϕ inner potential, V

γ_M roughness factor, cm^2 active material/cm^2 geometric electrode area

ρ_M active material density, g/cm^3

σ effective conductivity of electrolyte, S/cm

τ_α tortuosity factor for porous layer α

ε_α porosity for porous layer α

ξ_α dimensionless core radius in of electrode α, = $R_\alpha/R_{\alpha,0}$

Subscripts and Superscripts

0 open circuit conditions, dry membrane, reference

A layer A (anode material, Zn)

B layer B (separator layer)

C layer C (cathode material, O_2)

i species *i*

E electrolyte

F electronic filler

M active electrode material

P polymer binder

ρ reaction ρ

α generic layer

Φ_0 at equilibrium electrode potential

* per cm^2 active material area

CHAPTER I
INTRODUCTION

BACKGROUND

The Zinc/Air (Zn/Air) primary cell is a high energy density cell with a relatively flat discharge voltage and overall low energy cost.[1] In this cell, the cathode reactant is oxygen (O_2) from ambient air that diffuses through a thin cathode structure, after entry through openings in the cell's outer casing, and undergoes catalytic reduction of O_2.[1] To prevent discharge of the cell during storage, the openings in the cell casing are covered with a virtually non-permeable tab. The presence of this tab and the overall relative stability of the chemical system lead to a long shelf life. The assembled cell consequently requires only a small fraction of the internal volume for the cathode structure. The remaining internal volume is available for the anode components and thus a relatively large amount of anode material (primarily zinc) can be placed in the cell. The end result is a relatively high energy density cell.[1]

The electrochemistry of Zn/Air cells involves the oxidation of zinc at the anode in conjunction with the reduction of oxygen at the cathode. The associated chemical reactions in accordance with the dissolution (electrochemical) and precipitation (chemical) of zinc[2] and the alkaline reduction of oxygen[3] are:

$$Zn + 4OH^- \rightarrow Zn(OH)_4^{2-} + 2e^- \quad (1)$$

$$Zn(OH)_4^{2-} \rightarrow ZnO + 2OH^- + H_2O \quad (2)$$

$$\tfrac{1}{2}O_2 + H_2O + 2e^- \rightarrow 2OH^- \quad (10)$$

The overall resulting chemical reaction based upon the half-reactions for the Zn/Air electrochemical cell is:

$$Zn + \tfrac{1}{2}O_2 \rightarrow ZnO \quad (29)$$

The Zn source is the anode slurry which is stored in the anode compartment of the cell. The cathode can of the Zn/Air cell has small holes in the bottom of its structure, which allows air ingress. The structural, electrochemical, and transport properties of the cell are discussed in more detail later in this thesis.

Zn/Air primary cells are used almost exclusively as a power source for hearing instruments, commonly referred to as hearing aids. The hearing instrument market is segmented into two main device categories: analog and digital. The devices are designed around extremely complex electronic circuitry, which leads to demanding discharge protocols. The typical current experienced by the Zn/Air cell during discharge in this application is around 1mA (for Size 13 cells). During instances of high-demand (i.e., noisy surroundings), the cell can experience pulsed currents upwards to 12mA.

In addition to hearing instruments, Zn/Air cells are also used in applications such as medical telemetry devices, pagers, portable battery chargers, military applications, and also as an alternative fuel source (automobiles, buses, etc.).[1] The main reasons limiting the broad use of these cells are the tradeoffs between long service life and maximum power capability.[1] Environmental implications associated with this cell are many and lead to these tradeoffs, which are discussed at length in the second chapter of this thesis.

There are two main modeling approaches that are developed in this thesis. The first uses Butler-Volmer reaction kinetics coupled with diffusional limitations at each electrode to predict polarization curves (Voltage vs. Current Density) of the Zn/Air cell and account for overpotential losses at given stages of discharge based on a pseudo steady-state. This is then incorporated in a time-dependent shrinking core reaction model

for the discharging zinc particles in order to develop an overall predictive discharge curve (Cell Voltage vs. Time). The strength of this approach lies in its conceptual simplicity and the analytic form of the final result that is easy to use for predictive and design purposes. The approach presented is an alternative to that developed by Mao and White, wherein only numerical results are possible.[40] The approach developed in this thesis allows for rapid analytical prediction of overall cell performance at constant discharge currents based upon simple and readily available parameters in an acceptable level of accuracy. In addition to polarization and performance plots, percent capacity versus time plots are presented. This analysis allows useful insights into the overall performance of the Zn/Air cell and the design and operating parameters that affect it.

SUMMARY OF THESIS

Chapter II is an overview of Zn/Air cell assembly components, overall cell operation, and a literature review. The individual components that comprise the Zn/Air electrochemical cell are discussed, including anode and cathode electrode materials, various physical design characteristics,

Chapter III introduces electrochemical notions required for development of predictive anode, cathode, and electrolyte models. After derivation of non-specific electrode overpotentials, the electrode specific overpotentials are derived. For description of the diffusive characteristics of the cathode plaque assembly, the Dusty Fluid Model is employed. The derived anode overpotential is then combined with the Shrinking Core Model to describe the time-dependent reaction of Zn. These concepts are then used in concert to develop an overall time-dependent, predictive model for Zn/Air cell performance.

Chapter IV discusses the relevant experimentation that was completed during the course of this work. The techniques and associated equipment utilized for cell discharge are discussed. In addition, other methods employed to gain insight into the physical aspects of cell discharge, including SEM and Light Microscopy techniques, are described. Of particular novelty is the utilization of mounting and polishing of "potted" discharged cells followed by an extraction technique introduced by Horn et al.[4] This technique allows for examination of cells without direct Zn reaction thus providing clear images and accurate conclusions based upon the images.

Chapter V discusses the results associated with the predictive model and its congruency to experimental results. Successes and shortcomings associated with the model at varying discharge rates are discussed.

Chapter VI provides overall conclusions of this work. In addition, it suggests numerous areas for further experimentation and mathematical development to provide increasingly more accurate model predictions for Zn/Air cell development.

CHAPTER II
CELL DESCRIPTION, OPERATION, AND LITERATURE REVIEW

BACKGROUND

Figure II-1 illustrates an assembled primary Zn/Air cell used for hearing instrument applications. There are design differences amongst various manufacturers, but the general construction is similar. Zinc is a commonly used anode material for most types of alkaline primary and secondary cells, and composes the anode for the Zn/Air cell. The zinc, along with a gellant and the electrolyte, is contained in the anode can. The gelled mass of these three constituents is commonly referred to as the anolyte or slurry. The mass transport and reaction kinetic characteristics of zinc discharge are important factors in understanding the performance capability of the cell. These topics are discussed further later on in this chapter.

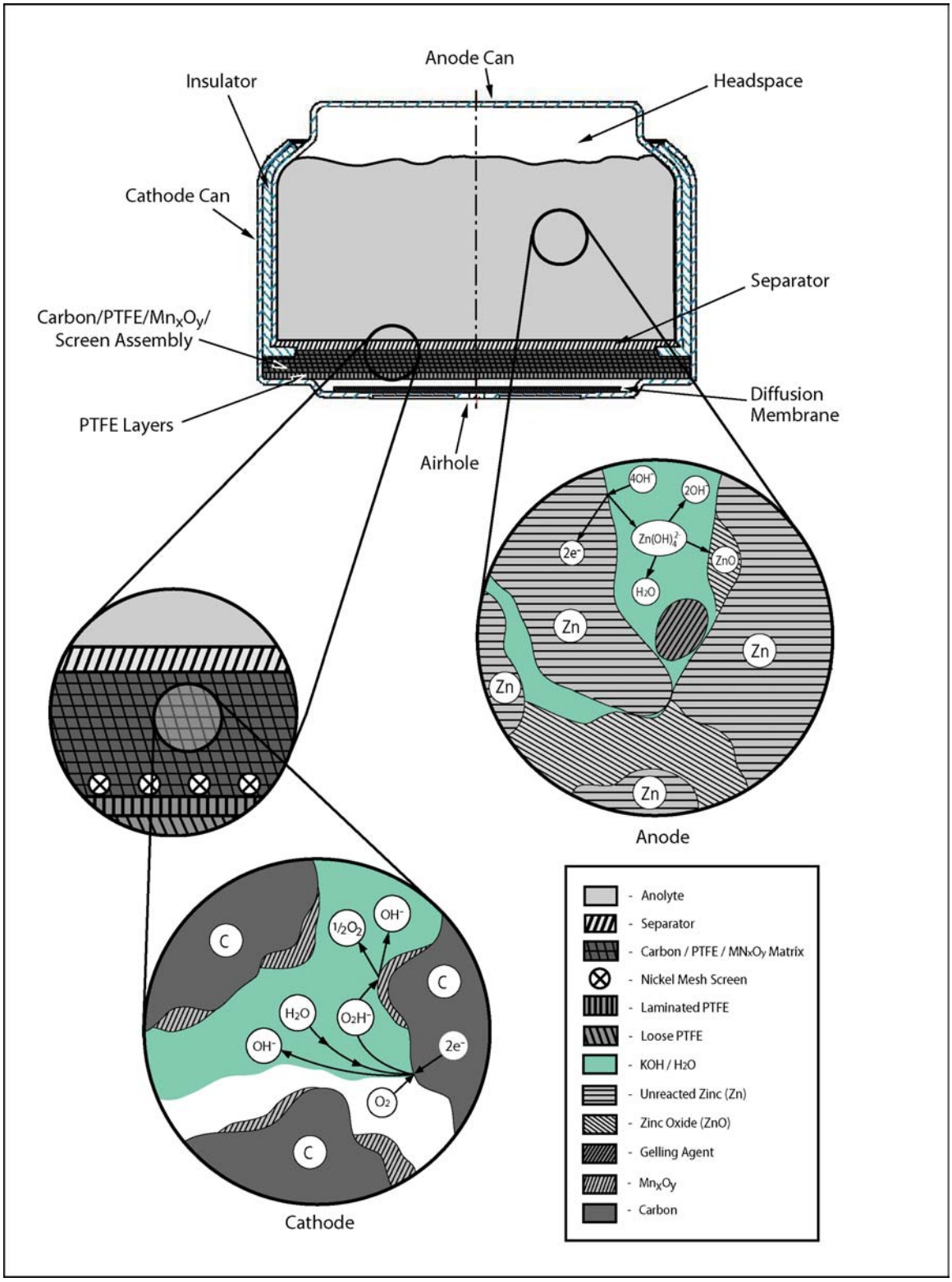

Figure II-1: Schematic of an assembled Zn/Air cell including the cathode and anode nanostructures.

Electrical shorting between the anode and the cathode cans is prevented by a molded plastic insulator (also referred to as a grommet), as shown in Figure II-1. The insulator is typically molded from Nylon® or similar polymer. In addition, electrical shorting between the anode and cathode internal compartments is prevented by the separator, which is a woven paper mesh. With the separator in place, the probability of a zinc particle coming in direct contact with the carbon-catalyst-screen matrix (discussed in more detail later) is significantly reduced. There are important design considerations in properly selecting the separator material. First, the separator thickness and density must be sufficient to prevent zinc particle penetration. Moreover, the separator thickness and density cannot be excessive as it must allow sufficient ionic transport (discussed in more detail later). The separator contributes to the overall impedance of the assembled cell, as it provides resistance to ionic transport. Improper design and selection can thus lead to the construction of a high-impedance cell that is not capable of supplying a sufficient running voltage or discharge characteristics to power a hearing instrument.

The cathode can assembly consists of the cathode can, an air diffusion membrane, one or two layers of a hydrophobic, porous, polymeric material, such as polytetrafluoroethylene (commonly referred to as PTFE and commercially available as Teflon® from Dupont or Excellerator from W.L. Gore), the catalyst-screen matrix (Carbon/PTFE/Mn_XO_Y mix on nickel screen), and the separator. In a two-layer PTFE structure, the first layer of PTFE is loosely placed in the cathode can, along with the air diffusion membrane, during cathode can sub-assembly. The air diffusion membrane is typically comprised of high-grade filter paper. The separator is typically non-woven cellulose material (commercially available from Celgard, LLC or Tonen Petrochemical

Co.) placed in the can to provide uniform air distribution throughout the overall geometric surface area of the cathode structure. The loose layer of PTFE provides the first barrier to water vapor transport (primarily ingress from the atmosphere). A second layer of PTFE is laminated onto the catalyst-screen matrix, along with the separator, during the manufacture of the cathode plaque structure (laminated PTFE/catalyst-screen matrix/separator) and is the final barrier to water transport (both to avoid ingress from the atmosphere and egress from the internal cell assembly). Water vapor transport has a significant deleterious impact on the performance of the cell and must be controlled. The control of water vapor transport both into and out of the cell is critical. Excess ingress of water vapor could cause the cathode plaque assembly to become flooded with water, thus preventing oxygen ingress and its subsequent reduction. In addition, the flow of water vapor out of the cell can lead to dry-out of the anode compartment. Both of these mechanisms have significant detrimental impact on the overall performance of the cell. These mechanisms will be discussed in more detail later on in this chapter.

The catalyst-screen matrix provides catalytic properties for the reduction of O_2, a diffusion structure, as well as a current collector. The main component of this assembly is carbon, typically of high-grade electrolytic quality such as the commercially available Vulcan XC-72 or high-conductivity carbon black from Cabot Corporation. The average particle size for the selected carbon varies, but is typically on the order of 30 nanometers for Vulcan carbon. Additional materials with catalytic properties, such as various manganese oxide species, are incorporated in the carbon matrix to further aid the electrochemical reduction of oxygen. The final component of carbon-catalyst blend is PTFE. This is added to help control water transport on some level, but primarily added

as a binding agent. This also aids in the prevention of electrolyte from filling up the cathode layer rapidly and completely, thus allowing oxygen access to reaction sights via the creation of open sphere boundaries. The typical PTFE loading is 30 to 40 weight percent. The carbon-catalyst blend is supported on a nickel mesh (or expanded metal) screen. The main purpose of the screen is to serve as a current collector and to provide a direct path for transport of electrons from the external circuit to the cathode structure. Nickel can act as a catalyst for oxygen reduction in certain instances. If the design of the cathode structure is such, a secondary purpose is to aid in the catalytic reduction of oxygen. The overall structure and its individual components' contribution to the electrochemical performance of the cell are discussed in more detail later on in this chapter.

The electrolyte utilized with the Zn/Air cell is alkaline aqueous potassium hydroxide (KOH). The typical molarity of the electrolyte is 6M or approximately 35 weight percent KOH in water. A low weight percentage of zinc oxide (ZnO) is added to the electrolyte to prevent self-discharge of the cell as well as hydrogen gas formation.

The anode consists of electrochemical grade, amalgamated zinc particles such as those available from Union Miniere or Noranda Advanced Materials. The average particle size varies, but is typically 250 micrometers. As mentioned, the zinc is amalgamated or alloyed with mercury to a level of 2 to 4 weight percent. Through natural occurrences, there are typically other metallic species in the zinc particles, such as lead, tin, and calcium (among others). Many of these species can lead to gassing in alkaline electrolyte solution, particularly iron and nickel, and need to be minimized, as discussed in more detail later in this chapter.[10]

A final additive in the zinc matrix is gelling agent(s). Typically the gelling agents are organic compounds, such as Aqua Keep from Absorbent Technologies or Water-Lock from Grain Processing Corp., that do not aid or detract from the electrochemical oxidation of zinc. The particle size of these additives are typically of 50 micrometers or less. The anode compositions typically include 1 weight percent or less of the gelling agent. The purpose of the gellant additive is to provide uniform electrolyte distribution in the anode compartment. This is discussed in more detail later in this chapter.

ANODE

The anode compartment of the Zn/Air cell consists of a portion of the molded plastic insulator, the anolyte, and the anode can. The anode can acts as one of the electronic current collectors for this system. As the zinc oxidation process occurs, electronic transport in the anode compartment is zinc particle to zinc particle. Upon reaching the internal anode can surface, the electron transfer then occurs through the highly conductive anode can. The various interactions in this compartment of the cell are rather complex. There are numerous reaction pathways that have been proposed for the oxidation and passivation of zinc in alkaline solutions. The associated kinetics of these reactions are also complex. This section discusses the elementary reactions that take place in the anode compartment as well as the kinetics and mass transport characteristics of the Zn/Air cell anode.

The overall Zn sequential oxidation and passivation reactions can be:[2]

$$Zn + 4OH^- \rightarrow Zn(OH)_4^{2-} + 2e^- \quad (1)$$

$$Zn(OH)_4^{2-} \rightarrow ZnO + 2OH^- + H_2O \quad (2)$$

The overall anode reaction for the complete zinc oxidation (or dissolution) and passivation process via the reactions above may thus be written as:

$$2Zn + 4OH^- \rightarrow 2ZnO + 2H_2O + 4e^- \quad (3)$$

In the first reaction step, the zinc oxidizes to form zincate ions $[Zn(OH)_4^{2-}]$, which transfer into the electrolyte solution. The two associated electrons conduct electronically to the external circuit (e.g., hearing instrument) through the zinc matrix and subsequently the anode can current collector. The second sequential reaction step is the precipitation of zinc oxide (ZnO), which releases two hydroxyl ions and water. This two-step reduction path has been extensively investigated and generally accepted as the overall discharge mechanism for Zn in concentrated alkaline solutions that are concentrated. This mechanism was first proposed by T.P. Dirkse via EMF investigations.[51] His interpretations were further supported via investigations utilizing Raman and NMR spectroscopy done by Fordyce and Baum and Newman and Blomgren respectively.[7,8]

During discharge, the concentration of $Zn(OH)_4^{2-}$ will eventually reach its solubility limit and will precipitate out of solution via Reaction (2).[9] This manner of precipitation occurs in the absence of convective flow and the precipitate is defined as Type I film. The lack of convective flow facilitates the super-saturation of electrolyte local to Zn particles and subsequently results in the precipitation of ZnO. Type I film is characterized by its white color, low apparent density, and flocculence.[10] It is essential that the precipitation reaction occur as quickly as possible, with minimal impact on non-discharged Zn access to hydroxyl ions. If this does not occur, Zn utilization (and subsequently capacity) will be significantly reduced due to a reduction of access of hydroxyl ions to Zn for reduction.[10] In the presence of convective flow, direct oxidation

to ZnO can occur and Type II films develop. This form of ZnO is much more dense and forms directly on the Zn particle surface.[9] Both types of film formation develop passivation layers on the surface of the Zn particles, which reduces the overall discharge performance of the cells in a few ways. The internal cell impedance is increased due to an increase of the Ohmic resistance across non-discharged Zn particles. There is a reduction of hydroxyl ion access to non-discharged Zn particles, which has a deleterious effect on capacity. Furthermore, the discharge reaction front in the cell is from the separator outward into the anode compartment. Depending upon the discharge rate, the formation of ZnO films, particularly Type I, near the separator surface leads to an obstruction of OH^- transport from the cathode compartment into the anode compartment. Again, this limits the cell's overall performance. The discharge front described is discussed in more detail in Chapter V – Results and Discussion.

The formation of solid potassium zincate [$K_2Zn(OH)_4$] also occurs.[9] This formation, coupled with the formation of ZnO, has a dramatic effect on the anode compartment characteristics. Both products are greater in molar volume than Zn, which causes both a reduction in the void fraction (porosity) among Zn particles in the anode chamber and a reduction in the anode compartment head space. The anode compartment head space is the volume in the anode compartment that is not occupied by the anode slurry. The amount of head space present prior to and post discharge is an important design characteristic. If there is inadequate head space then the probability of the assembled cell leaking is high due to the internal force exerted on cell walls from the conversion of Zn to ZnO, which has a higher partial molar volume than Zn, during cell discharge. In addition, after discharge, the cell dimensions will grow and removal of the

cell from the device after use may not be possible. The porosity reduction limits transport of ions to unreacted Zn particles. The reduction of anode compartment head space leads to increased internal pressure, which can subsequently lead to cell leakage. The formation of $K_2Zn(OH)_4$ effectively reduces the concentration of electrolyte and hence reduces electrolyte conductivity and overall cell performance by reducing the amount of OH^- ions available for Zn reduction.[1]

As previously mentioned, the Zn/Air electrolyte consists of a potassium hydroxide (KOH) and water solution. Typically the mixture is between 30 and 40% (by weight) KOH with a small percentage (~2% by weight) of ZnO added to it. The addition of ZnO helps to prevent spontaneous cell discharge via direct dissolution of Zn while at rest by equilibrium adjustment and production of hydrogen gas. The remaining percentage of the solution is water.

During the dissolution and passivation of zinc in alkaline electrolytes, it is possible for hydrogen gas to form via the electrolysis of water. When this occurs, after the completion of Reactions (1) and (2), it is possible for the formed water to hydrolyze via Reaction (4).[49]

$$2H_2O + 2e^- \rightarrow 2OH^- + H_2 \quad (4)$$

When Reactions (3) and (4) are combined, the resulting overall chemical reaction is:

$$Zn + H_2O \rightarrow ZnO + H_2 \quad (5)$$

The presence of ZnO helps to inhibit the formation of hydrogen gas via this process.[1] Hydrogen gas formation in the anode compartment of the Zn/Air cell is detrimental since can have a dramatic effect on cell performance reduction. The formation of hydrogen gas can lead to cell leakage and a reduction of the overall electrical performance of the

Zn/Air cell. The presence of ZnO does have a negative effect at higher concentrations in that there is an overall reduction of the specific conductance of the electrolyte solution.[9] This must be considered when designing a Zn/Air cell. Also, the presence of ZnO in electrolyte means that the zincate ion solubility limit will be reached more quickly.

ANODE REACTION KINETICS AND MECHANISMS

A universally accepted zinc passivation and dissolution mechanism currently does not exist. However, all proposed mechanisms do include two electron transfer as well as various intermediate Zn species such as ZnO, $Zn(OH)_4^{2-}$, and ZnOH. Some of the proposed dissolution mechanisms will be reviewed in brief below.

The reaction steps described in Reactions (1), (2) and (3) are simplified. A more involved reaction mechanism was proposed as follows[53]:

$$Zn + OH^- \rightarrow Zn(OH) + e^- \quad (6)$$

$$Zn(OH) + OH^- \rightarrow Zn(OH)_2^- \quad (7)$$

$$Zn(OH)_2^- + OH^- \rightarrow Zn(OH)_3^- + e^- \quad (8)$$

$$Zn(OH)_3^- + OH^- \rightarrow Zn(OH)_4^{2-} \quad (9)$$

$$Zn(OH)_4^{2-} \rightarrow ZnO + 2OH^- + H_2O \quad (3)$$

This mechanism incorporates a four step dissolution reaction mechanism that is then followed by the passivation reaction [Reaction (3)]. There are a total of two charge transfer reactions [Reactions (6) and (8)]. The rate determining step for this process is proposed to be Reaction (8).[53]

An additional mechanism proposed by Hampson et al. utilizes the formation of kink sites during the Zn dissolution with associated adsorption of intermediate Zn

species.[54] This mechanism has been used as the theoretical basis of varying Zn dissolution rates since it has been proposed that the dissolution rate is directly proportional to the varying densities of kink sizes. The mechanism proposed by Hampson et al. is as follows:[54]

$$Zn_{kink} + OH^- \rightarrow Zn(OH)_{ads}^- \quad (10)$$

$$Zn(OH)_{ads}^- \rightarrow Zn(OH)_{ads} + e^- \quad (11)$$

$$Zn(OH)_{ads} + OH^- \rightarrow Zn(OH)_2 + e^- \quad (12)$$

$$Zn(OH)_2 + 2OH^- \rightarrow Zn(OH)_4^{2-} \quad (13)$$

$$Zn(OH)_4^{2-} \rightarrow ZnO + 2OH^- + H_2O \quad (3)$$

This mechanism also incorporates a four step dissolution reaction mechanism that would then be followed by the passivation reaction [Reaction (3)]. Adsorption of Zn species occurs in Reactions (10) and (11). There are a total of two charge transfer reactions [Reactions (11) and (12)]. The rate determining step for this process is proposed to be Reaction (10).[54]

CATHODE

The cathode compartment of the Zn/Air primary cell consists of the cathode structure and a cathode can. The components of the cathode structure, as previously described, are the air diffusion membrane to distribute air, two layers of PTFE® as moisture barriers, the catalyst screen (Carbon/PTFE/MnO_2 mix on nickel screen), and the separator. It is through this that the oxygen must diffuse and electrocatalytically reduce with electrons to complete the electric circuit. The cathode structure is extremely thin and thus allows for a relatively high volume fraction of zinc in the anode compartment.

This design characteristic leads to a high energy density for such a small cell. The current designs of air cathodes stemmed from fuel cell research and the development of fluorocarbons, such as PTFE. Typically, the PTFE is blended in the carbon matrix where it functions as a binding agent (providing a bonded catalyst structure) and provides hydrophobic characteristics. A relatively low ambient humidity in comparison to the cell anode compartment will lead to the loss of water vapor from in the cell. This results in a reduction of electrolyte conductivity. In addition, this condition will lead to a drying out of the cathode. A relatively high ambient humidity in comparison to the cell anode compartment, on the other hand, will lead to transport of water inside the anode compartment. This will dilute the electrolyte and reduce the conductivity of the electrolyte. Temperature will affects the above processes.

In order for the cell to perform properly, a three-phase interface must develop in the cathode. That is, some electrolyte must diffuse into the cathode structure (through the separator) to establish an interface between the solid carbon/catalyst structure and the diffusing/electrocatalyzing oxygen gas. This interface is essential for effective performance as gaseous oxygen must have simultaneous access to catalyst sites, electrons, and electrolyte.

CATHODE OXYGEN REDUCTION REACTIONS

At the cathode, the following multi-step reactions occur[3]:

$$O_2 + H_2O + 2e^- \rightarrow O_2H^- + OH^- \quad (14)$$

$$O_2H^- \rightarrow OH^- + \tfrac{1}{2}O_2 \quad (15)$$

With an overall cathode reaction of:

$$O_2 + 2H_2O + 4e^- \rightarrow 4OH^- \quad (16)$$

The oxygen (along with other air constituents including CO(g), CO_2(g), N_2(g), and H_2O(g), which all can contribute to performance issues) enters the cell through the air access holes in the cathode can (see Figure II-1) once the protective seal is removed. The oxygen then passes through the air diffusion membrane, which allows for a more even air distribution across the cathode surface area. There after, the oxygen then passes through the PTFE® layers, which are hydrophobic, and limit the amount of ambient water vapor that is carried along with the oxygen to the carbon/catalyst layer. Upon contact with the carbon/catalyst layer, the oxygen catalytically reduces in the presence of the two electrons arriving via the external circuit from the anode reaction and produces hydroxyl and peroxide ions [Reaction (14)]. The formation of hydroxyl ions is aided by the carbon black support, which is a catalyst of oxygen reduction in alkaline solutions as well as a conductor of electrons. As previously mentioned, it is possible for the nickel screen to act as a catalyst for O_2. In order for this to be accomplished, the nickel screen must be positioned in a location that has readily available access to both oxygen ingress as well as liquid electrolyte. The hydroxyl ions formed diffusive into the anode compartment and directly combine with zinc ions as explained above. The peroxide ions are further reduced via Reaction (15) to form hydroxyl ions and soluble oxygen. This inherently slow reaction is catalytically aided by the Mn_XO_Y that is present in the carbon matrix.[3] Some of the soluble oxygen reacts further via Reaction (14) and adds to the concentration of hydroxyl ions. For the cathode, the current collector is a combination of the cathode can and the nickel screen. The cathode can is in electrical contact with the nickel mesh and allows current flow to the reaction sites.

The reaction at the cathode is much slower than that of the anode and thus is the rate determining step for the overall cell reaction. This is due to the slow kinetics of this reaction (low exchange current density).[3,9]

CATHODE REACTION KINETICS AND MECHANISMS

The oxygen reduction in a Zn/Air cell occurs at ambient conditions (pressure and temperature). Of particular importance to the overall description of the reaction kinetics and associated mechanism of the oxygen reduction is the temperature of the reaction. There have been significant studies done in regards to the reduction of oxygen over various cathode assemblies in various aqueous electrolyte solutions.[3] There is a high overpotential associated with cathodic reduction of oxygen in aqueous electrolytes, and thus a major focus of these studies has been the development of improved electrocatalysts.[3]

In aqueous electrolytes, two main paths of oxygen reduction are accepted: the direct 4-electron pathway and the 2-electron peroxide pathway. The direct 4-electron path in alkaline solutions consists of various steps that lead to the formation of hydroxyl ions.[3] The overall reaction for this pathway is written as follows:

$$O_2 + 2H_2O + 4e^- \rightarrow 4OH^- \qquad (17)$$

The peroxide path for alkaline solutions is represented by Reactions (14), (15), and (16). This pathway has been assumed as the basis for the cathode reaction for this thesis since it is universally agreed that this mechanism is dominant for most carbons, and most oxide covered metals.[3] As previously discussed, the cathode structure for the Zn/Air cell consists of carbon support and Mn_XO_Y catalysts. Yeager et al. have proposed that there are two possible reaction paths for the formation of peroxide that are possible:[10]

$$O_2 + H_2O + 2e^- \rightarrow HO_2^- \text{ (ads)} + OH^- \quad (18)$$

or

$$O_2 + H_2O + 2e^- \rightarrow HO_2^- + OH^- \quad (19)$$

The formed peroxide can then follow two additional possible paths: reduction or catalytic decomposition.

$$O_2H^- \text{ (ads)} \rightarrow OH^- + \tfrac{1}{2}O_2 \quad (20)$$

or

$$HO_2^- + H_2O + 2e^- \rightarrow 3OH^- \quad (21)$$

The decomposition of peroxide is given in Reaction (14) or alternatively as:

$$HO_2^- \text{ (ads)} + H_2O + 2e^- \rightarrow 3OH^- \quad (22)$$

The elementary reaction steps for the peroxide path over carbon black are described below. Reaction (24) is considered to be the rate determining step and will be utilized for the formation of a rate reaction in cathode modeling:[3,10]

$$O_2 + e^- \rightarrow O_2^- \quad (23)$$

$$O_2^- + H_2O \rightarrow HO_2^- + OH \quad (24)$$

$$OH + e^- \rightarrow OH^- \text{ (rapid)} \quad (25)$$

CATHODE PERFORMANCE EFFECTS

Gas-transfer rate greatly affects the limiting current capability of a Zn/Air cell. The relative humidity of the surrounding air generally degrades the gas-transfer rate. The limiting current, i_L, is stated as the maximum continuous-current possible as limited by gas diffusion.[12] In the instance of the Zn/Air cell, one major physiochemical contributor

to the overall limiting current of the cell is the diffusion of O_2 due to the slow reaction kinetics associated with oxygen reduction and transport. This is affected by the ability of oxygen to diffuse through the structure of the air distribution membrane and PTFE layers.

There is also a limiting factor associated with the formation of peroxide ions, however. As the concentration of peroxide ions is increased at the carbon interface, the ability of oxygen to come in contact with the carbon catalyst is reduced. This also limits the performance of the cell. The effect of limiting current, service life, and gas-transfer is qualitatively illustrated in Figure II-2. It is evident from this figure that the higher the gas-transfer rate, the lower the service life of the cell. This is so since, when under discharge conditions or at rest, the transfer of oxygen and its subsequent catalysis is increased with higher gas transfer rates. This limits the overall service life of the cell since there is a greater amount of reacting Zn (whether in use or not). Under high discharge conditions, this characteristic is typically beneficial since there would inherently be maximum hydroxyl ion exposure to unreacted zinc. Under more standard discharge conditions, this characteristic is detrimental since a greater proportion of direct Zn oxidation will occur when the device in not in use. The overall limiting current for the assembled cell can be reduced with greater air access. For the overall assembled cell, the oxygen reduction reaction is typically limiting. Increasing air access will increase the reaction rate for this limiting step, thus reducing the limiting current for the assembled cell. Examination of Figure II-2 shows these concepts. However, it is more likely that the limiting current is more linear in gas transfer rate, as shown via Equation (26).

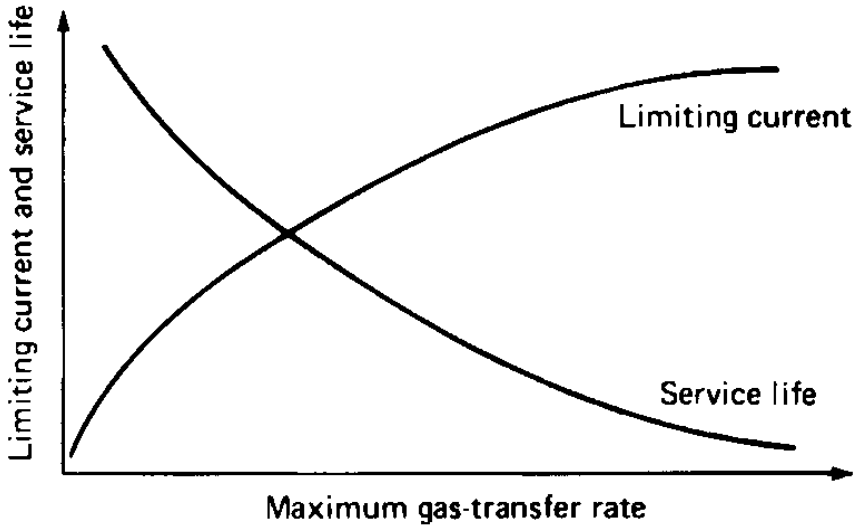

Figure II-2: Effect of gas-transfer rate on limiting current and service life.[1]

An additional physiochemical property that has a major impact on the limiting current is the solubility of oxygen in the electrolyte mixture. Fick's first law mathematically states that relationship between limiting current density and solubility (as well as diffusivity which is mentioned above).[1]

$$i_L = \frac{nF}{\delta_L} DC_b \tag{26}$$

Where n is the number of electrons involved in the electrochemical process, F is Faraday's Constant, δ_L is the diffusion layer thickness, D is the diffusion coefficient, and C_b is the concentration of soluble O_2 in the bulk electrolyte. By examination of Equation (26), one can readily see the direct proportionality of solubility of O_2 concentration in the bulk electrolyte as well as the maximum diffusion rate (DC_b/δ) on i_L. The molar concentration of the potassium hydroxide solution utilized in the construction of Zn/Air cells is typically 6M. At this concentration and STP conditions, the typical bulk solubility of O_2 is approximately 1×10^{-4}mol/L and the diffusion coefficient is ~6.4×10^{-6}cm^2/s.[3,11] Assuming a diffusion layer thickness of 0.01016 cm, the calculated limiting current density for the Zn/Air cathode is 6.56×10^{-8} mA/cm^2. This number will be re-visited later in this thesis during the solution of the developed mathematical model.

Additional performance issues arise from the transfer of CO(g), CO_2(g), N_2(g), and H_2O(g) along with O_2 from the air. The effect of N_2(g) is simply to reduce the concentration of O_2(g) available for reduction in the cathode electrode. The presence of H_2O(g) can have significant effect since it can reduce the electrolyte conductivity through dilution and can lead, under more severe conditions, to flooding of the cathode plaque assembly. The effects of CO(g) and particularly CO_2(g) are also deleterious. As

previously discussed, the electrolyte used in the Zn/Air cell is KOH(aq). When KOH(aq) comes in contact with CO_2(g), the formation of solid potassium carbonate, K_2CO_3, occurs via

$$2KOH + CO_2 \rightarrow K_2CO_3 + H_2O \quad (27)$$

The production of K_2CO_3(s) has several effects. Its most obvious effect is a reduction of electrolyte conductivity by reducing the overall amount of free hydroxyl ions. Since it is a solid particle, it can also inhibit the ionic transport of hydroxyl ions in the anode compartment by reducing the void volume amongst particles and effectively reduce cell performance. If the formation of the solid particles occurs in the cathode, then layer separation (or delamination) and/or an increase in diffusive resistance can occur and lead to an increase in cell impedance.

OVERALL CELL REACTION

The initial overall cell reaction during the formation of dissolved zincate ions is:

$$Zn + 2OH^- + \tfrac{1}{2}O_2 + H_2O \rightarrow Zn(OH)_4^{2-} \quad (28)$$

and finally with the precipitation of ZnO, it is:

$$Zn + \tfrac{1}{2}O_2 \rightarrow ZnO \quad (29)$$

The combined standard anode [1.26V for Reaction (3)] and cathode [0.40V for Reaction (16)] potentials equate to a theoretical cell voltage of 1.66V for Reaction (29).[52] The typical maximum open circuit voltage (OCV) for such a system in practice is approximately 1.45V, as a result of the very high activation overpotential of the cathode. The limiting current of such a cell depends upon the cell size (mass/volume of zinc), the discharge settings, and, as Figure II-2 shows, the gas transfer rate. Overall limiting currents for assembled Zn/Air button cells can vary from 6-100mA at 1.1V.

LITERATURE REVIEW

This thesis provides an analytical model for performance analysis of the Zn/Air primary cells used for powering hearing instruments and compares the predictions to experimentally determined data. The relevant literature studies of mechanistic, structural, and modeling studies are summarized below.

Anode Studies

Numerous works have been completed examining the dissolution of zinc in alkaline electrolytes, as summarized below.

Early work on the discharge of the Zn electrode with alkaline electrolytes was completed by Dirske.[51] The dissolution of Zn was examined under various concentrations of aqueous potassium hydroxide and the subsequent effect of amalgamation and zincate ion concentration on the overall process. Various reaction mechanisms were proposed. Of most importance was the establishment of the dissolution-precipitation mechanism that became the basis of studies discussed later in this literature review. Thus, Dirske's study made a significant impact in the understanding of the Zn dissolution-precipitation mechanism.

Powers and Breiter completed examinations of anodic films and cobwebs formed during the dissolution of Zn in strongly alkaline soutions.[9] Their examinations led to the postulate that two types of ZnO species form during dissolution. Type I ZnO was described as white, loose, and flocculent. It was concluded that this film forms in the absence of convective flow and after supersaturation of zincate in the area near the Zn electrode. Type II ZnO was described as more dense and ranging in color from light gray

to black. The color of Type I ZnO was determined to be dependent upon the potential and depth of discharge. Type I film formed directly on the electrode surface in the absence of convective flow and was thought to be the variation of ZnO primarily associated with Zn passivation. Powers then expanded on this work by further examining the physical characteristics of the Zn electrode under discharge, with particular attention given to Type II films.[17] The formation of cobwebs in the ZnO film was noted during dissolution of Type II ZnO. It was also stated that the appearance of these cobwebs had a correlation with hydrogen gas evolution and they accelerated the formation of spongy Zn or dendritic Zn, depending upon the cathodic potential. Powers completed further examination into the hydrogen evolution behavior of Zn electrodes in alkaline solutions.[10] This work provided further evidence that Type II ZnO catalyzed the formation of hydrogen bubbles. It was found in these experiments that the addition of various metals were accelerating effects on hydrogen gas formation. Metals that had this ability in alkaline solutions are iron, nickel, and platinum. Other metals had retarding effects on the formation of hydrogen gas, such as mercury, lead, and tin. These are important findings since the selection of component base materials (i.e., anode can) are determined to insure that the inclusion of hydrogen gas catalysts are eliminated or at the very least kept to a minimum.

Cachet et al. examined the kinetics of the Zn electrode in alkaline electrolytes.[55] Impedance and polarization measurements were completed on the discharging Zn electrodes. The results were indicative of not only a series of step-wise reactions, but also parallel reactions for the formation and reduction of adsorbed species. In addition, slow activation of the Zn electrode was noted with increasing overpotential. A lower

charge-transfer resistance was reported to accompany the dissolution reaction in comparison to the precipitation reaction, which is indicative of changing kinetics in the electrode. They concluded that the currently accepted mechanisms for Zn dissolution were insufficient since they did not include the parallel paths or the slow activation.

Cachet et al. also examined the behavior of the Zn electrode in alkaline solutions.[16] Electrochemical impedance studies were performed on discharging Zn electrodes. The reaction basis for the developed model consisted of a multi-step reaction process that involved to distinct charge-transfer reactions. The conclusions made from their work indicated that the dissolution of Zn occurred at reaction sites located in the pore structure of the electrode. In addition, the passivation films that formed reduced the anodic current with an increasing passivation layer and anodic polarization. They postulated that the addition of organic additives in the anode structure would reduce the dissolution of Zn due to the blocking of reaction pores and producing an alternative formation of the porous layer geometry. The mechanisms presented within this work serve as a basis for the modeling of the reaction kinetics of the anode for this thesis.

Meeus et al. completed studies on the reduction of mercury content in Zn powders for applications to electrochemical cells and batteries.[19] The level of mercury was reduced to levels of 1 to 3 weight percent with the inclusion of alloying elements, such as lead, indium, and gallium. In addition, an alternative amalgamation technique was proposed that incorporated mass amalgamation with surface amalgamation.

Huot completed a thorough review of the history of Zn batteries.[13] In this work, commentary on the various alloys of Zn electrodes was made. He noted that the elimination of mercury from Zn electrodes (this has not yet been done in the Zn/Air

electrode formulation), lead to a significant exposure to hydrogen gas formation, load capability, and shock sensitivity. The two main approaches for solution of these issues was the alloying of Zn or the incorporation of additives in the alkaline electrolyte. The incorporation of indium and lead as alloying elements was the first step that played a significant role in the reduction of hydrogen gas formation. Since then, the addition of calcium, aluminum, bismuth, and gallium, either individually or in various combinations, have proven to be beneficial as well. The addition of these alloying components needs to be done carefully so as to not reduce the performance capability of the alloyed electrode.

Huot and Boubour examined the performance of gelled Zn alloy powders in alkaline solutions under various discharge rates and temperatures.[14] Non-alloyed Zn powder did not perform well under all conditions examined. The powder passivated rather quickly and thus delivered a reduced service life. The inclusion of lead, bismuth, calcium, and aluminum as alloying elements to pure Zn powder increased the material utilization and thus service life. Benefits associated with indium alloys were only observable under high discharge rates.

Sato et al. examined the hydrogen gas evolution behavior of Zn alloys in alkaline electrolytes.[49] Amalgamated and non-amalgamated Zn powders were discharged and their gassing rates monitored. The amalgamated samples produced little to no hydrogen gas. When the mercury was removed, gassing increased. The formation of hydrogen gas evolution was suppressed with the addition of In_2O_3 to the electrolyte solution. It was postulated the deposition of indium on the surface of the Zn due to its overpotential in relation to hydrogen gas formation.

Fordyce and Baum studied complex Zn ions in aqueous alkaline solutions utilizing vibrational Raman spectroscopy techniques.[7] Various examinations were made on potassium hydroxide solutions that contained the zincate ion. Evaluation of the Raman spectra were indicative of a tetrahedral form. Newman and Blomgren studied complex Zn ions in aqueous alkaline solutions utilizing proton magnetic resonance spectroscopy.[8] ZnO was added to aqueous potassium hydroxide solutions. The formation of various Zn species was expected, with the dominant ionic species being zincate. Examination of the formulations via NMR spectroscopy were indicative of primarily the zincate ion with the possible inclusion of Zn to O bond of ZnO. These studies provided fundamental evidence in support of the Zn dissolution mechanism to zincate ions in alkaline electrolytes.

Yoshizawa and Miura investigated both Zn alloys as well as gelled anode additives.[20] The addition of indium, lead, bismuth, and calcium as alloying components to Zn powder was evaluated to increase hydrogen overvoltage. The inclusion of aluminum, calcium, and barium was also investigated and determined to smooth the Zn surface. The greatest reduction of hydrogen gas evolution on mercury free electrodes was obtained with alloys containing lead, indium, and bismuth. Various inorganic and organic additives were investigated. The lowest gassing levels were obtained with the addition of both indium hydroxide and perfluoroalkylpolyethylene oxide to the Zn alloy. Yang et al. examined the addition of surfactant additives to potassium hydroxide electrolyte and the resulting effect on discharge capacity of Zn electrodes.[15] The addition of sodium dodecyl benzene sulfonate to the electrolyte was determined to extend the discharge capacity due to the reduction of Zn surface passivation. This was further aided

by the formation of a loose and porous passive film on the Zn electrode surface, which allowed greater diffusion of hydroxyl ions to the Zn surface.

Glaser completed alloying and hydrogen gas evolution studies that led to the development of Zn alloys containing less than 0.5% mercury.[18] Various alloys containing indium, bismuth, and lead were discussed. It was presented that the best process for reduction was producing a Zn alloy of lead via an atomization process followed by the surface amalgamation of the Zn-Pb alloy.

Recently, an experimental technique was proposed by Horn and Shao-Horn that further enables the physical examination and understanding of discharged Zn.[4] Observations were then made in regards to the type of ZnO film formed and the resulting effects on cell performance. By the completion of a novel extraction and polishing technique, the self-discharge of Zn to ZnO via the presence of soluble oxygen species in water is avoided. In addition, the direct reaction of KOH with carbon dioxide is minimized. The elimination of these two reactions allows for the unobstructed visual observations into the discharge of Zn in alkaline solutions. A slightly modified version of this technique is utilized in this thesis to examine the discharge characteristics of the anode compartment of a Zn/Air cell.

Farmer and Webb examined mass transfer effects on Zn passivation in flowing alkaline electrolytes.[50] They found a relationship between electrolyte flow rate and the formation of passive films for various current densities. From their experimental work, a mathematical model for Zn dissolution was developed accounting for the diffusion of soluble species through the porous layer that forms on the Zn electrode and diffusion

through the electrolyte layer as a function of time. The model resulted in adequate analytical solutions of the mass transport process at long states of discharge.

Liu et al. studied the transient current density distributions of porous Zn electrodes in alkaline solutions.[56] Experiments were completed on electrodes with fixed pore patterns. The measured current distributions were non-uniform over varying discharge current densities and the non-uniformity increased over time. A mathematical model was developed to aid in the understanding of the physical experimental results. The basis of the non-uniformity based upon the developed model indicated that the resistance to charge-transfer and hydroxyl ion diffusion were the sources. Further adaptation of the model to include the physical observations of surface blockage of the anode was not successful in producing predictions that correlated with experimental results.

Isaacson et al. proposed a two-dimensional mathematical model current density and ZnO distribution in porous Zn electrodes.[57] The model predicted the overall movement of Zn and ZnO from the center of the electrode toward the surface of the electrode in 30 weight percent KOH. Non-uniform current density distribution and concentrations also enable material redistribution.

Sunu and Bennion developed a model for prediction of transient effects of the Zn electrode in alkaline solutions.[2] The model predicted the relation between time and perpendicular distance from the electrode and current distribution, solution potential, hydroxide ion and zincate ion concentration, porosity, Zn volume fraction, and ZnO volume fraction. Experimentation indicated that incorporation of a membrane in the electrode assembly reduced the Zn utilization. It was concluded that this was observed

due to the reduction of hydroxide ions available in the Zn compartment. The model predicted that the distribution of the reaction would be non-uniform and that the formation of reaction products would be thin. Under instances that included a membrane separator, the reaction products would form along the separator surface and lead to choke-off.

Cathode Studies

Numerous studies have been completed examining the reduction reaction of oxygen on various catalysts in alkaline electrolytes as reviewed by Kinoshita.[3] This section reviews the works that were utilized as a fundamental basis for the alkaline reduction of oxygen in this thesis.

Appleby and Marie investigated the kinetic properties of carbon materials for the reduction of oxygen in alkaline solutions.[41] Various forms of carbon were investigated, including carbon blacks, active carbons, and graphite, utilizing a ultra thin electrode with steady-state galvanostatic measurements for determination of activity. Various insights into possible reaction mechanisms and rate determining steps were developed as a result of their investigations.

Yeager et al. examined the electrochemical properties of graphite and carbon pertaining to the reduction of oxygen.[42] In this work, the direct 4-electron and peroxide pathways of oxygen reduction were introduced. Various electrochemical properties of carbon and graphite were reviewed, as well as the mechanistic reduction of oxygen on these catalysts. Yeager presented a thorough examination of the electrocatalysis of oxygen in relation to catalyst structure.[47] This work discussed the various mechanisms proposed for the reduction of oxygen in aqueous electrolytes. The proposed reduction of oxygen via

both the direct 4-electron transfer and peroxide pathways were reviewed. In addition, the reduction of oxygen over porous carbon electrodes was discussed. In this discussion, the importance of the inclusion of peroxide reduction catalysts was noted. Various proposed mechanisms were also reviewed. The direct 4-electron oxygen reduction mechanism reviewed in both of these works was utilized in the cathode modeling of this thesis.

Assad and Noponen investigated the performance of porous air electrodes.[58] To aid in the analysis, a mathematical model was developed to calculate electrode performance as a function of Tafel slope, exchange current density, and the effective diffusion coefficient for the electrode. Experimental variation of these properties was applied to the developed model. It was determined that the effective diffusion coefficient was dependent upon the geometrical properties of the cathode structure. The resulting recommendation was that porous air electrode design should incorporate a reduced path for oxygen diffusion. Increasing the wettability of the electrode will allow the transfer of electrolyte into the porous structure and thus increase the diffusion characteristics. Pisani et al. introduced a pore scale modeling approach applied to proton exchange membrane fuel cells (PEMFCs) incorporating various parameters associated with catalyst layer pore structure and their effects on PEMFC performance.[38] Their work indicated that the changes in oxygen and hydrogen concentration at the pore structure of the electrolyte changed significantly. This observation lead to the conclusion that modeling work assuming homogenous diffusion would have higher levels of inaccuracy. To account for the non-homogeneity, an averaging procedure was utilized to determine an effective expression that was not highly dependent upon concentration. The results were coupled with Butler-Volmer expressions to determine FC performance. The results of

the model indicated that the effects of the porous structure were significant in the overall performance of the FC. Although not directly pertinent, this work was utilized as a reference in regards to pore structure and its effects, which are incorporated in the model proposed in this thesis.

Meyers et al. investigated the impedance response of a porous electrode composed of intercalation particles.[48] The model assumed a porous electrode with no diffusional limitations in the solution phase. The model first examined the impedance response of an intercalation particle resulting in the determination of fundamental properties, such as charge-transfer, double-layer capacitance, and solid-phase diffusion. This basis was then expanded to describe a complete electrode. This type of analysis could have benefit for a study of the porous electrode utilized in the construction of Zn/Air cells.

Che et al. examined the catalytic properties and application of carbon nanotubes that were filled with metal-nanoclusters.[21] Their study focused on nanotubes that were fabricated via chemical vapor deposition. Catalysts for the reduction of oxygen were incorporated in the pore structure. This enables more accurate evaluation of catalytic properties of each tube due to the internal inclusion of the catalyst in comparison with an inconsistent surface coating. In addition, each tube can be evaluated as an individual reactor. Application of the tubes in a direct methanol fuel cell indicated a significant increase in cathodic current density (~20 times greater) due to the high surface area of the tubes and the high electrocatalytic activity. Although not specifically discussed, the incorporation of Mn_XO_Y into the carbon nanotube and application to Zn/Air cells could prove beneficial to increased cell performance and running voltage.

Cell Modeling

Numerous models have been published associated with the discharge performance prediction of cylindrical alkaline cells. However, very few models associated with the discharge performance prediction of Zn/Air cells exist. The various cylindrical alkaline cell models were reviewed due to the similarities associated with anode discharge and transient behaviors (i.e., separator plugging) to aid in the development of the model in this thesis. The primary models used as a reference basis in the arena of cylindrical alkaline cells are discussed. Following this review, existing models with more direct application to Zn/Air cells are then discussed.

Mak et al. investigated the performance prediction of cylindrical alkaline cells (Zn/MnO_2), where unlike Zn/Air cells the cathode is included in the cell assembly and consumed during use based upon quasi-equilibrium analysis.[22] This work indicated that linearity between discharge rate and load resistance and cathode mass at low discharge rates. At higher discharge rates, it was concluded that non-equilibrium states had impact on prediction and needed to be accounted for in the modeling to develop an accurate prediction. Expansion of their work led to a model that included polarization effects associated with ohmic resistances that develop during discharge as well as reaction kinetic limitations.[23] The model incorporated cathode design characteristics (cathode thickness) as well as curvature effects. Initial polarization effects of the porous electrode were examined neglecting mass transfer effects.

Chen and Cheh presented more complex models for cylindrical alkaline cells. A mixed-reaction model was developed that accounted for the formation of both ZnO and $Zn(OH)_4^{2-}$.[24] For more accurate prediction, Butler-Volmer equation was utilized to

account for electrode polarization and incorporated mass transport. The resulting model indicated that minor changes in KOH concentration (6M to 8M) had little impact on polarization. The main indicator for performance variation via the model was particle size of the MnO_2 (the smaller the better). This work was continued utilizing the dissolution-precipitation reaction, which also is presented in this thesis, and mass transport.[25] Their model indicated that the main contributor to cell polarization was the cathode reduction reaction due to mass transport limitations that are particularly evident at high-discharge rates. It was also indicated that the speed of hydroxyl ion transport across the separator from the cathode to the anode was key in providing long service life. This same characteristic will hold true in the Zn/Air cell. Since the reaction rate was determined to be highest at the separator interface, the precipitation of ZnO was highly concentrated at the separator. This is an additional characteristic that is seen in the Zn/Air cell at high discharge rates.

Podlaha and Cheh examined the discharge of cylindrical alkaline cells at high discharge rates.[26] Their initial work was a one-dimensional model that examined constant-current discharge. Three models were evaluated, with the most predictive being a model that accounted for separator pore plugging due to ZnO precipitation. This mathematical observation occurs in the Zn/Air cell and is supported by physical evidence (all discussed in Chapter 5). This work also included a sensitivity analysis of various cell design parameters on performance. The initial work was expanded to account for constant load, constant power, and pulsed current discharge conditions.[27] It was predicted that constant power loads contribute to the formation of a high cathodic overpotential associated with the reaction front movement in the cathode and thus result

in the lowest service life. The highest service life prediction occurred for constant load discharge due to the reduction of reaction rate over time and a reaction front more isolated to the electrode-separator interface. This model was then applied to a wound cell design.[28] The results indicated that a wound cell design would promote electrode utilization due to maximization of electrode access and electrode-separator interface.

The previous work was used as a basis for the differential algebraic solution of the governing equations presented by Zhang and Cheh.[29] This approach facilitated a more accurate prediction of cell performance since the solution of various cell parameters would be simultaneous and not explicit. Using the developed model, they then presented a rigorous sensitivity analysis for cylindrical alkaline cell performance prediction.[30] Their work indicated that the factors most affecting cell performance were effective cell length, discharge current, particle size, mass of active materials, and geometrical parameters. Effective cell length and discharge current were determined to be the most significant.

Kriegsmann and Cheh examined the effects of cathode porosity/composition utilizing the models presented by Podlaha and Cheh.[31] Their goal was to determine the optimized cathode porosity for maximum predicted cell performance for one discharge rate. It was determined that the most significant factor on extension of service life was the removal of graphite from the electrode matrix. Complete removal of the graphite gave the best predictions. Extension of the previous analysis was completed to account for the active material loading for both electrodes.[32] A specific active material loading for the cathode was determined with an associated anode active material loading number. The active material loading predictions were slightly less than those associated with

complete graphite removal. However, examination of Ragone plots (Specific Energy vs. Specific Power) indicated that the active material reduction was a better overall design. They continued further analysis of cathode electrode design parameters by examining the specific interfacial area.[34] The effects of adjusting the specific interfacial area in the cathode on predicted cell performance were evaluated. Simplification of the cathode model was completed via the assumption that the electrode structure exhibited no spatial fluctuations throughout the course of discharge. Comparison of these predictions with previous, more rigorous work gave similar results.

Krieggsman and Cheh also presented modeling work focused on the effects of zincate concentration during the discharge of cylindrical alkaline cells during anode oxidation reaction based upon the dissolution-passivation mechanism.[33] There work concluded that reduction of the zincate equilibrium concentration would lead to performance improvements. The was primarily attributed to the precipitation rate of ZnO. This model was then revised to account for a binary electrolyte and solely the direct formation of ZnO.[35] This approach simplified the model by neglecting the effects of zincate formation and allowing for more consistent physical property data. The overall service life predications were higher than those in their previous work, which was based upon a ternary electrolyte model. A complete evaluation of cell characteristics (porosity variation, Zn utilization, volume fraction, etc.) was completed utilizing this approach.

Zhang and Cheh presented work on random and uncertainty analysis applied to cylindrical alkaline cells.[36] This work accounted for randomness in various cell characteristics, such as particle size, and statistical uncertainties, such as transport coefficients. The effects of randomness and statistical variability of various parameters

on cell performance was evaluated using the differential algebraic model developed by Zhang and Cheh. Under one constant discharge regime, the technique was utilized to determine statistical variation in predicted cell performance.

Zhang and Cheh have also presented a two-dimensional model for performance prediction of the cylindrical alkaline cell.[37] This model, based upon macrohomgeneous theory, was developed to understand the effect of current collector length as a function of overall cell performance. The tertiary current density distribution was calculated incorporating kinetic, mass transport, and ohmic polarization. The optimum design, with cost implications, for the anode current collector was determined for two distinct continuous current discharge settings, with extension of the model to other modes of discharge possible, but not evaluated.

Thampan et al. approached the modeling of a PEMFC as a membrane reactor.[39] The model approaches the transport and/or reaction in each layer, describing transport via the Dusty Fluid Model and reaction kinetics via the Butler-Volmer expression. The analytic approach presented adequately described the performance of a PEMFC based upon various design parameters, such as PEM structure, relative humidity, pore size, porosity, thickness, among others. Deviation in predictions occurred under high current drains. This work was the basis for the modeling approach incorporated in the cathode structure of the Zn/Air cell in this thesis due to their many similarities.

A few mathematical models for overall cell performance prediction are found for primary Zn/Air cells in the literature. In addition, investigations of the Zn/Air cell individual components are available. Also available are related studies on the anode of alkaline primary cells or the cathode of hydrogen/oxygen alkaline fuel cells. A few

papers have been published focusing on the mass transport phenomena associated with zinc in alkaline solutions.

Mao and White published the most complete model for Zn/Air primary performance prediction.[40] Their numerical work expands on that of Sunu and Bennion with the inclusion of the separator, the air electrode, and the chemistry for the precipitation of potassium zincate and zinc oxide. It is a detailed model for predicting the discharge performance of a Zn/Air cell based upon various design parameters. The resulting model simulations had good agreement with experimental data. It was concluded that the primary reduction of zinc utilization was the depletion of hydroxide ions. In addition, the material loading in the anode was inversely proportional to material utilization and subsequently delivered capacity. Higher separator thickness led to increased material utilization, but subsequently reduced the running voltage due to increased resistance.

CHAPTER III
MATHEMATICAL MODEL

In the following sections, the mathematical development of the one-dimensional, time dependent predictive, analytical model is discussed. Basic notions associated with the Dusty Fluid Model are discussed and then applied to the cathode of a Zn/Air cell, which has many parallels with the approach employed by Thampan et al. for a Polymer Electrolyte Membrane (PEM) fuel cell.[39] Notions of electrocatalysis and kinetics are then introduced and applied to both the cathode and anode via the development of polarization equations based upon Butler-Volmer reaction kinetics for each electrode. The development of a time-dependent, unreacted zinc core radius based on the shrinking core reaction model is done next.[45] Subsequently, these time-dependent equations are combined with the polarization expressions to determine the time-dependent cell voltage.

EQUIVALENT CIRCUIT FOR ZN/AIR CELL

Equivalent circuits are employed extensively in the discussion of electrochemical power sources. Utilization of equivalent circuits allows the description of diffusion, kinetic, and general transport limitations in an electrochemical cell to that of an equivalent electrical circuit with corresponding resistances. This technique facilitates an easier physical "view" of the various operations taking place and insures inclusion of all processes occurring in the cell in the developed model. An equivalent circuit for a Zn/Air cell dealing with these internal resistances can be drawn as follows:

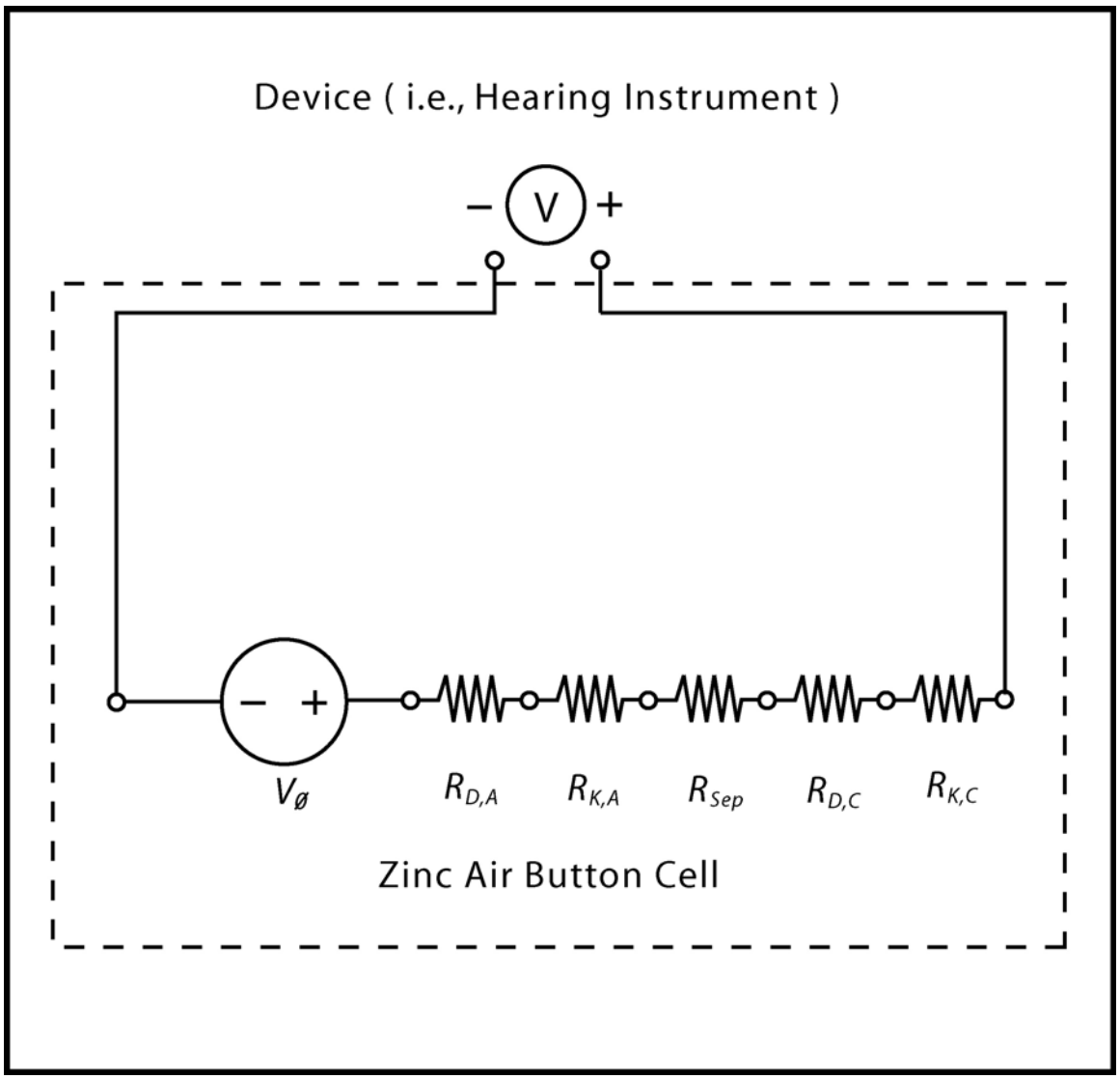

Figure III-1: Equivalent resistance circuit for a Zn/Air cell.

Key for Figure III-1:

V_0 represents the theoretical cell voltage.

$R_{D,A}$ represents the internal resistance associated with anodic diffusion.

$R_{K,A}$ represents the internal resistance associated with anode kinetics.

R_{Sep} represents the internal resistance associated with separator transport.

$R_{D,C}$ represents the internal resistance associated with cathodic diffusion.

$R_{K,C}$ represents the internal resistance associated with cathode kinetics.

TRANSPORT IN POROUS MEDIA: THE DUSTY FLUID MODEL

The transport of gases in the cathode plaque assembly will be modeled using the Dusty Fluid Model (DFM).[43] The DFM accounts for the species-to-species frictional interaction as well as the species-to-media interactions during transport. This allows for the determination of an overall transport coefficient to describe the species transport. For analysis of species transport via this model, the mass balance for species *i* under pseudo steady-state is:

$$\nabla \cdot N_i = \sum_{\rho=1}^{q} \nu_{\rho i} r_p \qquad ; \qquad i = 1,2,\ldots n \tag{30}$$

The current density in a respective region can be determined once the individual species fluxes are determined via the following relation:

$$i = F \sum_{i=1}^{n} z_i N_i \tag{31}$$

The DFM presented by Thampan et al. is employed in this work as:[43]

$$-\frac{c_i}{RT}\nabla_T \mu_i^e = \sum_{\substack{j=1 \\ j\neq i}}^{n} \frac{1}{cD_{ij}^e}\left(c_j N_i - c_i N_j\right) + \frac{N_i}{D_{iM}^e} + \frac{c_i B_0}{\mu D_{iM}^e}\left[\nabla p + \left(\sum_{j=1}^{n} c_j z_j\right) F \cdot \nabla \phi\right]$$

$$(i = 1,2,\ldots n) \tag{32}$$

The electrochemical potential gradient is:

$$\nabla_T \mu_i^e = \nabla_T \mu_i + z_i F \nabla \phi \tag{33}$$

Ordinary diffusion is accounted for via the D_{ij}^e diffusion coefficient. Interactions (i.e., frictional forces) between species *i* and the plaque structure is accounted for via D_{iM}^e diffusion coefficient. The last two terms on the right hand side of Equation (32)

account for convective fluxes and represent a pressure gradient (∇p) and potential gradient contributions ($\left(\sum_{j=1}^{n} c_j z_j\right) F \cdot \nabla \phi$), namely electroosmotic flow.

The permeability and effective diffusion coefficients for layer α via the DFM are:

$$D_{ij}^{e} = K_{i\alpha} D_{ij} = \left(\varepsilon_{\alpha} - \varepsilon_{\alpha 0}\right)^{q} D_{ij} \tag{34}$$

$$D_{iM}^{e} = K_{0\alpha} D_{iM} \tag{35}$$

$$B_{0\alpha} = \frac{\left(\varepsilon_{\alpha} - \varepsilon_{\alpha 0}\right)^{q} a_{\alpha}^{2}}{8} \tag{36}$$

where ε_{α} is the void fraction of layer α, $\varepsilon_{\alpha 0}$ is the percolation threshold, q is the critical or Bruggeman exponent (1.5), and a_{α} is the mean pore radius of the media.

By summing over all species present in the porous media, the following result is obtained:

$$\left[\nabla p + \left(\sum_{j=1}^{n} c_j z_j\right) F \cdot \nabla \phi\right] = -\frac{RT}{W} \sum_{j=1}^{n} \frac{N_i}{D_{jM}^{e}} \tag{37}$$

$$\text{where } W = 1 + \frac{B_0 cRT}{\mu} \sum_{h=1}^{n} \frac{x_h}{D_{hM}^{e}} \tag{38}$$

By substituting Equation (37) into Equation (32) an alternative form of the DFM results. This representation involves the driving forces on the left hand side of the equation and the species fluxes on the right hand side:

$$-\frac{c_i}{RT} \nabla_T \mu_i^{e} = \sum_{\substack{j=1 \\ j \neq i}}^{n} \frac{1}{c D_{ij}^{e}} \left(c_j N_i - c_i N_j\right) + \frac{N_i}{D_{iM}^{e}} - \frac{c_i B_0 RT}{\mu D_{iM}^{e} W} \sum_{j=1}^{n} \frac{N_j}{D_{jM}^{e}}$$

$$\left(\, i = 1,2,\ldots n \right) \tag{39}$$

Equation (39) can be written in an alternative form since the flux ratio $\left(N_j / N_i\right)$ is known for this system. Substituting the flux ratio into Equation (39), the resultant Fickian form is Equation (40).

$$N_i = -\frac{1}{RT} D_i^e c_i \nabla_T \mu_i^e$$

$$(i = 1,2,\ldots n) \tag{40}$$

Where the effective diffusivity of species *i* is:

$$\frac{1}{D_i^e} = \sum_{\substack{j=1 \\ j \neq i}}^{n} \frac{1}{c D_{ij}^e} \left(c_j - c_i \frac{N_j}{N_i} \right) + \frac{1}{D_{iM}^e} - \frac{c_i B_0 RT}{\mu D_{iM}^e W} \sum_{j=1}^{n} \frac{1}{D_{jM}^e} \frac{N_j}{N_i}$$

$$(i = 1,2,\ldots n) \tag{41}$$

DUSTY FLUID MODEL APPLIED TO THE CATHODE PLAQUE

To facilitate the modeling of transport in the cathode plaque, a specialized form of the DFM is utilized. Thus, the Dusty Gas Model (DGM) accounts for gaseous species transport in porous media. The driving force for gas phase transport is the partial pressure gradient

$$c_i \nabla_T \mu_i^e = \nabla p_i \tag{42}$$

For this specialized form of the DFM, the diffusion coefficient accounting for species interaction with the porous media is equivalent to the Knudsen diffusion, or

$$D_{iM}^e = D_{iK}^e \tag{43}$$

The effective diffusivity for partially liquid filled porous layers is

$$D_{i\alpha}^e = \left(1 - q_w\right)^q D_{iG}^e + q_w^q \kappa_{iL} K_1 D_{iL} \approx \left(1 - q_w\right)^q D_{iG}^e \tag{44}$$

with q defined as the critical exponent (1.5), D_{iL} defined as the liquid phase diffusivity of species i, and D_{iG}^{e} defined as the effective diffusivity for the dry porous layer.

Rewriting Equation (40) in terms of partial pressures and substituting Equation (44) yields:

$$\frac{1}{D_{iC}^{e}} = \sum_{\substack{j=1 \\ j\neq i}}^{n} \frac{1}{D_{ij}^{e0}} \left(p_j - p_i \frac{N_j}{N_i} \right) + \frac{1}{D_{iK}^{e}} - \frac{p_i B_0}{\mu D_{iK}^{e} W} \sum_{j=1}^{n} \frac{1}{D_{jK}^{e}} \frac{N_j}{N_i}$$

$$(i = 1,2,\ldots n) \tag{45}$$

The diffusion coefficients here are defined as

$$D_{ij}^{e0} \equiv pD_{ij}^{e} = pK_1 D_{ij} = (\varepsilon_\alpha - \varepsilon_{\alpha 0})^q \, pD_{ij} \tag{46}$$

$$D_{iK}^{e} = K_0 \sqrt{\frac{8RT}{\pi M_i}} \tag{47}$$

$$\text{with } K_0 = (\varepsilon_\alpha - \varepsilon_{\alpha 0})^q \left(\frac{2a_\alpha}{3} \right) \tag{48}$$

Since air is the diffusing gas, the main species of transport are oxygen (O_2) and nitrogen (N_2) as they are the most abundant constituents of the atmosphere. However, carbon dioxide (CO_2) is included in this model since its presence has a deleterious effect on cell performance. In addition, water vapor may be present and has the ability to diffuse into the cell during conditions of high relative humidity external to the cell. It is, however, assumed that the PTFE layers in the cell construction adequately prevent water vapor transfer and thus N_w is zero. It is also assumed that the flux of N_2 and CO_2 into the anode cell compartment is zero ($N_{N_2} = N_{CO_2} = 0$), since N_2 is inert and the flux of CO_2 is small. The basis for these assumptions are discussed at length with Chapter II.

Using these assumptions in conjunction with Equation (45) yields an expression for the overall diffusion coefficient of oxygen in the cathode plaque:

$$\frac{1}{D_{iC}^{e}}=\frac{p_{w}}{D_{O_2 iw}^{e0}}+\frac{p_{N_2}}{D_{O_2 N_2}^{e0}}+\frac{p_{CO_2}}{D_{O_2 CO_2}^{e0}}+\frac{1}{D_{O_2 K}^{e}}\left\{\frac{1+\frac{B_0}{\mu}\left(\frac{p_w}{D_{wK}^{e}}+\frac{p_{N_2}}{D_{N_2 K}^{e}}+\frac{p_{CO_2}}{D_{CO_2 K}^{e}}\right)}{1+\frac{B_0}{\mu}\left(\frac{p_{O_2}}{D_{O_2 K}^{e}}+\frac{p_w}{D_{wK}^{e}}+\frac{p_{N_2}}{D_{N_2 K}^{e}}+\frac{p_{CO_2}}{D_{CO_2 K}^{e}}\right)}\right\} \tag{49}$$

For application to the mathematical simulations, the terms associated with Carbon Dioxide in Equation (49) will be neglected since the partial pressure contributions associated with it are negligible in the atmosphere.

NOTIONS IN ELECTRODE KINETICS

The overall charge balance for an electrode reaction is

$$\sum_{\substack{i=1\\ i=e^-}}^{n}\nu_{\rho i}z_i=\nu_{\rho e^-} \tag{50}$$

For elementary reactions, the net rate per unit of active material or supported catalyst surface area via Thermodynamic Transition State Theory (TTST) is[43]

$$r_{\rho}^{*}=\vec{r}_{\rho}^{\,*}-\overleftarrow{r}_{\rho}^{\,*}=\vec{k}_{\rho}^{\,*}\prod_{i=r+1}^{n}a_i^{\nu_{\rho i}}-\overleftarrow{k}_{\rho}^{\,*}\prod_{i=r+1}^{n}a_i^{\nu_{\rho i}} \tag{51}$$

The rate constants are defined as

$$\vec{k}_{\rho}^{\,*}=\vec{k}_{\rho\Phi 0}^{\,*}\exp\left\{\frac{\beta_{\rho}\nu_{\rho e^-}F\eta}{RT}\right\} \tag{52}$$

$$\overleftarrow{k}_{\rho}^{\,*}=\overleftarrow{k}_{\rho\Phi 0}^{\,*}\exp\left\{\frac{(\beta_{\rho}-1)\nu_{\rho e^-}F\eta}{RT}\right\} \tag{53}$$

Both of these constants are dependent upon the overpotential, $\eta(\equiv \Phi - \Phi_0)$, associated with the electrode. The overpotential is a measure of the deviation of observed potential from theoretical potential for the electrode in question. Another term introduced in the equations defining the reaction rate constants is the symmetry factor, β_p, which is assumed to be equal to ½ for elementary reactions. These constants also exhibit the usual Arrhenius dependence upon the temperature of operation.

The equilibrium constant for the elementary reaction is

$$K_\rho = \frac{\vec{k}_\rho}{\overleftarrow{k}_\rho} = k_{\rho\Phi} \exp\left\{\frac{\nu_{\rho e^-} F\eta}{RT}\right\} \tag{54}$$

As with the reaction rate constants for the forward and reverse reactions previously presented, there is a strong dependence upon electrode overpotential and temperature for the equilibrium constant as well.

Under open circuit conditions, the overpotential and the net rate of the reaction are defined to be zero. Combining this notion with Equations (51), (52), and (53) yields:

$$\vec{r}^{\,*}_{\rho 0} = \vec{k}^{\,*}_\rho \prod_{i=r+1}^{n} a_i^{\nu_{\rho i}} = \overleftarrow{r}^{\,*}_{\rho 0} = \overleftarrow{k}^{\,*}_\rho \prod_{i=r+1}^{n} a_i^{\nu_{\rho i}} \tag{55}$$

Re-writing the relations in Equation (55) in Butler-Volmer form gives:

$$\begin{aligned} r^*_\rho &= \vec{r}^{\,*}_{\rho 0}\left[\exp\left\{\frac{\beta_\rho \nu_{\rho e^-} F\eta}{RT}\right\} - \exp\left\{\frac{(\beta_\rho - 1)\nu_{\rho e^-} F\eta}{RT}\right\}\right] \\ &= \overleftarrow{r}^{\,*}_{\rho 0}\left[\exp\left\{\frac{\beta_\rho \nu_{\rho e^-} F\eta}{RT}\right\} - \exp\left\{\frac{(\beta_\rho - 1)\nu_{\rho e^-} F\eta}{RT}\right\}\right] \end{aligned} \tag{56}$$

In a pseudo-irreversible form, Equation (56) can be re-written as:

$$\vec{r}^{\,*}_\rho = \vec{k}^{\,*}_\rho \prod_{i=r+1}^{n} a_i^{\nu_{\rho i}} \tag{57}$$

$$\text{with } k_{\rho}^{*} = \vec{k}_{\rho\Phi 0}^{*}\left[\exp\left\{\frac{\beta_{\rho}\nu_{\rho e^-}F\eta}{RT}\right\} - \exp\left\{\frac{(\beta_{\rho}-1)\nu_{\rho e^-}F\eta}{RT}\right\}\right] \tag{58}$$

Since the reactions are defined to be elementary and β_{ρ} is equal to ½, Equation (58) can alternatively be re-written as:

$$k_{\rho}^{*} = \vec{k}_{\rho\Phi 0}^{*}\left[2\sinh\left\{\frac{\nu_{\rho e^-}F\eta}{2RT}\right\}\right] \tag{59}$$

The current density (A/cm^2) based upon surface area of active material takes the following form:

$$i^{*} = F\sum_{\substack{i=1 \\ i\neq e^-}}^{n} z_i N_i^{*} \tag{60}$$

Assuming that there are no diffusional limitations associated in the electrode being analyzed, Equation (60) can be written as:

$$i^{*} = Fr_{\rho}^{*}\sum_{\substack{i=1 \\ i\neq e^-}}^{n} z_i \nu_{\rho e^-} \tag{61}$$

Since there is an overall charge balance associated with the specified electrode reaction Equation (50), Equation (61) takes the form

$$i^{*} = F\nu_{\rho e^-}r_{\rho}^{*} \tag{62}$$

The exchange current density for the electrode being modeled thus is written as:

$$i_0^{*} = F\nu_{\rho e^-}\vec{r}_{\rho 0}^{*} \tag{63}$$

The roughness factor was first introduced by Murkerjee et al. and is universally employed for the modeling of fuel cells.[44] For this analysis, it is utilized for the prediction of Zn/Air cell performance. The roughness factor is defined as

$$\gamma_M = \varphi_I m_M \left(\frac{6\varphi_M}{\rho_M d_M} \right) \tag{64}$$

Multiplying the current densities per surface area of active material Equations (62) and (63) by the roughness factor yields the current densities on an electrode geometric surface are basis

$$i = \gamma_M i^* \tag{65}$$

$$i_0 = \gamma_M i_0^* \tag{66}$$

By taking the ratio of Equation (65) to Equation (66), a relationship between current densities and overpotential is derived. This relationship is as follows:

$$\frac{i}{i_0} = \frac{\gamma_M i^*}{\gamma_M i_0^*} = \frac{i^*}{i_0^*} = \frac{F\nu_{\rho e^-} r_{\rho 0}^*}{F\nu_{\rho e^-} \vec{r}_{\rho 0}^*} = \frac{r_{\rho 0}^*}{\vec{r}_{\rho 0}^*} = \left[2\sinh\left\{ \frac{\nu_{\rho e^-} F\eta}{2RT} \right\} \right] \tag{67}$$

DEFINITION OF TRANSPORT REGIONS

In order to apply the previously discussed concepts to Zn/Air cells, it is necessary to describe the transport regions in the assembled Zn/Air cell, as done in Figure III-1. Each region will be discussed in the context of the application transport and kinetic principles discussed above

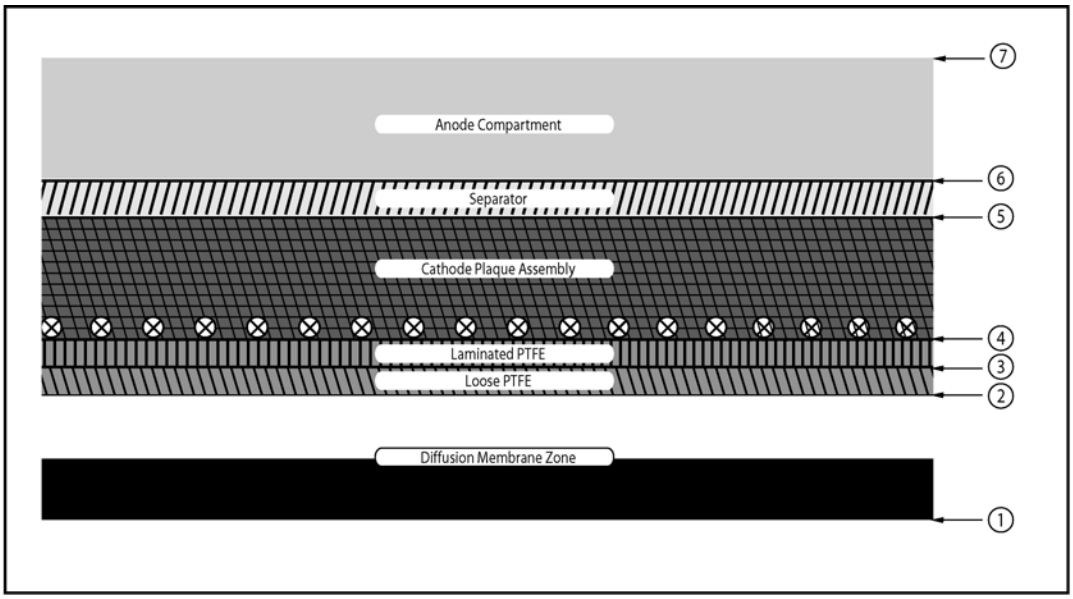

Figure III-2: Defined transport regions for modeling work.

REACTION KINETICS AT THE CATHODE

As discussed in Chapter II, the electrochemical reduction of oxygen in alkaline solutions is a multi-step reaction. We are interested in a simplified rate expression for the overall cathode reduction reaction, i.e.,

$$O_2 + 2H_2O + 4e^- \rightarrow 4OH^- \quad (16)$$

This accomplished utilizing the rate determining step for the cathode reduction reaction. It is assumed that the proposed RDS for the oxygen reduction reaction is Reaction (24) i.e.,[3]

$$O_2^- + H_2O \rightarrow HO_2^- + OH \quad (24)$$

The objective here is to derive a rate expression for the overpotential of the cathodic electrode of a Zn/Air cell. In order to achieve this, some assumptions are made as follows:

(1) The rate determining step for the cathode reduction reaction via the direct 4-electron reaction mechanism is assumed to be Reaction (24).

(2) No potential drop occurs across the cathode plaque structure.

(3) No diffusional limitations exist in the cathode plaque structure.

(4) Water comprised in the electrolyte solely aids in the transport of hydroxyl ions (OH^-).

(5) Water vapor ingress to the cell is effectively managed (no flux) and thus there is no deleterious effect on overall cell performance.

(6) Electroneutrality is valid for electrolyte that has penetrated into the cathode plaque structure and assisting with cell discharge.

Utilizing the assumptions presented in the defined cathode transport regions (Figure III-1) yields an expression for O_2 concentration:

$$c_{O_2,C} = c_{O_2,C}(2) = c_{O_2,C}(6) \tag{68}$$

Assuming that the reaction at the cathode is step-wise with a single electron in each step with one being rate limiting and that kinetics are first order, then a rate expression for the cathode reaction, in moles per cm^2 of cathode catalyst, is:

$$r_C^* = \left[\vec{k}_C^* c_{O_2^-,C} c_{H_2O,C} \exp\left(\frac{\vec{\alpha}_C F\eta}{RT}\right)\right] - \left[\overleftarrow{k}_C^* c_{OH_2^-,C} \overleftarrow{k}_C^* c_{OH,C} \exp\left(\frac{\overleftarrow{\alpha}_C F\eta}{RT}\right)\right] \tag{69}$$

The initial step of the reaction mechanism allows for the determination of a relation between oxygen concentration and superoxide concentration assuming pseudo-equilibrium

$$\vec{k}_1 c_{O_2,C} = \overleftarrow{k}_1 c_{O_2^-,C} \tag{70}$$

and rearranging for superoxide concentration

$$c_{O_2^-,C} = \mathrm{K}_1 c_{O_2,C} \tag{71}$$

where $\mathrm{K}_1 = \vec{k}_1 / \overleftarrow{k}_1$. Substituting Equation (71), and writing in pseudo-irreversible form[39], assuming constant concentration of water, and incorporation of oxygen adsorption equilibrium constant in the overall reaction constant, Equation (69) takes the form:

$$r_C^* = \vec{k}_C^* c_{O_2,C} \tag{72}$$

with

$$k_C^* = \vec{k}_{C,\Phi_c}^* \left\{2\sinh\left(\frac{\vec{\alpha}_C F\eta_C}{RT}\right)\right\} \tag{73}$$

The current and exchange current densities for the overall cathode reaction can be written utilizing Equations (62) and (63). With ν_{Ce^-} equal to +4, then the cathodic current densities are written as:

$$i_C^* = 4Fr_C^* \tag{74}$$

$$i_{C0}^* = 4F\vec{r}_C^* \tag{75}$$

The reference exchange current density is defined as follows

$$i_{C,0,ref} = 4F\vec{k}_{C,\Phi_0}(T_{ref})c_{O_2,ref} \tag{76}$$

The current densities discussed can be converted to a cathode geometric surface area basis by incorporating the cathode roughness factor, $\gamma_{M,C}$

$$i_C = \gamma_{MC} i_C^* \tag{77}$$

$$i_{C0} = \gamma_{MC} i_{C0}^* \tag{78}$$

The cathode current and exchange current densities, A/cm^2, can now be written as:

$$i_C = \gamma_{M,C} 4Fk_C^* c_{O_2,C} \tag{79}$$

and

$$i_{C0} = \gamma_{M,C} 4Fk_{C,0}^* c_{O_2,C} \tag{80}$$

The partition coefficient is defined as

$$\kappa_{O_2,C} = \frac{c_{O_2,C}}{c_{O_2,T}} \tag{81}$$

By solving for the oxygen concentration and substituting into Equation (79), an alternative form results

$$i_C = \gamma_{M,C} 4Fk_C^* \kappa_{O_2,C} c_{O_2,T} \tag{82}$$

The reaction rate can also be re-written in terms of the cathode area, with units of moles per cm^2 cathode per second

$$r_C = \gamma_{M,C} r_C^* = \gamma_{M,C} k_C^* c_{O_2,C} \tag{83}$$

Using the concept of cathode catalyst roughness factor, the rate of O_2 consumption with units of moles O_2 per cm^2 cathode per second, is as follows:

$$\text{Rate of } O_2 \text{ Consumption} = \nu_{C,O_2} \gamma_{M,C} \tag{84}$$

The rate of O_2 transferred over the cathode catalyst, in moles O_2/cm^3 catalyst·sec, is:

$$r_C^{'} = \frac{\nu_{C,O_2} r_C}{L_c} \tag{85}$$

where L_C is the cathode structure thickness.

This is also the flux of O_2 and can be re-written as:

$$\frac{dN_{O_2}}{dx} = r_C^{'} \tag{86}$$

Rearranging and integrating over the cathode structure thickness:

$$\int_d^{e_s} dN_{O_2,x} = \frac{\nu_{C,O_2} r_C}{L_c} \int_d^e dx \tag{87}$$

$$N_{O_2,x_s} - N_{O_2,x_C} = \nu_{C,O_2} r_C \tag{88}$$

Assuming that the electrolyte is impervious to O_2:

$$N_{O_2,x_C} = -\nu_{C,O_2} \gamma_{M,C} k_C c_{O_2,C} = P_{O_2} \left\{ c_{O_2,atm} - \frac{c_{O_2,C}}{\kappa_{O_2,C}} \right\} \tag{89}$$

where P_{O_2} is the permeability of O_2 in the cathode structure.

Rearranging for O_2 concentration:

$$c_{O_2,C} = \frac{\kappa_{O_2,C} c_{O_2,atm}}{1 + \frac{\nu_{O_2,C}\gamma_{M,C} k_C^* \kappa_{O_2,C}}{P_{O_2}}} \tag{90}$$

Substituting Equation (90) into Equation (79):

$$i_C = \frac{\gamma_{M,C}\nu_{C,e^-} F k_C^* \kappa_{O_2,C} c_{O_2,atm}}{1 + \frac{(-\nu_{O_2,C})\gamma_{M,C} k_C^* \kappa_{O_2,C}}{P_{O_2}}} \tag{91}$$

By neglecting unity in the denominator of Equation (91) facilitates the mathematical definition of the limiting current density:

$$i_{CL} = \left(\frac{\nu_{C,e^-}}{-\nu_{C,O_2}}\right) F P_{O_2} c_{O_2,atm} \tag{92}$$

The ratio of current density to limiting current density is:

$$\frac{i_C}{i_{CL}} = \left(\frac{-\nu_{C,O_2}}{P_{O_2}}\right)\gamma_{MC} k_C^* \kappa_{O_2,C} \Bigg/ \left\{1 + \left(\frac{-\nu_{C,O_2}}{P_{O_2}}\right)\gamma_{MC} k_C^* \kappa_{O_2,C}\right\} \tag{93}$$

Rearranging

$$\left(\frac{-\nu_{C,O_2}}{P_{O_2}}\right)\gamma_{M,C} k_C^* \kappa_{O_2,C} = \frac{\frac{i_C}{i_{CL}}}{1 - \frac{i_C}{i_{CL}}} \tag{94}$$

In addition,

$$\frac{i_{C0}}{i_{CL}} = \left(\frac{-\nu_{C,O_2}}{P_{O_2}}\right)\gamma_{M,C} \vec{k}_{C,\Phi_0} \kappa_{O_2,C} \tag{95}$$

and

$$\frac{k_C^*}{\vec{k}_{C,\Phi_0}^*} = \frac{i_{C0}}{i_{CL}} = \frac{\frac{i_C}{i_{C0}}}{1 - \frac{i_C}{i_{CL}}} \tag{96}$$

The ratio of the reaction coefficients also can be written as

$$\frac{k_C}{\vec{k}_{C,\Phi_0}} = 2\sinh\left(\frac{\vec{\alpha}_C F \eta_c}{RT}\right) = \frac{\frac{i_C}{i_{C0}}}{1-\frac{i_C}{i_{CL}}} \tag{97}$$

Thus solving for cathode overpotential

$$-\eta_C = \frac{RT}{\vec{\alpha}_C F}\sinh^{-1}\left[\frac{1}{2}\left\{\frac{i_C}{i_{C0}}\Big/\left[1-\left(\frac{i_C}{i_{CL}}\right)\right]\right\}\right] \tag{98}$$

In addition, the exchange current density may be written as

$$i_{C,0} = i_{C,0,ref}\left(\frac{c_{O_2}}{c_{O_2,ref}}\right)\exp\left[-\frac{E_{C,\Phi_0}}{R}\left(\frac{1}{T}-\frac{1}{T_{ref}}\right)\right] \tag{99}$$

REACTION KINETICS AT THE ANODE

As discussed in Chapter II, the electrochemical oxidation of zinc in alkaline solutions is also a multi-step reaction. For this analysis, however, we are interested in a simplified rate expression for the overall anode oxidation reaction, i.e.,

$$2Zn + 4OH^- \rightarrow 2ZnO + 2H_2O + 4e^- \tag{3}$$

For this the rate determining step for the overall anode oxidation reaction is utilized, i.e.,[53]

$$Zn(OH)_2^- + OH^- \rightarrow Zn(OH)_3^- + e^- \tag{8}$$

The objective here is to derive a simplified rate expression to predict the overpotential of the anodic electrode of a Zn/Air cell. In order to achieve this, the following assumptions are made

(1) Only the proposed rate determining step for the overall anode oxidation reaction [Reaction (8)] is considered for zinc oxidation.

(2) No potential drop across anode slurry, i.e., no diffusional limitations exist in the slurry.

(3) Stoichiometric equivalents of hydroxyl ions (OH^-) are present in the anode compartment to facilitate the reaction.

(4) No deleterious side reactions occur with the anode compartment (i.e., direct oxidation or carbonation of the electrolyte).

(5) Electroneutrality is valid for electrolyte that has penetrated into the cathode plaque structure and assisting with cell discharge.

Utilizing the assumptions presented in the defined anode transport regions (Figure III-1) yields an expression for OH^- concentration:

$$c_{OH^-,A} = c_{OH^-,A}(6) = c_{OH^-,A}(7) \tag{100}$$

Assuming that the reaction at the anode reaction is also step-wise and first order, then a rate expression for the anode reaction, in moles per cm^2 of anode actives, is:

$$r_A^* = \left[\vec{k}_A^* c_{Zn(OH)_2^-,A} c_{OH^-,A} \exp\left(\frac{\vec{\alpha}_A F\eta}{RT}\right)\right] - \left[\vec{k}_A^* c_{Zn(OH)_3^-,A} \exp\left(\frac{\vec{\alpha}_A F\eta}{RT}\right)\right] \tag{101}$$

Writing in pseudo-irreversible form[39], and incorporating the concentration of $Zn(OH)_2^-$ at the surface within the rate constant, Equation (101) takes the form:

$$r_A^* = k_A^* c_{OH^-,A} \tag{102}$$

with

$$k_A^* = \vec{k}_{A,\Phi_\circ}^* \left\{ 2\sinh\left(\frac{\vec{\alpha}_A F \eta_A}{RT} \right) \right\} \tag{103}$$

The current and exchange current densities for the overall cathode reaction can be written utilizing Equations (62) and (63). With ν_{Ae^-} equal to +4, then the anodic current densities are written as:

$$i_A^* = 4Fr_A^* \tag{104}$$

$$i_{A0}^* = 4F\vec{r}_A^* \tag{105}$$

The reference exchange current density is defined as follows:

$$i_{A0,ref}^* = 4F\vec{k}_{A,\Phi_0}(T_{ref})c_{OH^-,ref} \tag{106}$$

The current densities discussed can be converted to a anodic geometric surface area basis by incorporating the anode roughness factor, γ_{MA}:

$$i_A = \gamma_{MA} i_A^* \tag{107}$$

$$i_{A0} = \gamma_{MA} i_{A0}^* \tag{108}$$

The anode roughness factor also accounts for the amount of reacted zinc, or zinc converted to intermediate species. This factor is an adjustment to the overall mathematical model based upon the accessibility/inaccessibility to zinc. As the zinc is resting in anode compartment, particles are essentially resting on one another and preventing ease of access to unreacted zinc. This factor increases over time as the zinc radius reduces, having a more detrimental impact on anodic overpotential.

The anode current and exchange current densities, A/cm^2, can now be written as:

$$i_A = \gamma_{MA} 4Fk_A^* c_{OH^-,A} \tag{109}$$

and

$$i_{A0} = \gamma_{MA} 4Fk^{*}_{A,0} c_{OH^-,A} \tag{110}$$

The partition coefficient is defined as:

$$\kappa_{OH^-,S} = \left(\frac{c_{OH^-}}{c_{OH^-,B}} \right)_{eq} \tag{111}$$

The pseudo steady state material balance on OH^- diffusing to the Zn particle surface is

$$\frac{d}{dr}\left(r^2 N_{OH^-,r}\right) = 0 \tag{112}$$

Integrating Equation (112) with the boundary condition of $r^2 N_{OH^-,r} = 0$ at $r = 0$ yields

$$r^2 N_{OH^-,r} = k_1 \tag{113}$$

Substituting Equation (113) into Fick's Law and rearranging results in

$$r^2 \frac{dc_{OH^-}}{dr} = -\frac{k_1}{D_{OH^-,S}} \tag{114}$$

Rearranging and integrating the concentration and radial terms yields

$$c_{OH^-,0} - c_{OH^-,r} = \frac{k_1}{D_{OH^-,S}} \left(\frac{1}{R_0} - \frac{1}{r} \right) \tag{115}$$

Evaluating Equations (115) and (113) at the reaction surface yields

$$c_{OH^-,0} - c_{OH^-,R} = \frac{k_1}{D_{OH^-,S}} \left(\frac{1}{R_0} - \frac{1}{R} \right) \tag{116}$$

and

$$R^2 N_{OH^-,R} = k_1 \tag{117}$$

Substituting Equation (117) into Equation (116) and solving for $N_{OH^-,R}$ yields

$$N_{OH^-,R} = \frac{D_{OH^-,S}\left(c_{OH^-,0} - c_{OH^-,R}\right)}{R^2\left(\frac{1}{R_0} - \frac{1}{R}\right)} \tag{118}$$

Utilizing Equation (111) in Equation (118) results in

$$N_{OH^-,R} = \frac{D_{OH^-,S}\kappa_{OH^-,S}\left(c_{OH^-,B} - \left\{\frac{c_{OH^-,R}}{\kappa_{OH^-,S}}\right\}\right)}{R^2\left(\frac{1}{R_0} - \frac{1}{R}\right)} \tag{119}$$

The interfacial reaction rate at the Zn particle surface is

$$N_{OH^-,R} = -\nu_{A,OH^-}k_A^* c_{OH^-,R} \tag{120}$$

Equation Equations (119) and (120) and solving for OH^- concentration at the Zn particle surface yields

$$c_{OH^-,R} = \frac{\kappa_{OH^-,S}c_{OH^-,B}}{1 + \frac{(-\nu_{OH^-,A})k_A^*\kappa_{OH^-,S}}{\left(\frac{R}{R_0}\right)^2 P_{OH^-,A}}} \tag{121}$$

where $P_{OH^-,A}$ is the permeability of OH^- in the ash layer and is defined as

$$P_{OH^-,A} \equiv \frac{D_{OH^-,S}\kappa_{OH^-,S}}{R_0^{\,2}\left(\frac{1}{R} - \frac{1}{R_0}\right)} \tag{122}$$

Substituting Equation (121) into Equation (109):

$$i_A = \frac{\gamma_{MA}\nu_{A,e^-}Fk_A^*\kappa_{OH^-,S}c_{OH^-,B}}{1 + \frac{(-\nu_{A,OH^-})\gamma_{MA}k_A^*\kappa_{OH^-,A}}{P_{OH^-,A}}} \tag{123}$$

By neglecting unity in the denominator of Equation (121) facilitates the mathematical definition of the limiting current density:

$$i_{AL} = \left(\frac{\nu_{A,e^-}}{-\nu_{A,OH^-}} \right) F \gamma_{MA} P_{OH^-,A} c_{OH^-,B} \tag{124}$$

The ratio of current density to limiting current density is:

$$\frac{i_A}{i_{AL}} = \left\{ \left(\frac{-\nu_{A,OH^-}}{P_{OH^-,A}} \right) \left(\frac{R}{R_0} \right)^2 \gamma_{MA} k_A^* \kappa_{OH^-,S} \right\} \Bigg/ \left\{ 1 + \left(\frac{-\nu_{A,OH^-}}{P_{OH^-,A}} \right) \left(\frac{R}{R_0} \right)^2 \gamma_{MA} k_A^* \kappa_{OH^-,S} \right\} \tag{125}$$

Rearranging:

$$\left(\frac{-\nu_{A,OH^-}}{P_{OH^-,A}} \right) \gamma_{MA} \left(\frac{R}{R_0} \right)^2 k_A^* \kappa_{OH^-,S} = \frac{\frac{i_A}{i_{AL}}}{1 - \frac{i_A}{i_{AL}}} \tag{126}$$

In addition,

$$\frac{i_{A0}}{i_{AL}} = \left(\frac{-\nu_{A,OH^-}}{P_{OH^-,A}} \right) \gamma_{MA} \left(\frac{R}{R_0} \right)^2 \vec{k}_{A,\Phi_0} \kappa_{OH^-,S} \tag{127}$$

and

$$\frac{k_A^*}{\vec{k}_{A,\Phi_0}^*} = \frac{i_{A0}}{i_{AL}} = \frac{\frac{i_A}{i_{A0}}}{1 - \frac{i_A}{i_{AL}}} \tag{128}$$

The ratio of the reaction coefficients also can be written as:

$$\frac{k_A}{\vec{k}_{A,\Phi_0}} = 2 \sinh\left(\frac{\vec{\alpha}_A F \eta_A}{RT} \right) = \frac{\frac{i_A}{i_{A0}}}{1 - \frac{i_A}{i_{AL}}} \tag{129}$$

and solving for anode overpotential:

$$\eta_A = \frac{RT}{\bar{\alpha}_A F} \sinh^{-1}\left[\frac{1}{2}\left\{\frac{i_A}{i_{A0}} \Big/ 1 - \frac{i_A}{i_{AL}}\right\}\right] \tag{130}$$

OVERPOTENTIAL IN THE ELECTROLYTE

The change in current throughout the electrolyte is constant. Thus,

$$\frac{di}{dz} = 0 \tag{131}$$

and

$$i = -\sigma_{OH^-} \frac{d\phi_s}{dz} \tag{132}$$

Integrating across the "thickness" of the electrolyte

$$i = \frac{\sigma_{OH^-}}{L_{KOH}} \left\{\phi_{s,KOH}(2) - \phi_{s,KOH}(1)\right\} \tag{133}$$

Rearranging gives:

$$\left\{\phi_{s,KOH}(2) - \phi_{s,KOH}(1)\right\} = i\left(\frac{L_{KOH}}{\sigma_{KOH}}\right) \tag{134}$$

In Equation (133), L_{KOH} is the effective thickness of the electrolyte, i.e., the average distance that the OH^- ions must be transported from the cathode to the anode. This, of course, is a function of current density and the depth of discharge. Here it is assumed that the transport resistance lies in the separator layer, i.e., $L_{KOH} = L_{Sep}$.

OVERALL CELL VOLTAGE EXPRESSION

Now that the overpotential equations have been developed for the anode, cathode, and electrolyte, the overall expression for a Zn/Air primary cell can be written.

$$V = \frac{1}{F}\left\{\mu^e_{e^-,A} - \mu^e_{e^-,C}\right\} = \frac{1}{F}\left\{\left(\mu_{e^-,A} + (-1)F\phi_{M,A}\right) - \left(\mu_{e^-,C} + (-1)F\phi_{M,C}\right)\right\} = \phi_{M,C} - \phi_{M,A} \tag{135}$$

Electrode Potential

$$\Phi_M = \phi_M - \phi_S \tag{136}$$

$$V = \left(\Phi_{M,C} + \phi_{S,C}\right) - \left(\Phi_{M,A} + \phi_{S,A}\right) \tag{137}$$

where

$$\Phi_M = \Phi_{0,M} + \eta_M \tag{138}$$

and the Open Circuit Voltage (OCV)

$$V_\circ = \Phi_{0,C} - \Phi_{0,A} \text{ (Open Circuit Voltage)} \tag{139}$$

Then,

$$V = \left(\Phi_{0,C} - \Phi_{0,A}\right) + \eta_C - \eta_A - \left(\phi_{S,A} - \phi_{S,C}\right) = V_0 + \eta_C + \eta_A - \left(\phi_{S,A} - \phi_{S,C}\right) \tag{140}$$

With the interfacial resistance,

$$\left(\phi_{S,A} - \phi_{S,C}\right) = \left\{\phi_{S,A} - \phi_{S,B}(1)\right\} + \left\{\phi_{S,B}(1) - \phi_{S,B}(2)\right\} + \left\{\phi_{S,B}(2) - \phi_{S,C}\right\} = iR_I \tag{141}$$

The final form of the overall equation based upon Butler-Volmer Reaction Kinetics can now be written as:

$$V = V_0 - \eta_A + \eta_C - i\left(\frac{L_{KOH}}{\sigma_{KOH}}\right) - iR_I \tag{142}$$

Where $i\left(\frac{L_{KOH}}{\sigma_{KOH}}\right) - iR_I$ is the combination of losses in the electrolyte as well as interfacial resistances, which leads to Ohmic drop in voltage. The electrolyte losses are a function of time. However, these effects in relative comparison to the overall anodic losses are minimal as presented in the work of Mao and White.[40]

Inclusion of the equations developed throughout this chapter leads to a final current density dependent voltage equation

$$V = V_0 - \frac{RT}{\vec{\alpha}_A F}\sinh^{-1}\left[\frac{1}{2}\left\{\frac{i_A}{i_{A,0}}\Big/1-\frac{i_A}{i_{A,L}}\right\}\right] - \frac{RT}{\vec{\alpha}_C F}\sinh^{-1}\left[\frac{1}{2}\left\{\frac{i_C}{i_{C,0}}\Big/1-\frac{i_C}{i_{C,L}}\right\}\right] - i\left(\frac{L_{KOH}}{\sigma_{KOH}}\right) - iR_I \quad (143)$$

SHRINKING CORE REACTION KINETICS AND TIME-DEPEDENT ANODIC OVERPOTENTIAL

The shrinking core reaction kinetic model was employed for the development of the time-dependent performance prediction model. This approach models the zinc particles as spheres whose active radii are shrinking as the electrochemical oxidation reaction consumes the zinc during cell discharge. Similar approaches have been employed in the modeling of Zn-MnO_2 as well as Li-MnO_2 cells, but not directly stated as the approach.[46] In conjunction with the shrinking zinc core radii, an inert zinc oxide film is formed on the surface of active Zn. This layer is referred to as the generically as the ash layer and electrochemically as passivation.[45] The passivation of zinc, on a microscopic level, reduces the cell potential by increasing the resistance to mass transport of OH^- to unreacted zinc. In addition, the development of this layer leads to greater electronic conductivity losses to the current collector since ZnO is much less conductive than Zn. This subsequently leads to a voltage drop and a reduction in cell capacity as well. At the anode, the ash layer formation is also accompanied by a reduction in porosity (or void volume) of the anode compartment. This is due to the increase in partial molar volume associated with the conversion of Zn to ZnO. This process is schematically represented in Figure III-2.

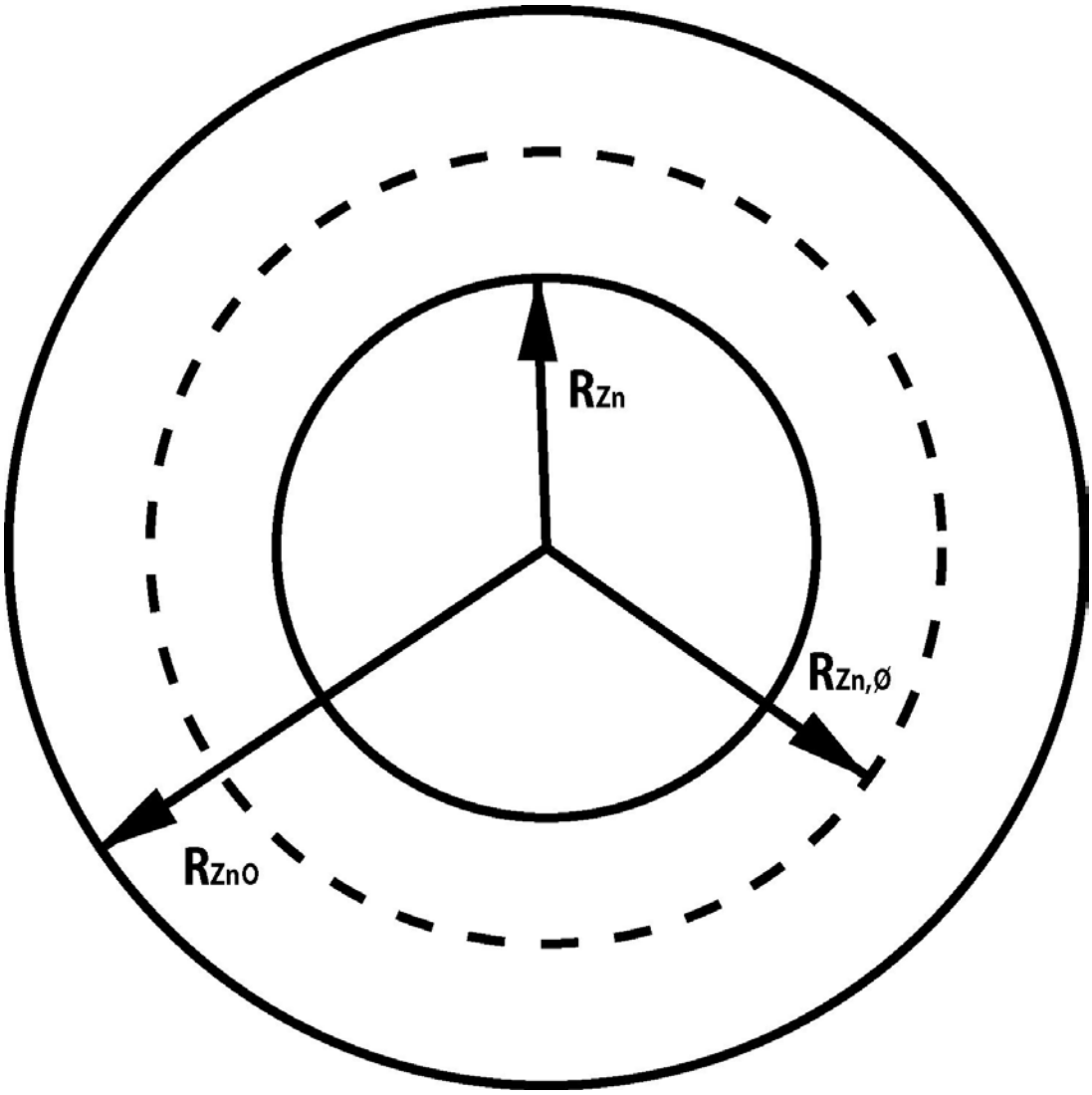

Figure III-3: Representation of theoretical shrinking Zn core for time-dependent anode modeling.

.

The pseudo-steady-state material balance for the OH^- ion in the reacted ash layer surrounding particles of active materials (core) in the electrodes is written as

$$\frac{1}{r^2}\frac{d}{dr}\left(r^2 N_{OH^-}\right)=0 \tag{144}$$

where

$$N_{OH^-} = -D^e_{OH^-,A}\frac{dc_{OH^-}}{dr} \tag{145}$$

Application of the material balance (and all subsequent development with the reactive core/reacted ash layer) assumes spherical geometry. In practice the zinc particles are typically more oblong in shape. However, this assumption is useful since it provides a good approximation and allows analytic solution. The rate of reaction per unit volume of active material (Zn) is r''_{ρ} and $D^e_{OH^-,A}$ is the effective diffusion coefficient of OH^- in the ash layer.

The solution to the flux in the ash layer at the core surface ($r = R$) is obtained by integrating the Fickian flux equation for constant effective diffusivity. The resulting equation is

$$N_{OH^-} = -P_{OH^-,A}\left(\frac{1}{\xi_{Zn}}\right)^2\left(c_{OH^-,B}-\frac{c_{OH^-,R}}{\kappa_{OH^-,S}}\right) \tag{146}$$

where $c_{OH^-,B}$ is the concentration of OH^- ions in the electrolyte surrounding the particles and is assumed to be equal to that in the separator layer. This assumption stems the assumption that there is minimal diffusional resistance in the electrode layer. The partition coefficient for OH^- with respect to the electrolyte is

$$\kappa_{OH^-,A} \equiv \left(\frac{c_{OH^-}}{c_{OH^-,B}} \right)_{eq} \tag{147}$$

For example, the portioning of OH^- ions from the electrolyte into the active material. The dimensionless, unreacted core radius is

$$\xi_{Zn} = R_{Zn} / R_{Zn,0} \tag{148}$$

where R_{Zn} is the instantaneous Zn particle radius and $R_{Zn,0}$ is the radius of a virgin Zn particle at time zero.

The permeability of hydroxyl ions is defined by

$$P_{OH^-,A} \equiv \frac{\kappa_{OH^-,S} D_{OH^-,A}(\xi_{Zn})}{R_{Zn,0}(1-\xi_{Zn})} \tag{149}$$

The permeability decreases with the state of the discharge as ξ reduces from 1 to 0. Under low discharge rates, there is typically high zinc utilization (complete conversion) and ξ will eventually be very close to zero. At high discharge rates, the range of variation of ξ would be more limited as the particles may not be fully discharged by virtue of having reached the limiting current prior to complete utilization.

Assuming that the reaction in the particle core is limited to the interface between the ash layer and the fresh core on the basis of unit surface area of core (denoted by r_ρ^*) and expressed as:

$$N_{i,R} = (\nu_{i\rho}) r_\rho^* \tag{150}$$

This equation is equated to the previous expression flux at the particle core. The flux through the electrode is Equation (150) multiplied by $(\xi_{Zn})^2 \gamma_M$. Further development will proceed after examination of the specifics in the electrode.

It is assumed that the anode kinetics are fast compared with solid-state diffusion. It is also assumed that the reaction in the particles of the active materials can be modeled as occurring in a distinct zone in each particle that defines the boundary between an inner core (unreacted zinc) and a shell with completely reacted material. Then from material balance on OH^- ions in the anode.

$$-\frac{1}{\overline{V}_{Zn,A}}\frac{dR_{Zn}}{dt}=\frac{(-\nu_{A,Zn})}{\nu_{A,e^-}}\left(\frac{R_{Zn,0}}{R_{Zn}}\right)^2\frac{i}{\gamma_{M,Zn}F} \tag{151}$$

Integrating

$$\xi_{Zn}^3=1-\frac{3}{R_{\alpha,0}}\left(\frac{-\nu_{A,Zn}}{\nu_{A,e^-}}\right)\frac{\overline{V}_{Zn,A}}{F\gamma_{M,A}}\int_0^t i dt \tag{152}$$

Further, defining Coulombic capacity

$$Q_t\equiv\int_0^t i dt \tag{153}$$

which for a discharge in the constant current discharge is simply $Q_t = i\,t$. Thus

$$\xi_{Zn}=\left[1-\frac{3}{R_{Zn,0}}\left(\frac{-\nu_{A,Zn}}{\nu_{A,e^-}}\right)\frac{\overline{V}_{Zn,A}}{F\gamma_{M,A}}Q_t\right]^{1/3} \tag{154}$$

This can be used for the determination of the dimensionless radius of the shrinking anode core for a certain discharged capacity Q_t. This in turn can provide the exchange current and the limiting current densities as a function of time or discharge capacity. Using these terms with the overall Butler-Volmer equation developed earlier finally gives V versus Q_t, or V versus t directly. The maximum Coulombic capacity, in C/cm^2, Equation (154) may be obtained from above for $\xi_{Zn} = 0$, and the use of Equation (153).

$$Q_{\max} = \left(\frac{\nu_{A,e^-}}{-\nu_{A,Zn}} \right) \left(\frac{m_{M,A}}{\rho_{M,A}} \right) \frac{F}{\overline{V}_{Zn,A}} \tag{155}$$

Alternatively we may write the discharge-dependent dimensionless radius as

$$\xi_{Zn} = \left(1 - \frac{Q_t}{Q_{\max}} \right)^{1/3} \tag{156}$$

In general, the capacity of one of the electrodes would be limiting. Since the oxygen source is essentially limitless (surrounding air), the anode is the limiting reaction in this particular cell.

The results derived above are based on unit area of the cathode structure. The conventional terms for evaluating battery capacity are typically per unit mass or per unit volume of the cell. For example, to convert the maximum Columbic capacity to the specific capacity (C/g):

$$C = \frac{Q_{\max}}{m_{cell}} \tag{157}$$

DIFFERENTIAL RESISTANCE

An ideal power source is defined as one whose potential is independent of the current drawn. Such a power source would not have any internal resistance that reduces the overall cell potential. The Zn/Air cell, and every power source in practice, is a non-ideal power source. Its potential is greatly affected by the current being drawn and the internal resistance losses that develop over time. These corresponding overpotentials were dealt with in the beginning of this chapter.

A useful tool for determining the potential-current relationships for an assembled cell is its differential resistance. Ohm's Law assumes linearity and thus is not appropriate for determining the resistances contributions of the terms shown in Figure III-1 since these potential-current relationships, aside from that for the separator, are non-linear. The differential resistance is thus defined as:

$$R \equiv \frac{\partial(\Delta\phi)}{\partial I} \tag{158}$$

Then defining the overall resistance, in $\Omega \cdot cm^2$, for the assembled Zn/Air cell:

$$R \equiv \frac{d(V_O - V)}{\partial i} \tag{159}$$

Then substituting Equation (143) into Equation (159):

$$R = -\frac{d\eta_C}{di} + \frac{d\eta_A}{di} + \frac{d\eta_{Sep}}{di} + \frac{d\eta_I}{di} \tag{160}$$

The differential resistance associated with the anode will be examined first, and the other cell components will follow. The contribution to the overall differential resistance of an assembled Zn/Air cell can be written as

$$R_A = \frac{d\eta_A}{di} = \frac{d}{di}\left[\frac{RT}{\bar{\alpha}_A F}\sinh^{-1}\left[\frac{1}{2}\left\{\frac{i_A}{i_{A,0}}\middle/1-\frac{i_A}{i_{A,L}}\right\}\right]\right] \tag{161}$$

To differentiate Equation (161), the following relation is used:

$$\sinh^{-1}(u) = \ln\left(u + \sqrt{1+u^2}\right) \tag{162}$$

The symbolic differentiation of Equation (162) is as follows:

$$\frac{d}{di}\left[\sinh^{-1}(u)\right] = \frac{d}{di}\left[\ln\left(u+\sqrt{1+u^2}\right)\right] = \frac{1}{u+\sqrt{1+u^2}}\left(1+\frac{1}{2}\frac{2u}{\sqrt{1+u^2}}\right)\frac{du}{di} = \frac{1}{\sqrt{1+u^2}}\frac{du}{di} \tag{163}$$

Where

$$\frac{du}{di} = \frac{d}{di}\left\{ \frac{i_A}{2i_{A,0}} \Big/ 1 - \frac{i_A}{i_{A,L}} \right\} = \frac{1}{2i_{A,0}} \frac{1}{1 - \frac{i_A}{i_{A,L}}} \tag{164}$$

The solution for Equation (161) is thus:

$$R_A = \frac{RT}{\left(2\vec{\alpha}_A F i_{A,0}\right)\left(1 - \frac{i_A}{i_{A,L}}\right)^2 \sqrt{1 + \frac{1}{4}\left(\frac{i_A}{i_{A,0}} \Big/ 1 - \frac{i_A}{i_{A,L}} \right)^2}} \tag{165}$$

The resistance associated with the cathode components is arrived in a similar fashion, i.e.,

$$R_C = \frac{d\eta_C}{di} = \frac{d}{di}\left[\frac{RT}{\vec{\alpha}_C F} \sinh^{-1}\left[\frac{1}{2}\left\{ \frac{i_C}{i_{C,0}} \Big/ 1 - \frac{i_C}{i_{C,L}} \right\} \right] \right] \tag{166}$$

Following the same manner of derivation described for the anode

$$R_C = \frac{RT}{\left(2\vec{\alpha}_C F i_{C,0}\right)\left(1 - \frac{i_C}{i_{C,L}}\right)^2 \sqrt{1 + \frac{1}{4}\left(\frac{i_C}{i_{C,0}} \Big/ 1 - \frac{i_C}{i_{C,L}} \right)^2}} \tag{167}$$

The resistance contributions from the separator and the interstitial resistances follow Ohm's law and thus take a linear term. The differentiation of these terms, respectively, is as follows:

$$R_{Sep} = \frac{d\eta_{Sep}}{di} = \frac{d}{di}\left[i\left(\frac{L_{Sep}}{\sigma_{KOH}} \right) \right] = \frac{L_{Sep}}{\sigma_{KOH}} \tag{168}$$

$$R_I = \frac{d\eta_I}{di} = \frac{d}{di}\left[iR_I \right] = R_I \tag{169}$$

The total differential resistance can thus be written as

$$R = -R_C + R_A + R_{Sep} + R_I \tag{170}$$

Using Equations (165), (167), (168), and (169) in Equation (170) yields:

$$\begin{aligned} R = & \frac{RT}{\left(2\vec{\alpha}_A F i_{A,0}\right)\left(1-\frac{i_A}{i_{A,L}}\right)^2\sqrt{1+\frac{1}{4}\left(\frac{i_A}{i_{A,0}}\Big/1-\frac{i_A}{i_{A,L}}\right)^2}} \\ & - \frac{RT}{\left(2\vec{\alpha}_C F i_{C,0}\right)\left(1-\frac{i_C}{i_{C,L}}\right)^2\sqrt{1+\frac{1}{4}\left(\frac{i_C}{i_{C,0}}\Big/1-\frac{i_C}{i_{C,L}}\right)^2}} \\ & + \frac{L_{Sep}}{\sigma_{KOH}} + R_I \end{aligned} \tag{171}$$

The differential resistance of a Zn/Air cell versus current density can now be plotted using the same parameters necessary for the development of a polarization curve for a given extent of discharge.

TIME-DEPENDENT ZINC PARTICLE PARAMETERS

For determination of the anodic discharge current density, the time-dependent parameters associated with the Zn particles and Zn mass are calculated as follows.

The volume of an individual Zn particle is:

$$V_{Zn,Part} = \frac{4}{3}\pi R_{Zn,O}^3 \tag{172}$$

The mass of an individual Zn particle is:

$$M_{Zn,Part} = V_{Zn,Part} \times \rho_{Zn} \tag{173}$$

The time-dependent surface area of a zinc particle is equal to:

$$A_{Zn,Part,t} = 4\pi R^2 \tag{174}$$

The total number of Zn particles:

$$N_{Zn,Part} = \frac{M_{Zn}}{M_{Zn,Part}} \tag{175}$$

Time-dependent surface area of total Zn particles:

$$A_{Zn,Part,Total,t} = A_{Zn,Part,t} \times N_{Zn,Part} \tag{176}$$

Time-dependent anodic discharge current density:

$$i_{discharge,a} = \frac{i_{discharge}}{A_{Zn,Part,Total,t}} \tag{177}$$

THEORETICAL CAPACITY AND SERVICE LIFE

To aid in the evaluation of the developed predictive model, it is useful to examine the theoretical capacity and service life under prescribed discharge conditions. The overall cell reaction, Reaction (29), is utilized as the basis to complete these calculations:

$$2Zn + O_2 \rightarrow 2ZnO \tag{29}$$

The electrochemical equivalents for the reactants of this equation are[1]:

Zn	0.82 Ah/g
O_2	3.35 Ah/g

Assuming that the supply of O_2 is limitless since its source is the surrounding environment then the theoretical capacity is solely determined by the amount of Zn present in the cell, providing that there are no kinetic, transport, or Ohmic limitations. The theoretical capacity of the Size 13 cell is then calculated by:

$$C = 0.3477g \times 0.82\frac{Ah}{g} = 0.285Ah = 285mAh \tag{178}$$

With the theoretical capacity determined, it is now possible to calculate the theoretical service life based upon the various discharge currents to be examined in the predictive model. The theoretical service hours are as follows:

For 1mA discharge current: $$t_{1mA} = \frac{285mAh}{1mA} = 285h \quad (179)$$

For 4mA discharge current: $$t_{4mA} = \frac{285mAh}{4mA} = 71.3h \quad (180)$$

For 10mA discharge current: $$t_{10mA} = \frac{285mAh}{10mA} = 28.5h \quad (181)$$

Again, these calculations are solely theoretical and based upon complete utilization of the mass of anode reactant, Zn. As seen throughout the course of model development, there are many limiting factors that cause a reduction in cell performance and service life. However, these values will aid in the evaluation of the values predicted by the developed model. A comparison of the theoretical capacities in conjunction with the predicted and experimentally determined values will allow for determination of Zn utilization and overall reaction efficiency under various discharge conditions.

MODEL PARAMETERS

To complete the model simulations, three parameters were fitted, including the diffusion coefficient of hydroxyl ions in the ash layer, the anodic exchange current density, and the cathodic exchange current density. The values chosen were determined to be reasonable based upon comparisons of similar terms defined in Mao et al. and Kinoshita.[40,3]

The pore size of the structure was assumed. However, the value selected is in-line with observations made during various fuel cell studies.[39] Due to the similarity of

assembly between the fuel cell and the Zn/Air cell, this assumption is valid. The gas diffusion coefficients within the porous structure are calculated parameters based upon the DFM and are incorporated within the model. Please refer to the Appendix for more information in regards to gas diffusion coefficient determination.

Table III-1 includes the values used during the simulation of polarization, discharge performance, and time-dependent anodic limiting current density. The table is divided into five distinct parameter categories: Cell Structure, Reaction Kinetic, Transport, Input, and Universal Constants. For each value, a reference is given. For those that were taken from the literature, the corresponding number relates to the reference referred to within the References section of this thesis. For those values which are fixed due to their association either with a cell design or component dimension, the term "Given" is assigned since these are fixed values. For parameters that were fitted, the term "Fitted" is listed as the reference. Values that were assumed are noted as such. The remaining parameters that are calculated are also noted as such.

Table III-1: Parameters employed during polarization, discharge, and differential resistance simulations for a Size 13 Zn/Air cell.

CELL PARAMETERS			
INPUTS	**VALUE**	**UNITS**	**REFERENCE**
Mass of Zinc	0.3477	g	Given
Cathode Geometric Area	0.438	cm^2	Given
Anode Compartment Volume	0.1578	cm^3	Given
ρ_{Zn}	7.14	g/cm^3	Given
L_{SEP}	0.010	cm	Given
L_A	0.3233	cm	Given
L_C	3.556×10^{-2}	cm	Given
$R_{Zn,o}$	0.0125	cm	Given
$\overline{V}_{Zn}$	9.18	cm^3/mol	Given
pore size	1.065×10^{-4}	cm	Assumed
$R_{A,0}$	1.25×10^{-2}	cm	Given
$R_{C,0}$	1.51×10^{-7}	cm	Given
Volume fraction of Zinc	0.3436	Dimensionless	Calculated
Volume fraction of Carbon	0.1765	Dimensionless	Calculated
Zinc Loading	0.7938	g Zn/cm^2	Calculated
Carbon Loading	0.0113	g C/cm^2	Calculated
REACTION KINETIC PARAMETERS			
INPUTS	**VALUE**	**UNITS**	**REFERENCE**
$i_{A,0}$	1.0×10^{-4}	A/cm^2	Fitted
$i_{C,0}$	1.0×10^{-11}	A/cm^2	Fitted
$\kappa_{OH^-,A}$	1	Dimensionless	Assumed
TRANSPORT PARAMETERS			
INPUTS	**VALUE**	**UNITS**	**REFERENCE**
α_A	0.5	Dimensionless	Assumed
α_C	0.5	Dimensionless	Assumed
$D^e_{OH^-,A}$	0.51×10^{-8}	cm^2/sec	Fitted
σ_{KOH}	0.45	S/cm	40
t_{OH^-}	0.78	dimensionless	40
c_{OH^-}	8.0×10^{-3}	mol/ cm^3	40
OPERATING PARAMETERS			
INPUTS	**VALUE**	**UNITS**	**REFERENCE**
Discharge Current	1 4 10	mA mA mA	Given

V_o	1.654	V	Calculated
T	293	K	Given
iR_I	0	V	Assumed
UNIVERSAL CONSTANTS			
INPUTS	**VALUE**	**UNITS**	**REFERENCE**
R	8.314	J/mol·K	59
F	96,485	C/mol	59
$MW\ O_2$	32	g/mol	59
$MW\ H_2O$	18	g/mol	59
$MW\ N_2$	28	g/mol	59

CHAPTER IV
EXPERIMENTAL

Numerous techniques were employed during the development of experimental data in support of the proposed model and its subsequent validation. To investigate the structure of various components, the cells were cross-sectioned, polished, and then examined via digital light microscopy and Scanning Electron Microscopy (SEM). In some instances, Energy-Dispersive Spectroscopy (EDS) was utilized to complete elemental analyses of the prepared samples. To characterize cell discharge performance and provide validating data for the predictive model, a Maccor Series 4000 battery testing cabinet was utilized for the testing of various Size 13 Zn/Air. Examination of the morphology and ZnO distribution, post-discharge, was completed by cross-sectioning the discharged cells and invoking a novel extraction/polishing technique slightly modified to that proposed by Horn et.al.[4] Digital images of the cross-sections that were generated were then taken using an Olympus SZ-CTV with a Sony CCD-IRIS video camera attached. The various techniques employed are discussed in this chapter.

SIZE 13 ZN/AIR CELLS

As mentioned previously, Size 13 Zn/Air cells were employed during the course of this study. These cells were discharged under the various conditions and were the basis for the structural investigations that are to be discussed. The overall performance of these cells vary between manufacturers. The rated cell capacities vary between manufacturers, but typically range from 260 to 300 mAh. In addition, the various cell dimensions vary between manufacturers. The overall cell height and overall cell diameter of Size 13 button cells are specified to range in height from 5.0 to 5.4 mm and 7.5 to 7.9

mm in diameter by the International Electrochemical Commission (IEC). The American National Standards Institute (ANSI) also has similar specifications. Both governing bodies also set performance and abuse testing requirements for Zn/Air electrochemical cells for various manners of discharge and storage. Figure IV-1 is a profile view of a characteristic Size 13 cell.

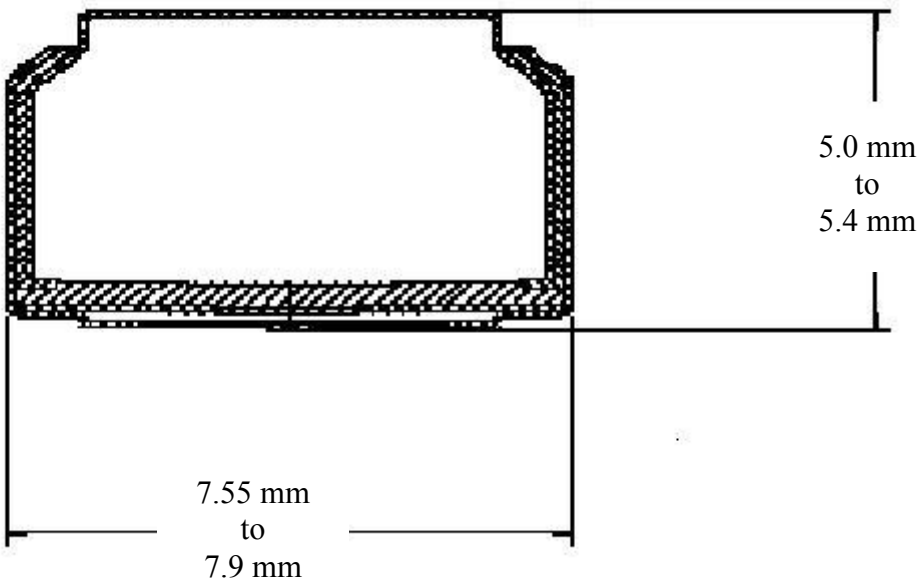

Figure IV-1: Profile of characteristic Size 13 Zn/Air cell employed during the course of this thesis.

COMPONENT STRUCTURE INVESTIGATIONS

The cells to be examined were cross-sectioned by mounting cells or cell components in a low-viscosity epoxy resin, such as Struers Epo-fix resin. To prepare the mounts, a forming cup was filled with resin and the sample cell was placed in. The mixture was stirred slightly, allowing any entrained air bubbles to escape. The forming cup incorporating the epoxy mix and sample cell was then placed under vacuum for approximately 24 hrs to allow the release of any additional air bubbles. There upon, the forming cup was then allowed to set for a period of 24 hrs to allow the epoxy to harden. This overall procedure of preparing a mount has been commonly termed “potting” and the mounted sample cell or component is said to be "potted".

With the mounts complete, the samples were then ready for cross-sectioning. The procedures are slightly different for the sample being analyzed. The procedures for component and non-discharged cell preparation are discussed below. Please see Figures IV-2 and IV-3 for examples of a finished mount of a Size 13 cell that has been polished.

Procedure - Component Mount Preparation

1. The mount was cut longitudinally at a location slightly less than half the samples’ outer diameter or width using a 600 grit silicon carbide grinding wheel. During the cutting process, water was used both as a slight lubricant and a cooling aid.
2. Three successive polishing steps, accompanied by a lubricant such as mineral oil, were then completed.

2.1. The first polishing step incorporated a 6 micron diamond polishing pad at a rotation of approximately 80 rpm followed by an isopropanol ultrasonic cleaning.

2.2. The second polishing step incorporated a 3 micron diamond polishing pad at a rotation of approximately 100 rpm followed by an isopropanol ultrasonic cleaning.

2.3. The final polishing step incorporated a 1 micron diamond polishing pad at a rotation of approximately 120 rpm followed by an isopropanol ultrasonic cleaning.

3. In some instances, a final etching step that utilized an etchant such as sulfuric acid was incorporated after the completion of the polishing steps. The exposed sample side of the polished mount was placed in an etchant dip for a period of no more than 30 seconds. This enabled an oxide-free examination surface, which lead to clear digital images.

Procedure - Non-Discharged Cell Mount Preparation

1. The mount was cut longitudinally at a location slightly less than one quarter of the cells' outer diameter using a 600 grit silicon carbide grinding wheel. During the cutting process, water is used both as a slight lubricant and a cooling aid.
2. The anolyte was then removed via flushing with running water and the open anode cavity was backfilled with epoxy under vacuum.
3. After the backfilled epoxy hardened, three successive polishing steps, accompanied by a lubricant such as mineral oil, are then completed.

3.1 The first polishing step incorporated a 6 micron diamond polishing pad at a rotation of approximately 80 rpm followed by an isopropanol ultrasonic cleaning.

3.2 The second polishing step incorporated a 3 micron diamond polishing pad at a rotation of approximately 100 rpm followed by an isopropanol ultrasonic cleaning.

3.3 The final polishing step incorporated a 1 micron diamond polishing pad at a rotation of approximately 120 rpm followed by an isopropanol ultrasonic cleaning.

4. In some instances, a final etching step that utilizes an etchant such as sulfuric acid was incorporated after the completion of the polishing steps. To complete this, the exposed sample side of the polished mount was placed in an etchant dip for a period of no more than 30 seconds. This enabled an oxide-free examination surface, which provided clear digital images.

Figure IV-2: Side view of a cross-sectioned and polished Size 13 mount.

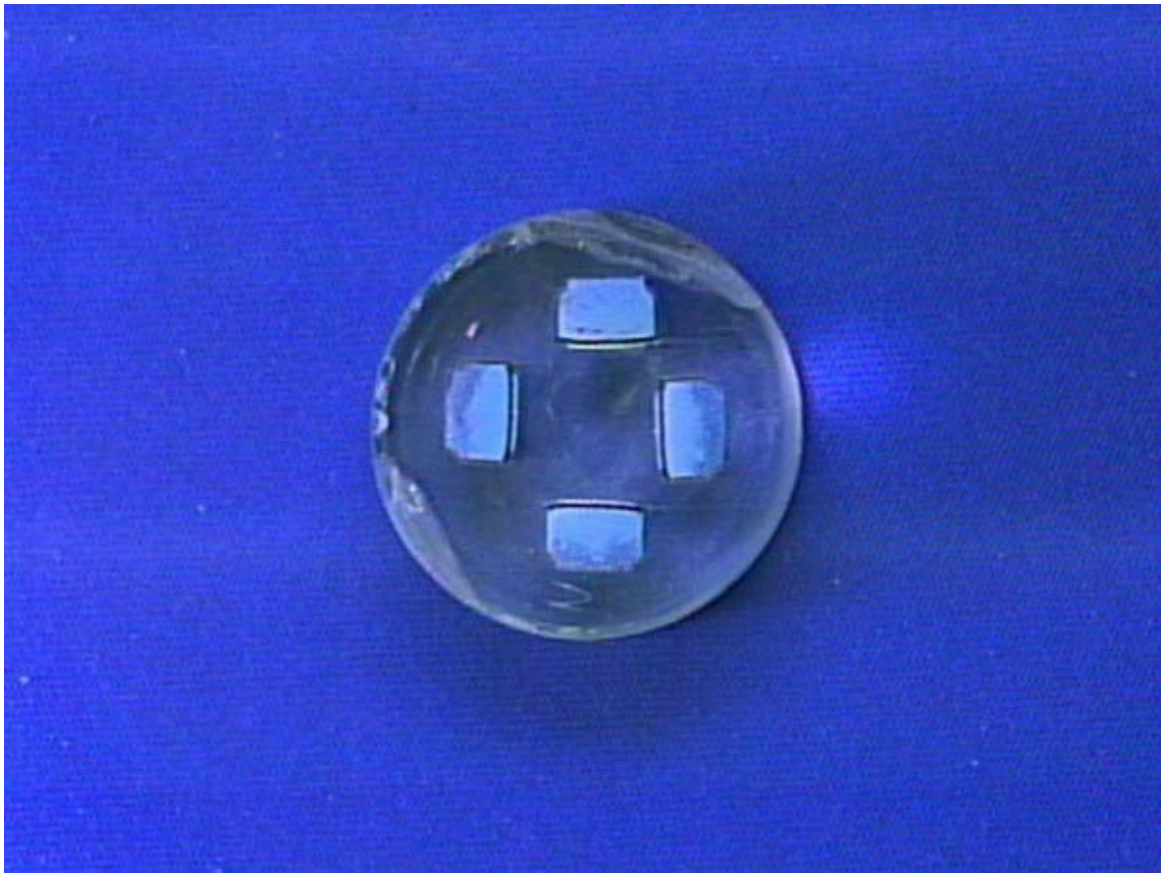

Figure IV-3: Top view of a cross-sectioned and polished Size 13 mount.

DIGITAL IMAGE COLLECTION

After the cell mount preparation was completed, digital images were acquired via two methods: digital light microscopy or a Scanning Electron Microscopy (SEM). The digital camera utilized was an Olympus SZ-CTV. The camera has a Sony CCD-IRIS video camera attached to it. This attachment facilitated the direct capture of digital images to a personal computer. The assembly has a magnification range of X to Y and was utilized for the capturing of relatively high magnification images (Figures V-16, V-17, and V-18). For lower magnification images, a JVC TK=1270 video camera was utilized (Figures IV-1 and IV-2).

For the generation of images via SEM, an Amray Model 1830 SEM with computer SEM control was used. In addition, the system has an attached KEVEX EDS system for the completion of Electron Dispersive Spectroscopy analyses. The SEM system parameters for image collection were an accelerating voltage of 20 kV and a working distance of 12 mm. To enable the use of SEM examination for materials that are non-conductive, the mounts were coated with a gold layer of 5 to 10 μm thickness to prevent charging of the sample, which will otherwise produce thick black spots on the images and prevent clear observations of general characteristics. The sputtering of gold was completed using a EMITECH Model 550 Gold Sputter Coater. For samples in which EDS analysis was to be completed, the mounts were coated with a carbon layer of approximately 5 μm thickness instead since the presence of gold would impact the EDS analysis due to the possibility of overlapping with peaks of interest. When carbon sputtering was done, it was completed using a EMITECH Model 950 Carbon Evaporator.

CELL DISCHARGE TESTING

For the generation of discharge curves, Size 13 Zn/Air cells were discharged at rates of 1mA, 4mA, and 10mA respectively on a Maccor Series 4000 battery testing cabinet. These discharge rates are equal to 2.789mA/g, 11.158mA/g, and 27.894mA/g of zinc. A total of 16 cells were discharged for each group completed.

The Maccor Series 4000 battery testing cabinet is specifically designed for the testing of primary and secondary batteries (or cells). The systems are multi-channel, computerized, and capable of complete automation. The system can support discharge currents up to 5A and discharge voltages up to 12V. There are 128 channels available for discharge testing. Each channel operates under common specifications. There are a total of four current ranges that each channel is capable of: Range 1 is 150μA, Range 2 is 5mA, Range 3 is 150mA, and Range 4 is 5A. Current was measured, recorded, and controlled to 0.02% of the full current scale for each channel. Voltage was measured, recorded, and controlled to 0.02% of full voltage span for each channel. Step times could also be programmed in 10 millisecond increments with a minimum step length of 10milliseconds. Capacity (amp hours) was measured, recorded, and used for control to the same accuracy as current and voltage measurements. Battery (or cell) parameters were measured 100 times per second and used for control. Performance data was collected at operator defined intervals and was available with 10 millisecond time resolutions. Data points were automatically reported at the beginning and end of each step. Each channel could be programmed, started, and operated independently of all other channels. Failure, whether short or open, of the battery (or cell) being cycled on any channel did not affect cycling of any other channel.

ZINC DISCHARGE AND SPATIAL DISTRIBUTION ANALYSIS

To evaluate the physical properties of the discharged Zn in a cell, the discharged cells were mounted in epoxy in the same manner previously discussed After mounting, the cells were cross-sectioned via a different method of post-mount treatments to prevent the self-discharge of non-reacted Zn. This methodology is described in detail below and follows the procedure proposed by Horn et al., with minor variations.[4]

Procedure - Discharged Cell Mount Preparation

1. The mount was cut longitudinally at a location slightly less than half the samples' outer diameter using a 600 grit silicon carbide grinding wheel. During the cutting process, methanol used both as a slight lubricant and a cooling aid.
2. After the first cross-sectioning step, the mount was placed sample side down in a volume of acetone that covers approximately 50% of the mount height in the container used (i.e., 12.5 mL of acetone in a 30 mL vial) to allow the extraction of water in the cell. The mount was allowed to soak in this arrangement for a period of 16 hours. It was observed that allowing the mount to soak for a longer duration softened the epoxy and caused issues with the remaining preparation steps.
3. Next, the mount placed in a vial in the same manner as Step 2 and was allowed to soak in methanol for a period of four days to allow potassium hydroxide extraction. The sample was periodically agitated throughout the four day duration.
4. The mount was then placed in an oxygen free environment, under vacuum, and allowed to evaporate for a period of 24 hrs.

5. The mount was then backfilled with additional epoxy under vacuum.
6. The mount was then longitudinally cross-sectioned as per Step 1 to allow examination of the sample surface below the atmosphere-exposed layer during the acetone-methanol treatment steps.
7. Three successive polishing steps were then completed. To prevent additional self-discharge, the polishing steps were completed with water-free lubrication media (isopropanol). During all polishing steps, care must be taken so as not to impregnate the Zn/ZnO surface with Silicon Carbide (SiC).
    7.1. The first polishing step incorporated a 6 micron diamond polishing pad at a rotation of approximately 80 rpm followed by an isopropanol ultrasonic cleaning.
    7.1.1. The second polishing step incorporated a 3 micron diamond polishing pad at a rotation of approximately 100 rpm followed by an isopropanol ultrasonic cleaning.
    7.2. The final polishing step incorporated a 1 micron diamond polishing pad at a rotation of approximately 120 rpm followed by an isopropanol ultrasonic cleaning..
8. The preparation of the mounts was now complete and detailed examinations could be undertaken.

As previously mentioned, the extraction of the water prevents the direct oxidation of unreacted Zn. To avoid this process from happening during the preparation of the sample mounts, water-free polishing steps were followed. The extraction of the potassium hydroxide prevented the direct conversion of potassium hydroxide to

potassium carbonate. As previously discussed, potassium carbonate is a solid, white powder. The images captured from cells with such powder distributed through the anode compartment would not be clear and would not allow the accurate description of the Zn discharge front or the spatial distribution of unreacted Zn particles. Following these steps enables the capturing of clear images (via both digital light microscopy and SEM) of discharged versus non-discharged Zn as well as the Zn discharge front.

CHAPTER V
RESULTS AND DISCUSSION

During the course of this investigation, a substantial amount of information was generated. For instance, polarization and discharge performance of Size 13 Zn/Air cells was carefully investigated. In addition, experimental data was collected pertaining to physical properties of various cell components as well as pre and post-discharge behavior observations. This information was key in understanding the cell functionally and in supporting the theoretical foundations employed during the mathematical development of the one-dimensional performance model. The results generated from these investigations and their overall pertinence to the validity of the performance prediction model are discussed in this chapter.

MODEL-BASED POLARIZATION CURVE

Modeling work presented in this thesis allows the determination of polarization behavior for a Zn/Air cell under various states of discharge. The polarization curve is a plot of voltage versus current density. Utilizing the current density allows for behavioral investigations that are not dependent on either cell size or discharge current. The differing variations of cell size typically are associated with varying cathode surface area. Simply multiplying the current density by the cathode area in question would give predicted voltage values as a function of discharge current, and vice versa.

Figures V-1 and V-2 are model-based polarization curves for the assembled cell for 25% and 50% discharge capacity respectively. Based upon the cathode surface area for this cell size, the limiting currents are predicted to be roughly 15mA for 25% discharge capacity and 2mA 50% discharge capacity respectively. These curves also

illustrate the time-dependent effects of discharge that occur within a cell at various states of discharge. As the cell continues to discharge, passive films and transport resistances are developing. These phenomena have negative effects on the overall cell performance, as is illustrated via that dynamic change of the calculated limiting current.

Experimental discharge curves were not developed in the course of this study. Future evaluations could include the comparison of the model-based polarization curves versus polarization curves derived from experimental results. Insight into the optimization of cell design parameters could be gained by such an evaluation.

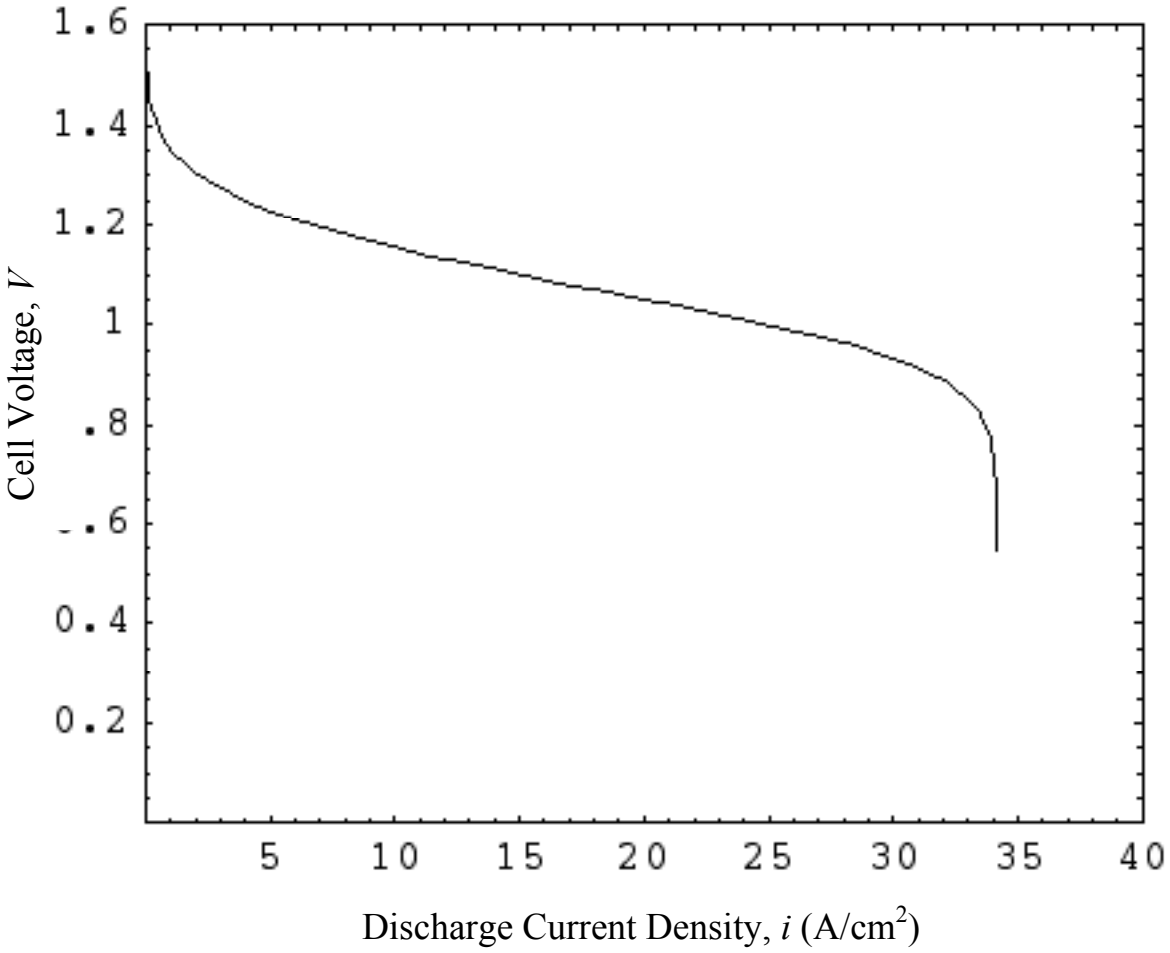

Figure V-1: Model-based polarization curve for Size 13 Zn/Air cell at 25% discharge capacity.

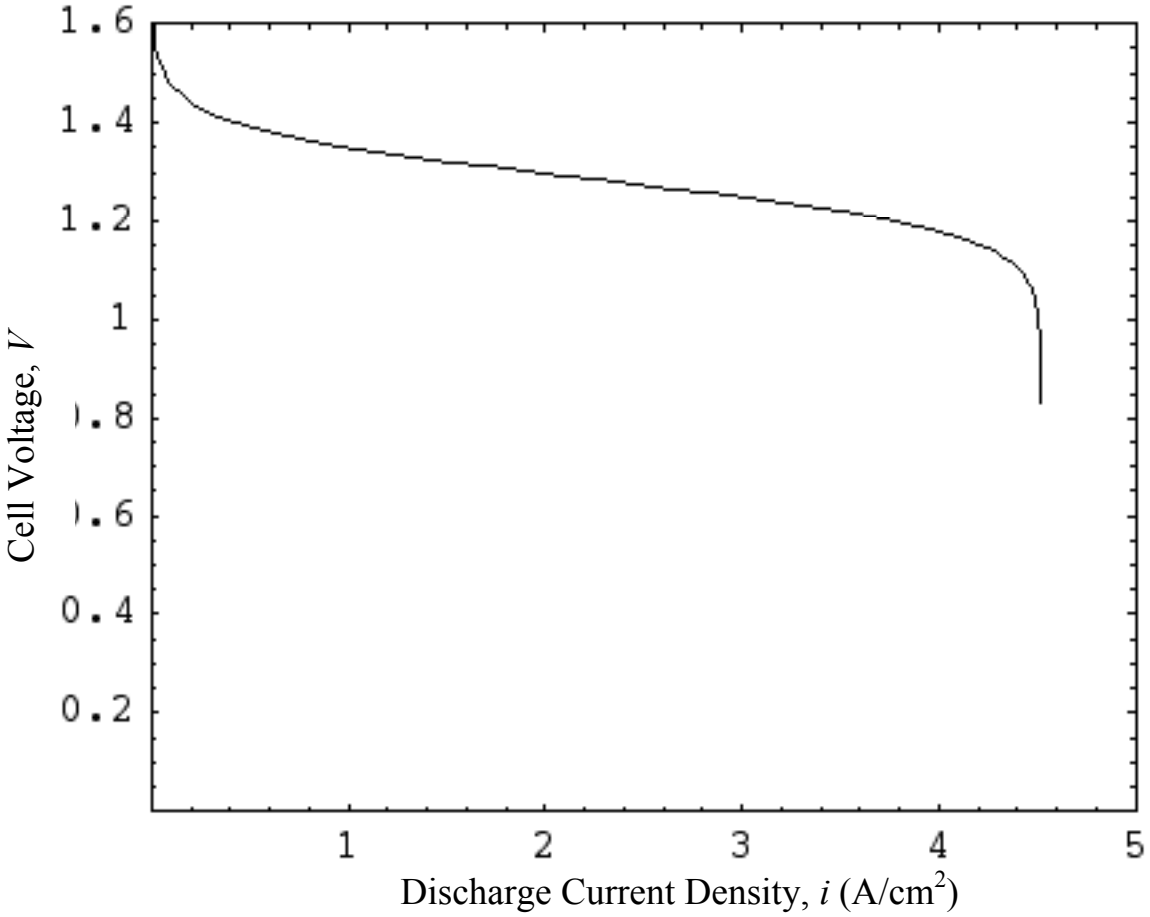

Figure V-2: Model-based polarization curve for Size 13 Zn/Air cell at 50% discharge capacity.

MODEL-BASED DISCHARGE CURVES AND ANALYSES

In this section, the model-based discharge curves and additional model-based cell characteristics are discussed. Each discharge drain (1mA, 4mA, and 10mA) will be examined individually. Various insights can be gained by examining the cell performance first from a theoretical standpoint. In subsequent sections, the theoretical results are compared with experimental results to obtain useful insights into cell.

1mA Continuous Discharge

The model-based discharge curve for 1mA continuous current is presented in Figure V-3. It is observed that the cell voltage is running relatively steady (or flat) until near the end of service life where there is a precipitous decline in cell voltage. The predicted performance of this cell, based upon 0.3477g of Zn and a gravimetric energy density of 0.82Ah/g, is 285mAh. For a discharge rate of 1mA continuous, the theoretical runtime is 285 service hours. The predicted service-life generated from the model for 1mA continuous drain is 284.21 service hours, which is within 0.5% of the theoretical value.

4mA Continuous Discharge

The model-based discharge curve for 4mA continuous current drain is presented in Figure V-5. The running voltage is predicted to be lower for this discharge, but relatively steady until the end of service life. The theoretical runtime for this discharge rate is 71.3 service hours. The predicted service-life generated from the model for 4mA continuous drain is 67.945, which is within 5% of the theoretical value.

10mA Continuous Discharge

The model-based discharge curve for 10mA continuous current drain presented in Figure V-9. The predicted running voltage has shifted even lower than the previous simulations. In addition, the discharge slope is relatively steeper than those generated for the 1mA and 4mA discharge rates. The theoretical runtime for this discharge rate is 28.5 service hours. The predicted service-life generated from the model for 10mA continuous drain is 22.85, which is within 20% of the theoretical value.

Simulation Observations

It was determined that the primary factor affecting the predicted service life was the diffusion coefficient of OH^- in the ash layer. Adjusting this parameter had significant effect in both the reduction and increase of the predicted service life value. This parameter also has significant impact on the overall shape of the curve at the end of service. The adjustment of this parameter can lead to a radius in the knee of the curve that is either very sharp or gradual.

The exchange current densities had significant impact on the running voltage and overall flatness of the discharge curve. The cathodic exchange current density was determined to be of most significance to the running voltage. Minor adjustments of this parameter could cause significant swings in the running voltage value. The anodic exchange current density had some impact on running voltage, but primarily effected the overall flatness of the discharge curve. When high values were selected for this parameter, the discharge curve was very square. Proper adjustment lead to an overall

relatively flat discharge curve with an increasingly slight slope with increasing discharge current.

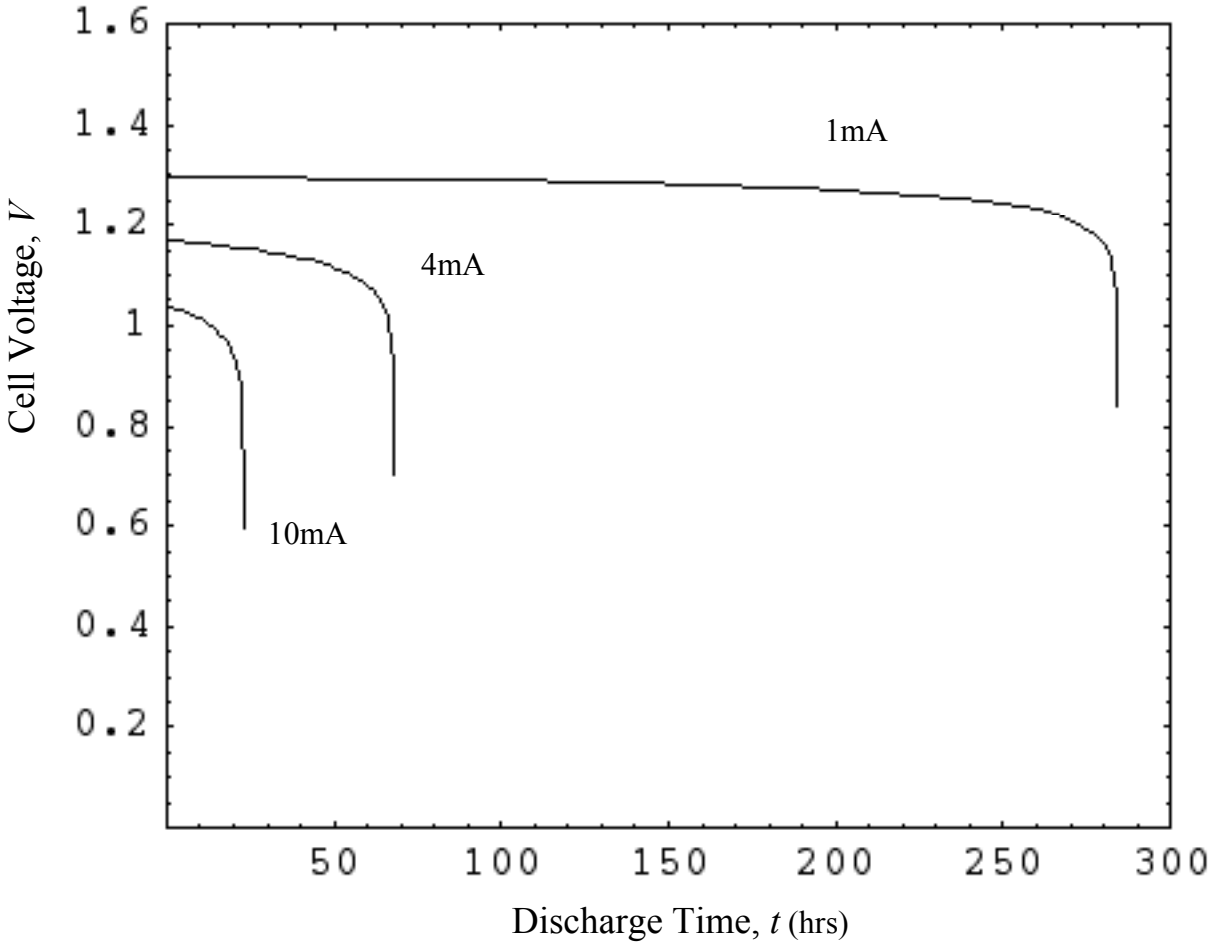

Figure V-3: Model-Based discharge curves for Size 13 Zn/Air cell at 1mA, 4mA, and 10mA continuous current discharge.

COMPARISON WITH EXPERIMENTAL DATA

Figures V-13 through V-15 overlay the predicted, model-based performance curves over those obtained experimentally at the discharge currents of 1mA, 4mA, and 10mA respectively.

1mA Continuous Discharge

The comparison of the model-based versus the experimental discharge curves for 1mA continuous current is presented in Figure V-3. The model-based curve is represented by the solid line. The experimental discharge curve is represented by the dashed line. The experimental discharge curve is the average of 16 Size 13 cells that were discharged at 1mA continuous current. During the collection of the discharge results, there were some issues with the collection of data. This are the points that deviate from the overall running voltage of approximately 1.25V during discharge. The average service life for these cells was 282.84 service hours. The predicted service-life generated from the model for 1mA continuous drain is 284.21 service hours, which is within 0.5% of the experimental value. Overall the model shows excellent agreement with the experimental discharge curve. The discharge slopes are close to one another, as are the service life values.

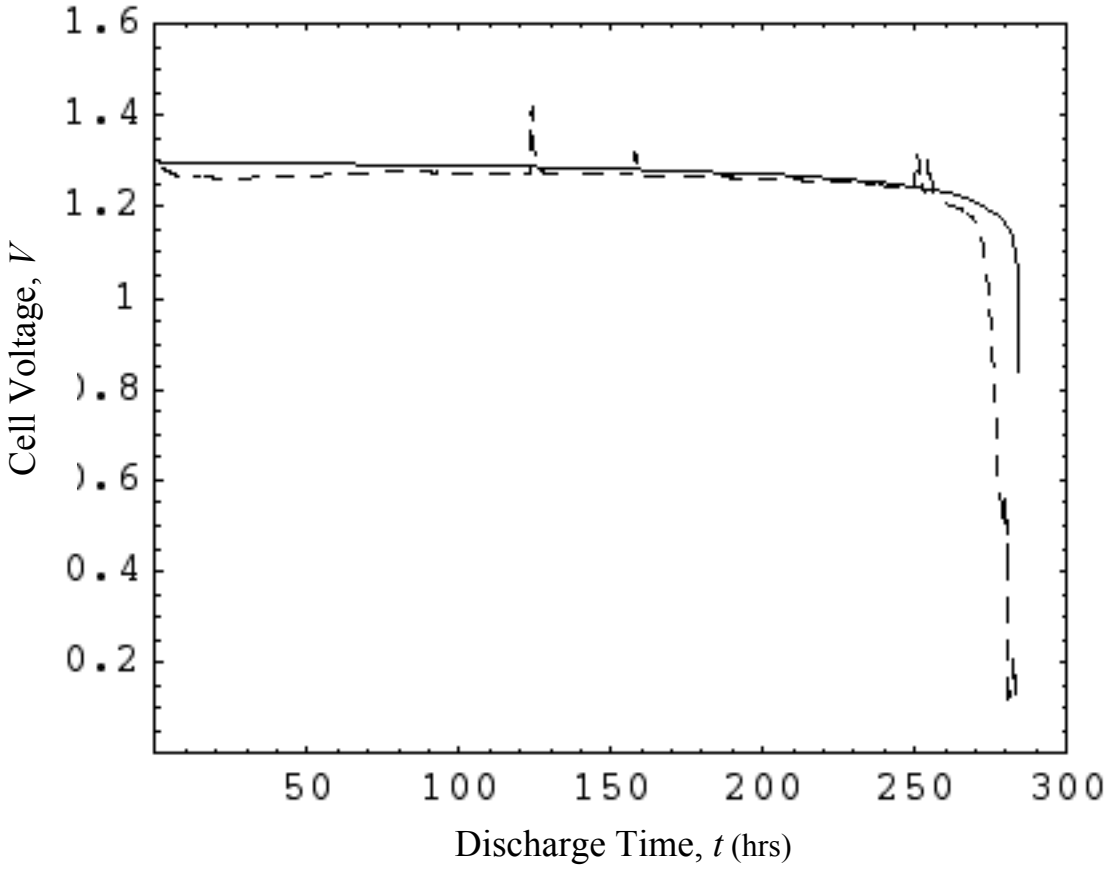

Figure V-4: Experimental versus Model-Based discharge curves for Size 13 Zn/Air cell at 1mA continuous current drain.

4mA Continuous Discharge

The comparison of the model-based versus the experimental discharge curves for 1mA continuous current is presented in Figure V-3. The model-based curve is represented by the solid line. The experimental discharge curve is represented by the dashed line. The experimental discharge curve is the average of 16 Size 13 cells that were discharged at 4mA continuous current. The average service life for these cells was 67.9541 service hours. The predicted service-life generated from the model for 1mA continuous drain is 67.945 service hours, which is within 0.5% of the experimental value. At this elevated discharge rate, the model shows excellent agreement with the service life and discharge slope of the experimental discharge curve.

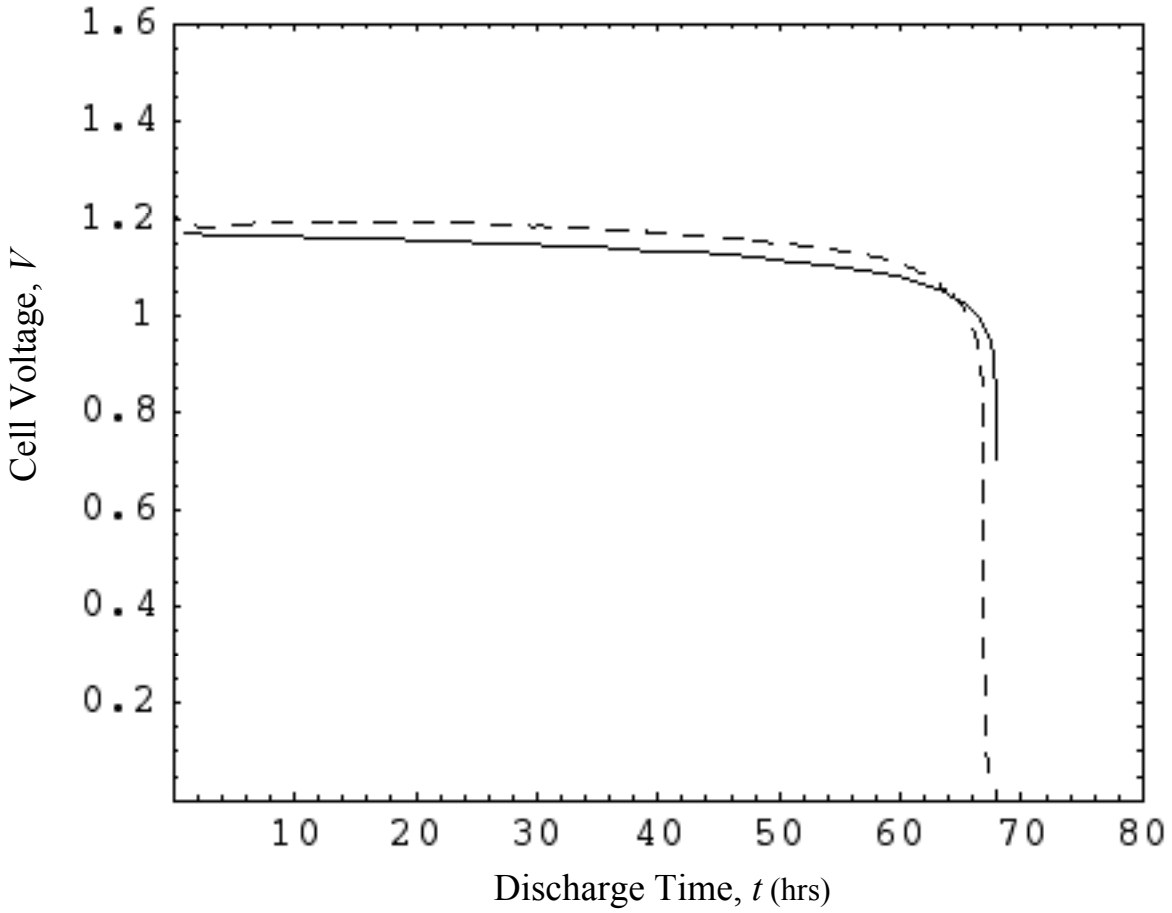

Figure V-5: Experimental versus Model-Based Discharge curves for Size 13 Zn/Air cell discharged at 4mA continuous current drain.

10mA Continuous Discharge

The comparison of the model-based versus the experimental discharge curves for 10mA continuous current is presented in Figure V-3. The model-based curve is represented by the solid line. The experimental discharge curve is represented by the dashed line. The experimental discharge curve is the average of 16 Size 13 cells that were discharged at 4mA continuous current. The average service life for these cells was 22.6925 service hours. The predicted service-life generated from the model for 1mA continuous drain is 22.85 service hours, which is within 0.5% of the experimental value. The predicted service life values for the model show excellent agreement with the experimental service life. At this high discharge rate deviations in discharge slope exist. The experimental values show a much steeper slope than that of the predicted. This is most likely due to deviations in the time-dependent anodic exchange current density, which is a function of the dimensionless Zn radius. It is possible that the modeling approach employed does not account for the porosity reduction behavior at this discharge rate sufficiently and thus the deviation arises.

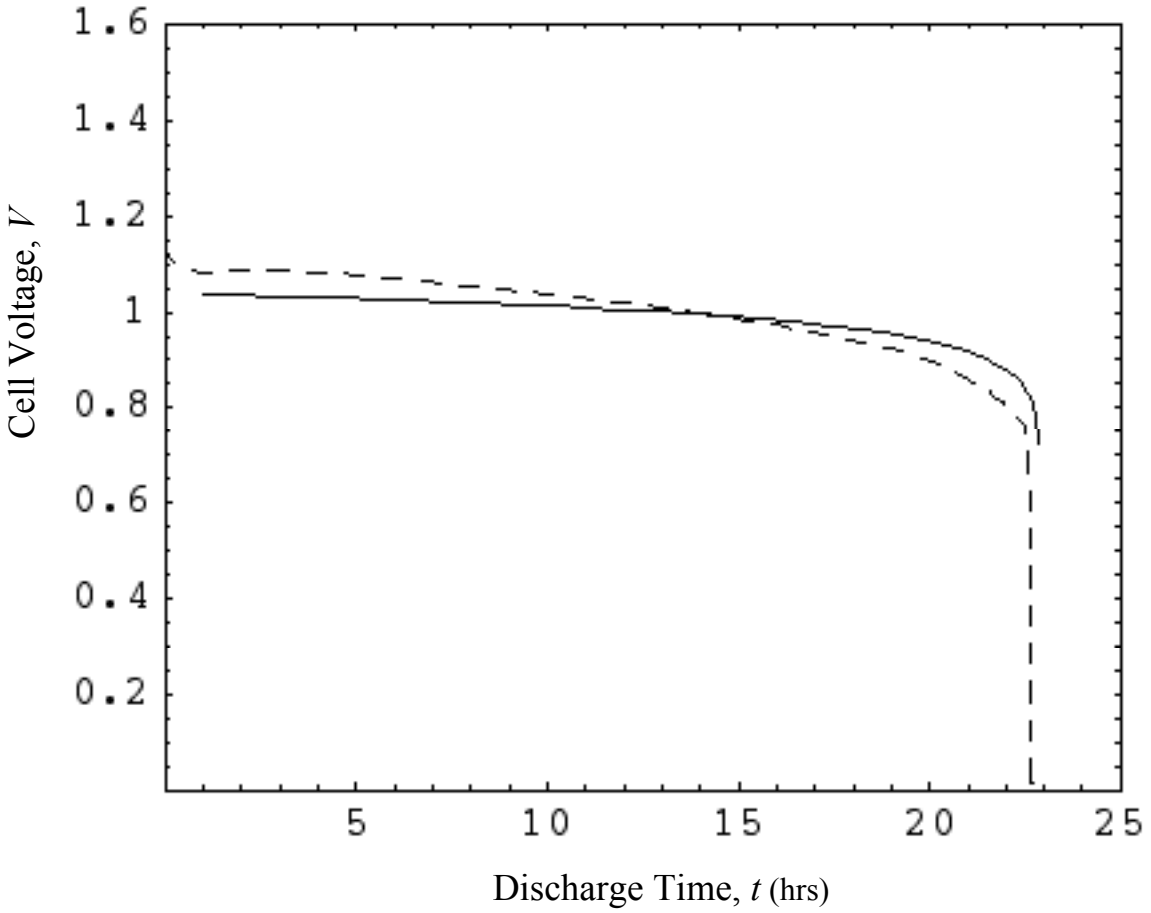

Figure V-6: Experimental versus Model-Based Discharge curves for Size 13 Zn/Air cell discharged at 10mA continuous current drain.

MODEL-BASED ANODIC LIMITING CURRENT DENSITY

Examination of the effects of discharge rate on the model-based anodic limiting current density can give additional insight into the performance characteristics of a Zn/Air cell. Figures V-7, V-8 and V-9 are plots of the time-dependent, model-based anodic limiting current density versus time.

The predicted service life is over when the limiting current is equal to the discharge current according to the theoretical basis of the model and the developed kinetic equations. It is at this point that the anodic overpotential becomes very high due to zero value in the denominator of the hyperbolic sine term of Equation (130).

By setting the limiting current density equal to the discharge current density enables the determination of a calculated value for the ash layer permeability, which in turn can lead to the calculation of the Zn utilization.

Based upon the discussion within this section, there are some deviations that exist between the calculated observations and the expected results. From the figures, the predicted limiting current is lower than the discharge current. The error associated with this observation is most likely based within the Zn reaction assumptions.

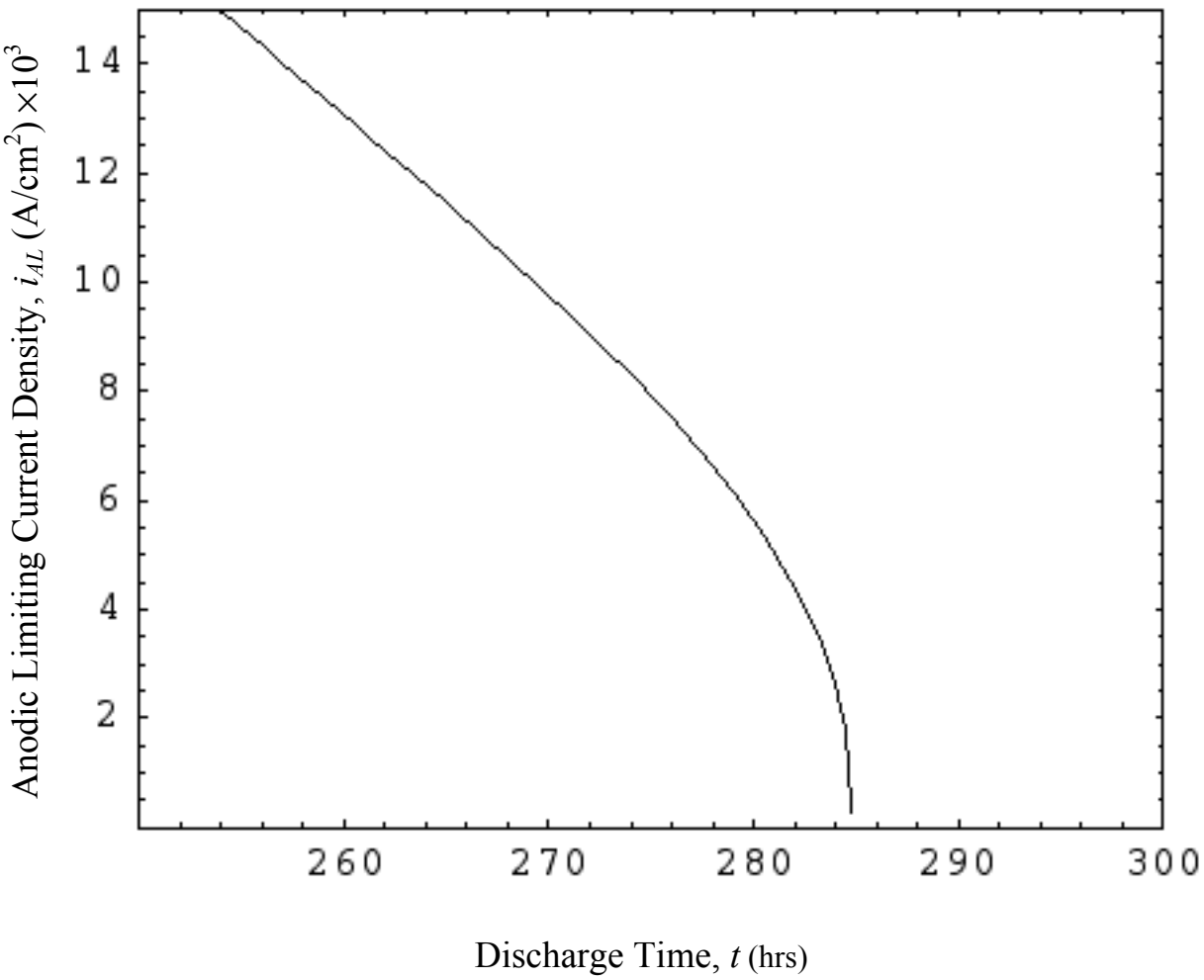

Figure V-7: Anodic limiting current density versus time for Size 13 Zn/Air cell at 1mA continuous discharge.

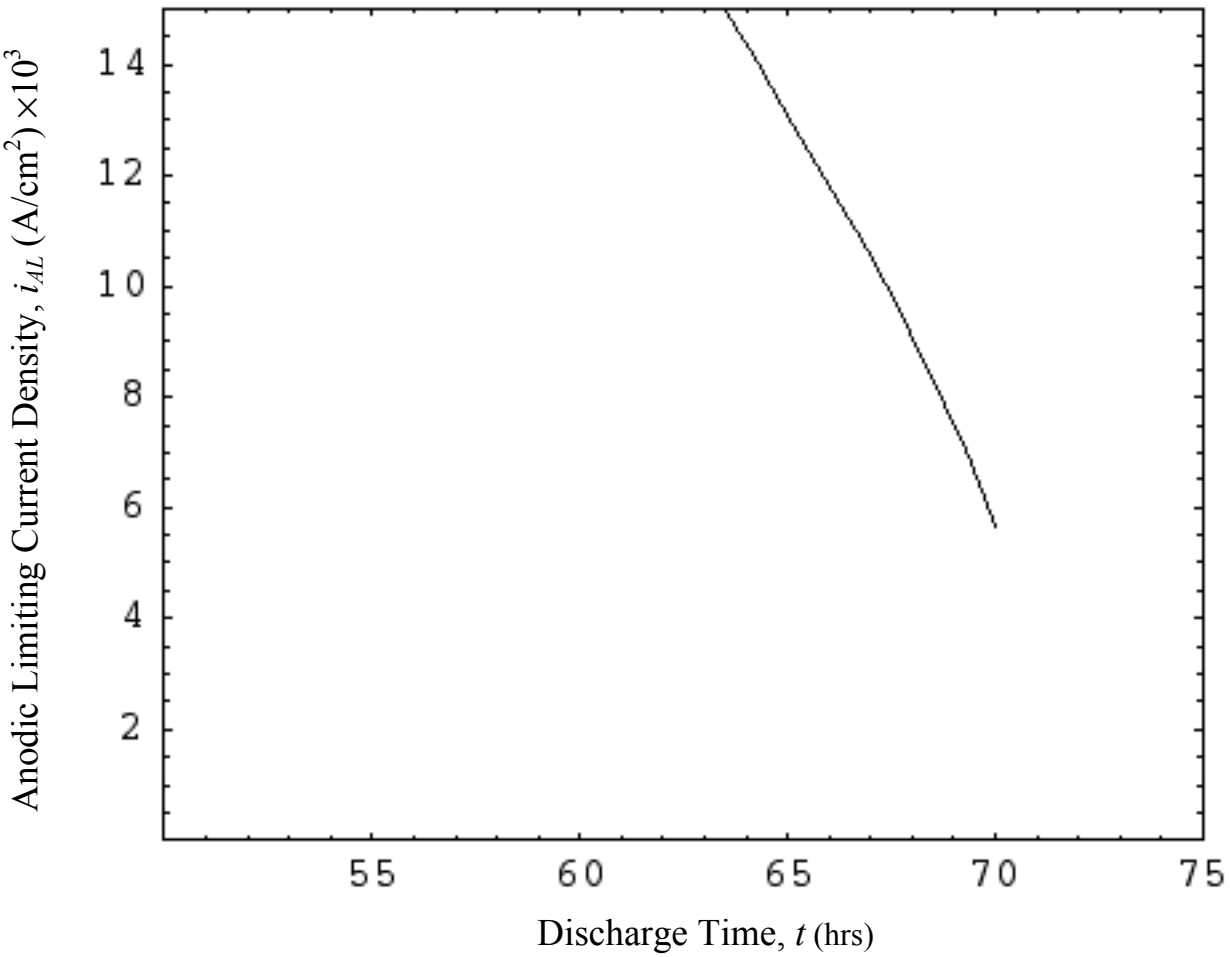

Figure V-8: Anodic limiting current density versus time for Size 13 Zn/Air cell at 4mA continuous discharge.

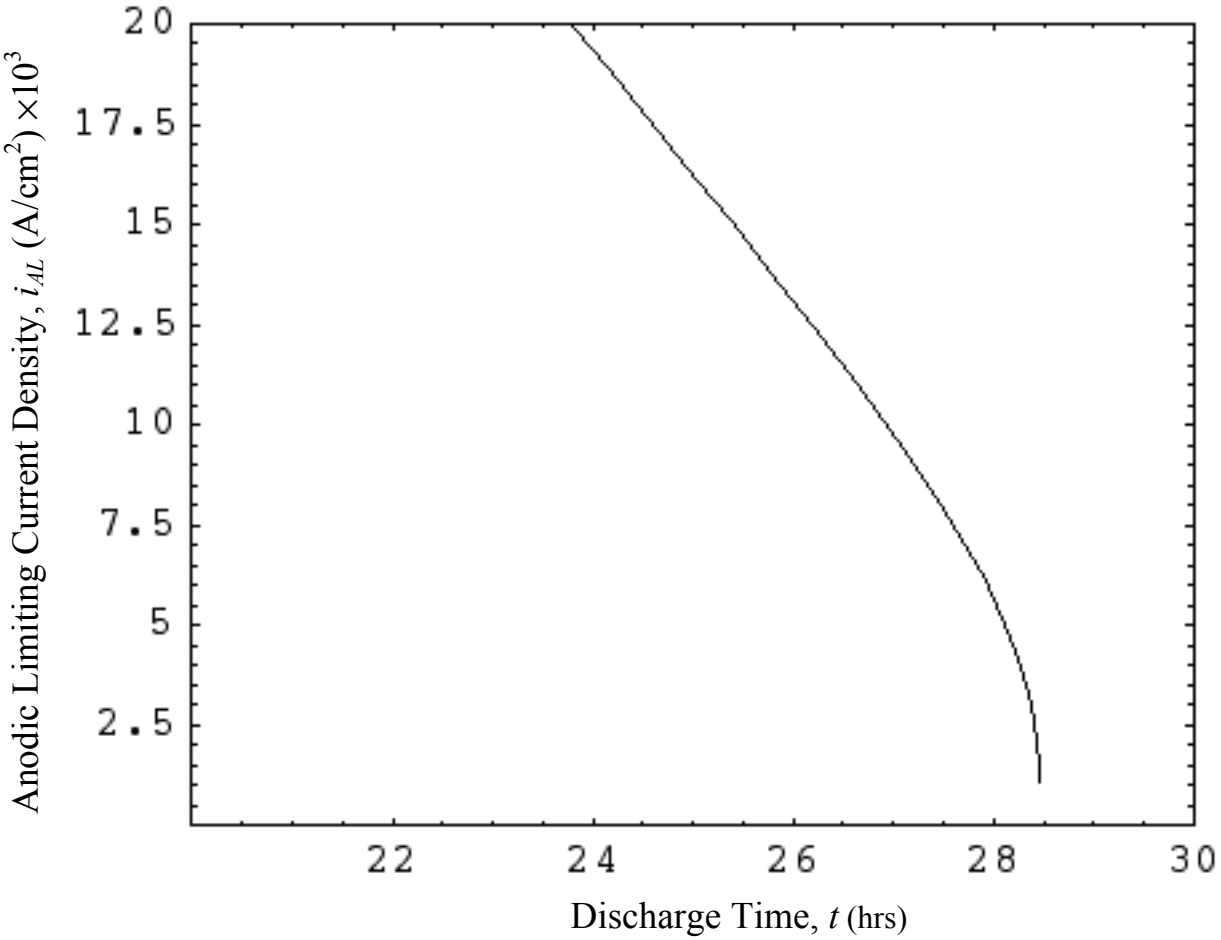

Figure V-9: Anodic limiting current density versus time for Size 13 Zn/Air cell at 10mA continuous discharge.

CROSS-SECTIONAL ANALYSES: ZINC MORPHOLOGY AND SPATIAL DISTRIBUTION

A key assumption that is utilized during the mathematical formula of the performance model is that non-discharged Zn access to free hydroxyl ions is not impeded by electrolyte diffusion limitations in the anode compartment. In other words, the model assumes that all resistance to diffusion in the anode compartment is accounted for in the separator area. If this assumption were truly valid, Zn utilization would be higher and uniform through out the anode chamber. Zn utilization would have a strong relation to primarily the anodic limiting current density. In addition, comparisons between the predicted performance models and those experimentally generated would be similar across all discharge currents investigated.

As discussed in this chapter, the experimental and model-based discharge curves did not exactly correlate. To further investigate this effect, cross-sectional analyses of the various discharged cells were completed in accordance with the procedure outlined in Chapter IV. These analyses were performed in hopes of gaining some insight in regards to physical aspects of discharged cells that may indicate deviation from predicted to actual performance results. Cross-section images of cells after discharge are included and discussed below.

Figure V-10 is a cross-sectional image of a Size 13 Zn/Air cell that was discharged under 1mA continuous current. Examination of this image shows a very high utilization of Zn. In this image, only a few non-discharged Zn particles are observed and they are located away from the separator. In addition, the formation of both Type I and Type II ZnO is seen. The high utilization of Zn that is indicated by this cross-section directly correlates with the high capacity indicated by discharge testing as well as the

predicted model results for the discharge current of 1mA. However, it is clear that there is some gradation in the direction perpendicular to the separator.

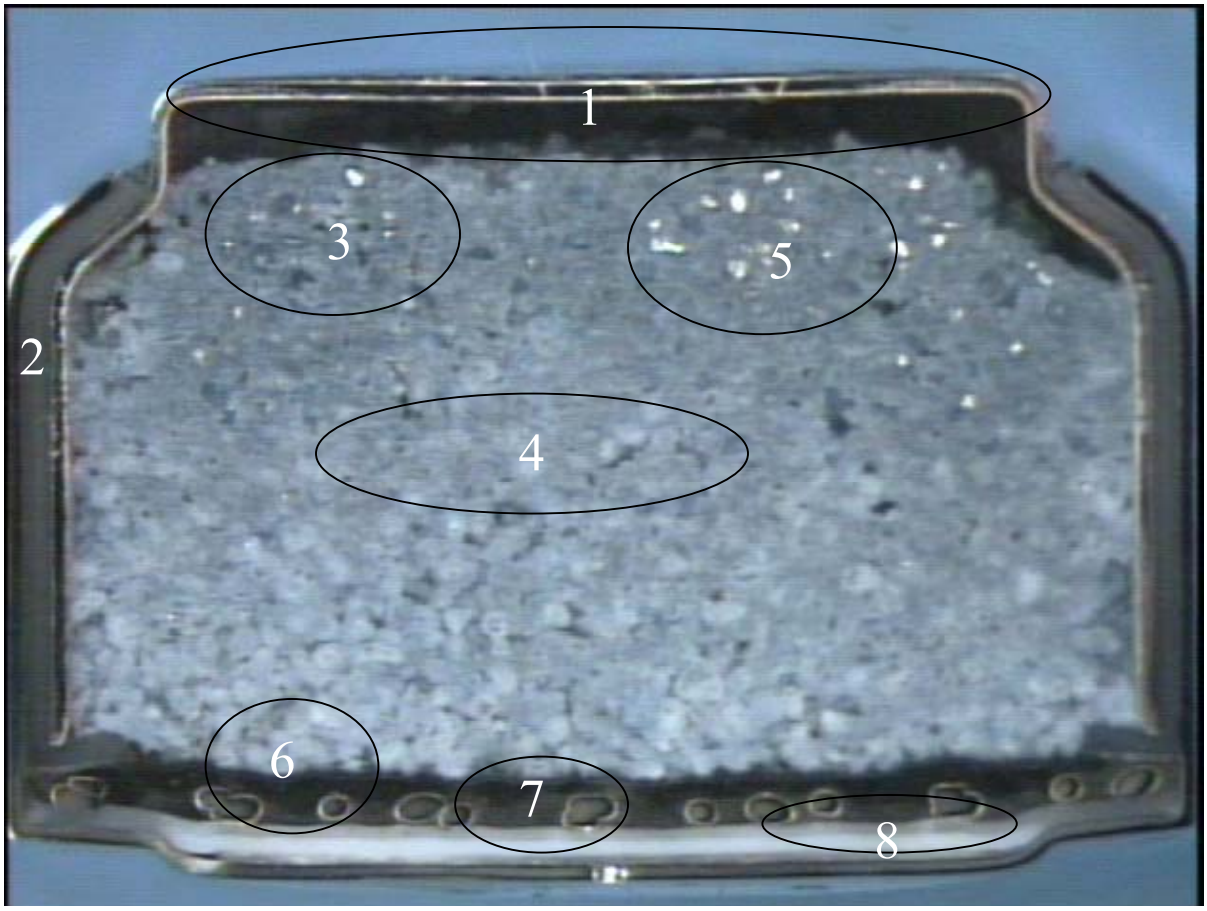

Figure V-10: Cross-sectional image of size 13 Zn/Air cell discharged at 1mA continuous current obtained via digital light microscopy.

Key for Figure V-10:

1. Headspace in cell available after cell discharge.
2. Nylon Grommet electrically insulating the anode can from the cathode can.
3. Type II discharged Zn particles.
4. Type I discharged Zn particles.
5. Non-discharged Zn particles.
6. Nickel mesh screen in cathode plaque assembly.
7. Loose PTFE layer in cathode plaque assembly.
8. Air diffusion membrane.

Figure V-11 is a cross-sectional image of a size 13 Zn/Air cell that was discharged under 4mA continuous current. Examination indicates a reduced utilization of Zn at this higher discharge current. This is evident with apparent increase in the number of non-discharged Zn particles. In addition, a discharge front that extends from the cathode plaque outward to the anode can is more evident. This is also accompanied by the apparent higher concentration of Type I discharged Zn particles and reduced concentration of Type II discharged Zn particles. The formation of Type I Zn particles during discharge is directly attributable to the reduction of capacity due to its higher density in comparison to Type II discharged Zn particles. As a layer of Type I film is formed on the separator, the ability for free OH^- to travel to unreacted Zn particles is reduced. As this layer continues to form during discharge, the cell will eventually be unable to produce a sufficient current to power a hearing instrument (or other device) and will cease to discharge. The anodic limiting current is reached quicker during the rapid formation of Type I discharged Zn particles due to the greater impedance of current and significant reduction of hydroxyl ion transport both through the ash layer surrounding individual Zn particles and through the anode compartment matrix. These observations would provide direct correlation to the experimental discharge data for 4mA constant current discharge. In addition, these observations indicate possible inadequacies associated with the assumption that hydroxyl ion access is uniform to all non-discharged Zn particles in the anode can. As this assumption becomes less valid at higher discharge currents, greater discrepancy between predicted and actual discharge performance arises. In addition, the void fraction between zinc particles is further reduced at higher discharge rates.

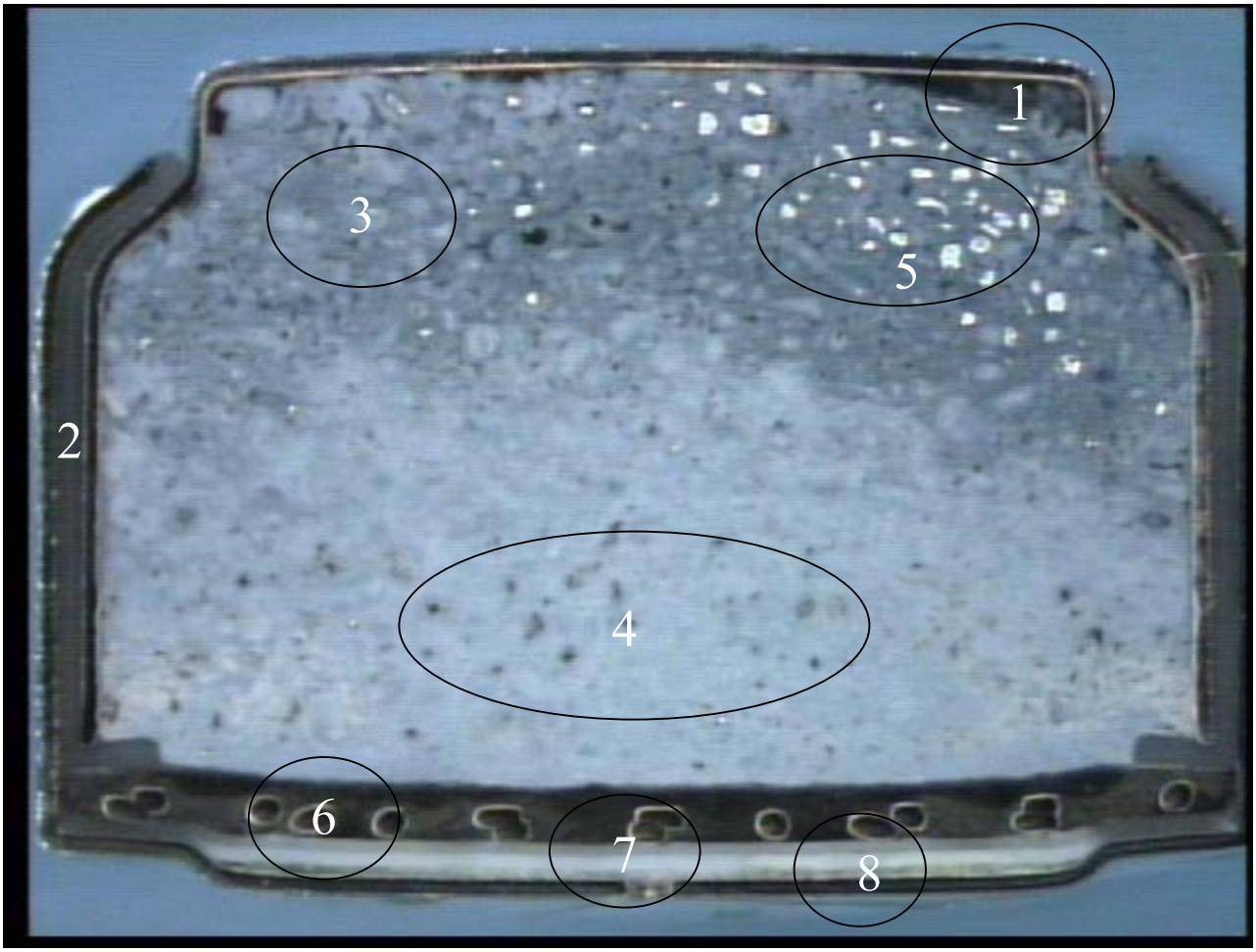

Figure V-11: Cross-sectional image of size 13 Zn/Air cell discharged at 4mA continuous current obtained via digital light microscopy.

Key for Figure V-11:

1. Headspace in cell available after cell discharge.
2. Nylon Grommet electrically insulating the anode can from the cathode can.
3. Type II discharged Zn particles.
4. Type I discharged Zn particles.
5. Non-discharged Zn particles.
6. Nickel mesh screen in cathode plaque assembly.
7. Loose PTFE layer in cathode plaque assembly.
8. Air diffusion membrane.

Figure V-12 is a cross-sectional image of a size 13 Zn/Air cell that was discharged under 10mA continuous current. Examination of the image shows a substantially higher proportion of non-discharged Zn particles in comparison to both Figures V-10 and V-11. In addition, the discharged Zn particles are virtually all Type I. As previously discussed, the formation of Type I discharged Zn particles has significant impact on the cell to provide capacity. The observations made via this image provide an explanation of the significantly reduced capacities at the discharge current of 10mA. In addition, this provides further evidence that the assumption of uniform hydroxyl ion access to non-discharged Zn particles is valid only at lower discharge currents.

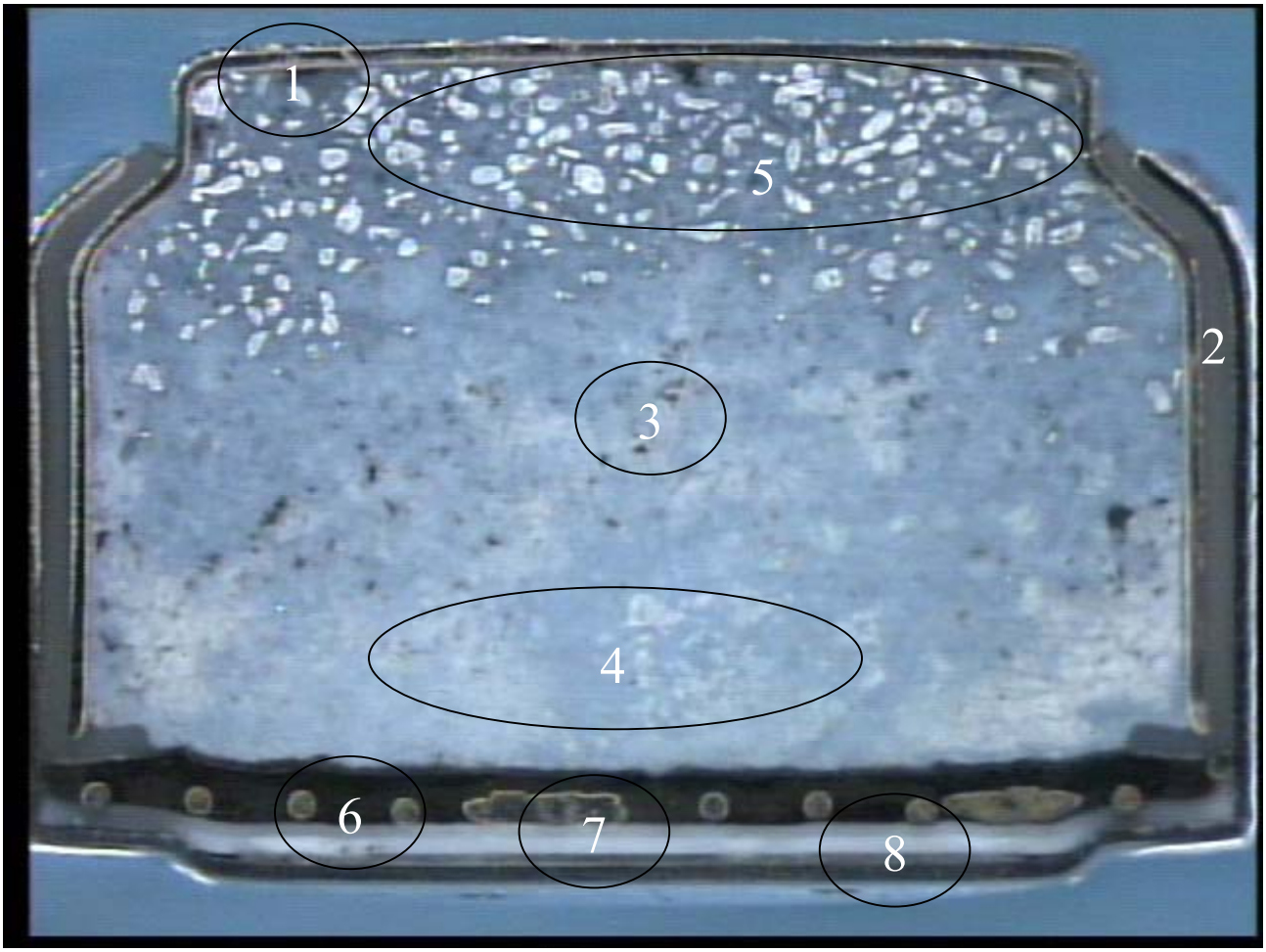

Figure V-12: Cross-sectional image of size 13 Zn/Air cell discharged at 10mA continuous current obtained via digital light microscopy.

Key for Figure V-12:

1. Headspace in cell available after cell discharge (virtually non-existent).
2. Nylon Grommet electrically insulating the anode can from the cathode can.
3. Type II discharged Zn particles.
4. Type I discharged Zn particles.
5. Non-discharged Zn particles.
6. Nickel mesh screen in cathode plaque assembly.
7. Loose PTFE layer in cathode plaque assembly.
8. Air diffusion membrane.

SEM ANALYSIS: ZINC PARTICLES AFTER 10mA CONTINUOUS DISCHARGE

SEM analyses were completed on the cross-sectioned cells previously discussed to gain further insight of cell discharge dynamics and evaluation of model assumptions. Examinations were conducted on non-discharged Zn particles and those of Type I ZnO along the separator and Figures V-13 through V-16 are representative SEM images of the analyses. To aid in discussion, call-outs of specific observations are included only in the higher magnification images (Figures V-14 and V-16).

Examination of Figures V-13 and V-14 shows that areas near unreacted Zn particles have higher void volumes. Although these observations are made on cross-sections of discharged cells, the same statement would hold true for a non-discharged cell. As the cell begins to discharge, the void fraction is further reduced in a time-dependent manner. The main contributor to this reduction is the formation of ZnO, which has a higher partial molar volume than Zn. The reduction of void fraction is more vividly illustrated in Figures V-15 and V-16, which are for sections along the separator. In these images, there is virtually zero void fraction available close to the separator. The occurrence of discharge states similar to these images prevent the further discharge of zinc and the cell stops to perform.

Examination of the Figures V-13 and V-14 also indicates the accuracy associated with the basic shrinking core model application. The non-reacted zinc core is clearly observed in both figures referenced. In addition, the formation of the ZnO film around the non-reacted zinc core is clearly visible. Figure V-14 indicates that the ZnO film is not consistently solid. That is, there are holes in the ZnO ring that would facilitate the transport of hydroxyl ions to the non-reacted Zn surface. As the reaction proceeds, the

ZnO film becomes more and more dense leading to the reduction of available areas for hydroxyl ions to penetrate and gain access to non-reacted Zn. This is illustrated in Figures V-15 and V-16. The ZnO surrounding the unreacted Zn core also appears separated from it. It is not clear is this is a result of the cross-sectional preparation described earlier. It is possible to get variations in the finished surface of the sample after polishing. In addition, the cross-sectioning technique only gives a representative snap-shot of a specific section of the overall diameter of the cell. It is possible that images gathered from other areas of the anode compartment may provide images indicating more uniform coating of the unreacted Zn.

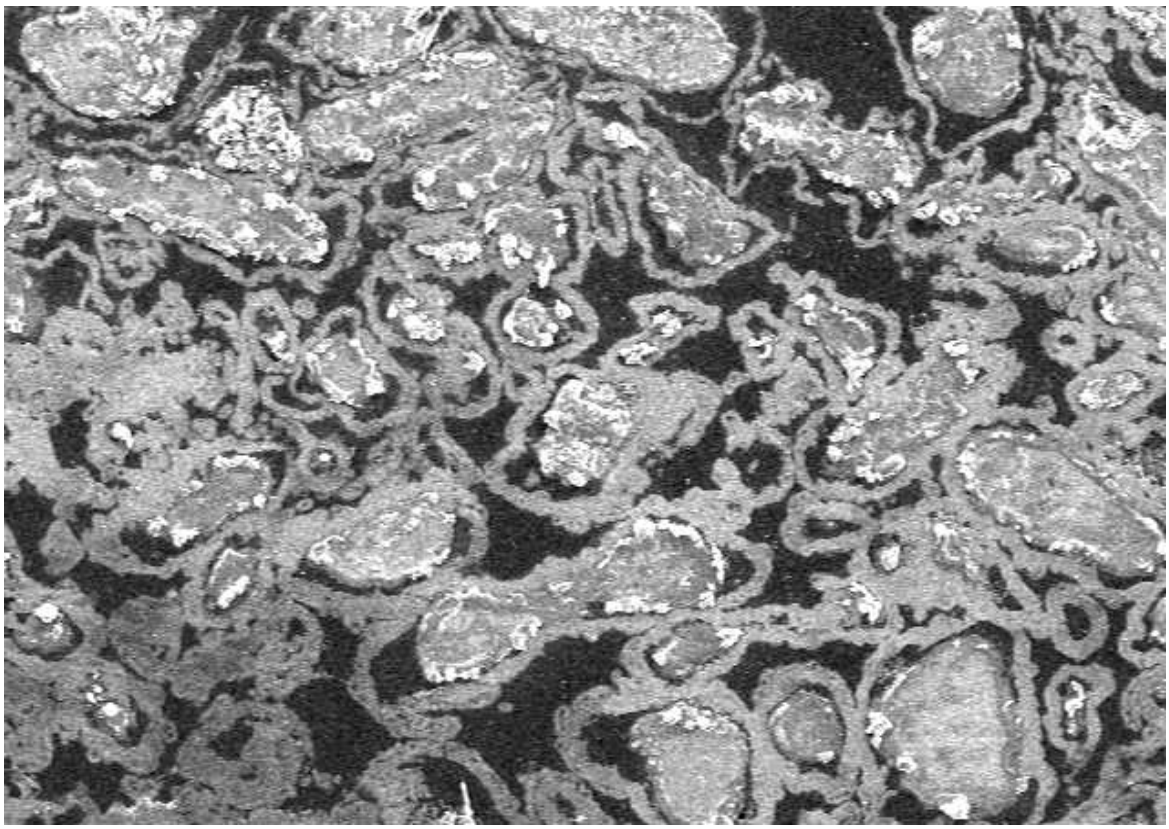

Figure V-13: SEM image at 100X magnification of low Zn utilization zone after 10mA continuous current discharge.

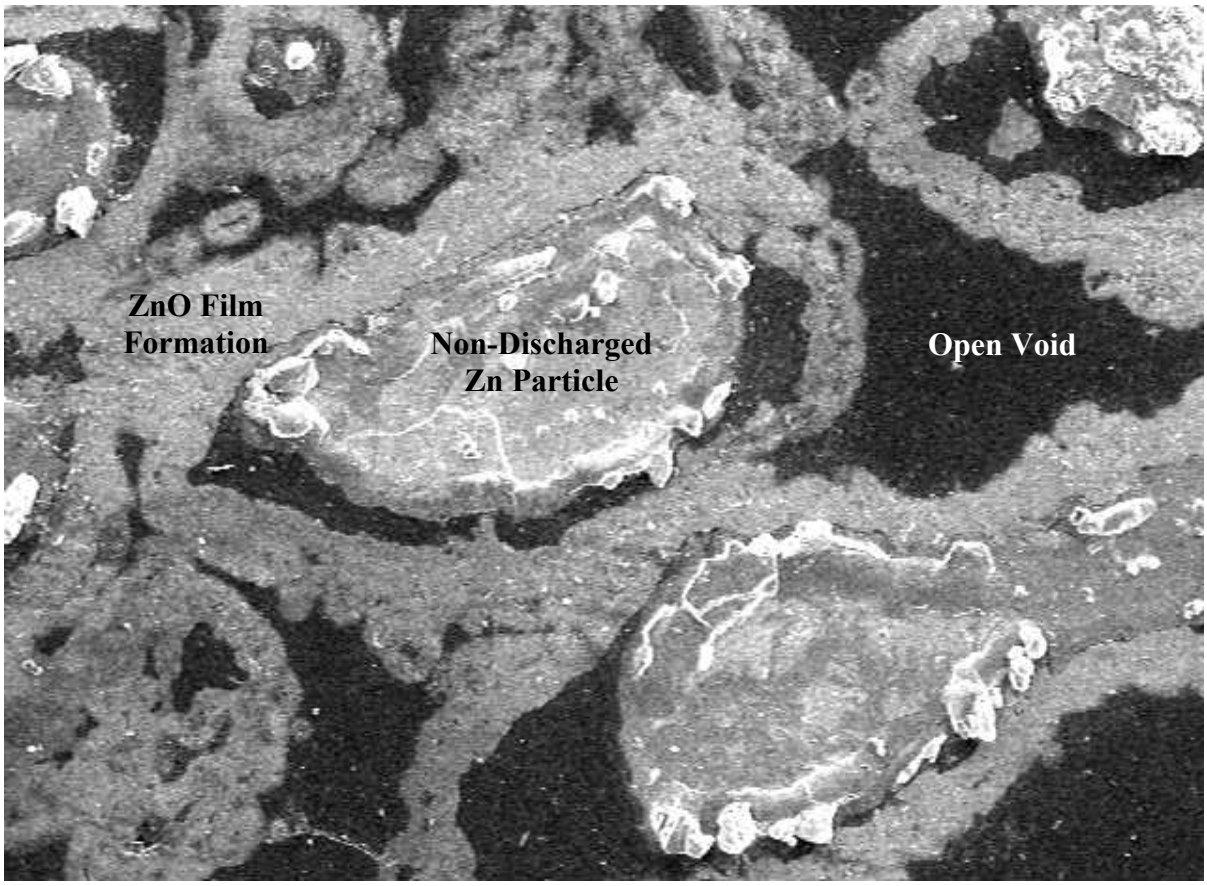

Figure V-14: SEM image at 332X magnification of low Zn utilization zone after 10mA continuous current discharge.

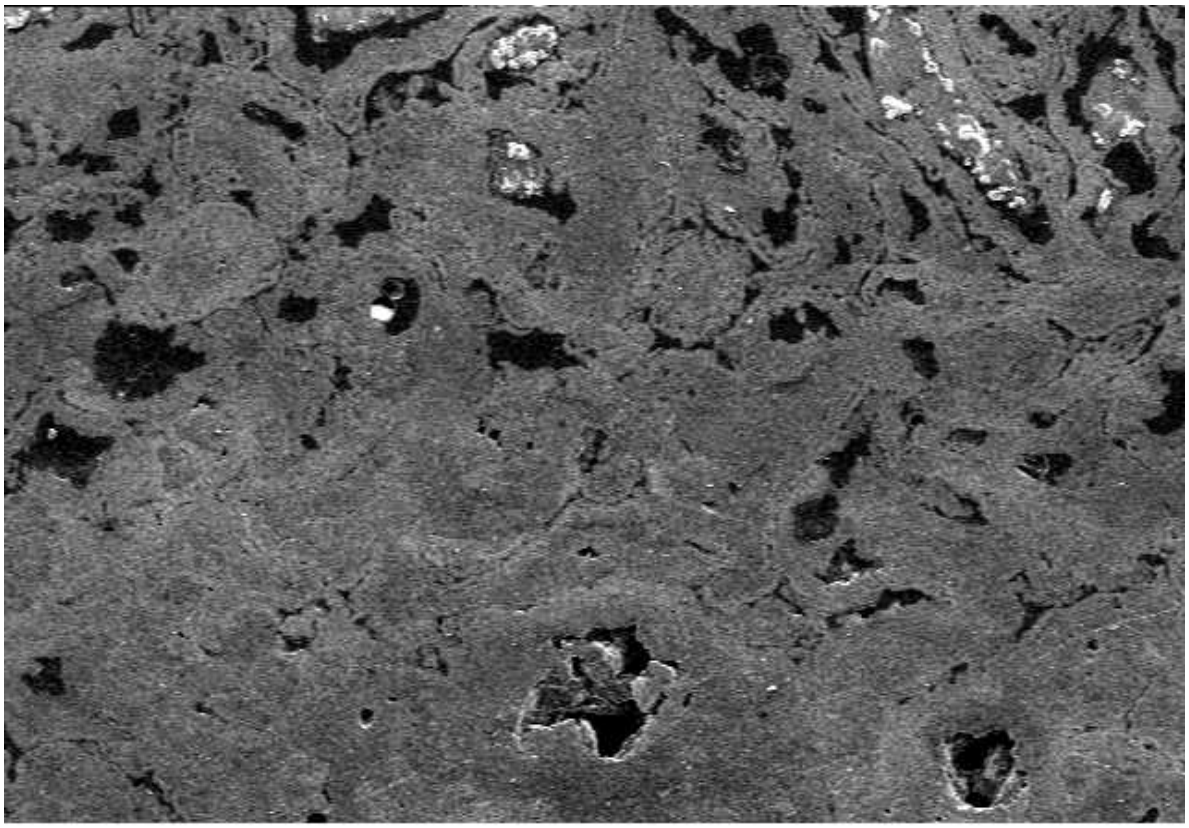

Figure V-15: SEM image at 100X magnification of discharged Zn along separator after 10mA continuous current discharge.

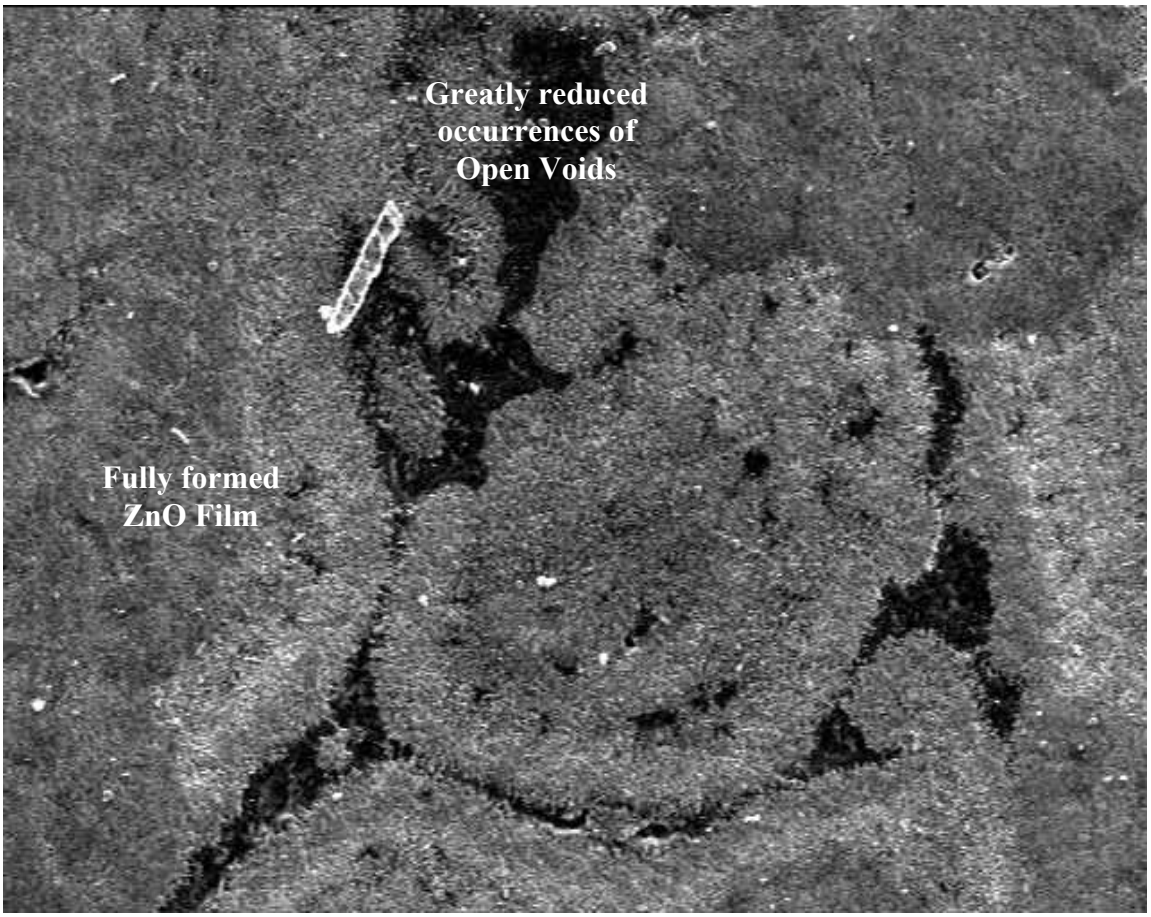

Figure V-16: SEM image at 960X magnification of discharged Zn along separator after 10mA continuous current discharge.

SEM ANALYSIS: CATHODE PLAQUE

SEM analysis was completed on a discharged cathode plaque, the result of which is included in Figure V-17. EDAX scans were completed on the cross-sectioned plaque to evaluate component distribution throughout the cathode assembly. The image includes four quadrants of analysis. The upper left-hand quadrant shows the completed EDAX scan for manganese (Mn). The lower left-hand quadrant shows the completed EDAX scan for fluorine (F), which is directly indicative of PTFE presence. The upper right-hand quadrant shows the completed EDAX scan for potassium (K), which is indicative of electrolyte penetration. The lower right-hand quadrant shows the EDAX scan region associated with all three aforementioned quadrants.

From Figure V-17, the Mn appears to be fairly well dispersed. The particle size, however, appears to be larger than what would be primarily desired. This observation would have detrimental impact on the cathode catalyst activity. As with catalysts in general, smaller particle sizes would have larger surface areas available for reaction assistance. In this case the overall efficiency of the Mn_XO_Y catalyst to catalyze peroxide produced in the cathode plaque during the reduction of oxygen would be lower.

The occurrence of F also appears to be fairly dispersed, leading to the conclusion that the PTFE is also fairly dispersed. This characteristic is key in both the binding of the carbon matrix as well as helping to control water transport during the cell discharge. This observation is qualitative statement of a bulk property. Examination of the carbon matrix at higher magnifications would lead to observations in regards to PTFE defibrillation. This is a key characteristics since an over defibrillated PTFE blend would not have consistent binding properties and lead to a poorly performing plaque.

The final observation of note in regards to Figure V-17 is the flooding of the cathode due to the observable level of potassium throughout the cell matrix. As previously mentioned, cathode flooding is one of the possible mechanisms for the ending of cell discharge. Under low current drains, the flooding of the plaque may occur at a lower rate due to the slower reduction of oxygen required to satisfy cell discharge. In this instance, the discharge of zinc will be the dominating reaction leading to the end of cell life. This was discussed earlier in this chapter during the discussion of the 1mA discharged cell. Under higher current drains, the flooding of the plaque plays a more significant role in the failure of the cell to continually provide the required current. The reduction of oxygen must occur at a faster rate in order to provide a useful current to the external device. This, in turn, can lead to a greater production of hydroxyl ions in the cathode plaque structure and a flooding condition being met sooner in discharge life.

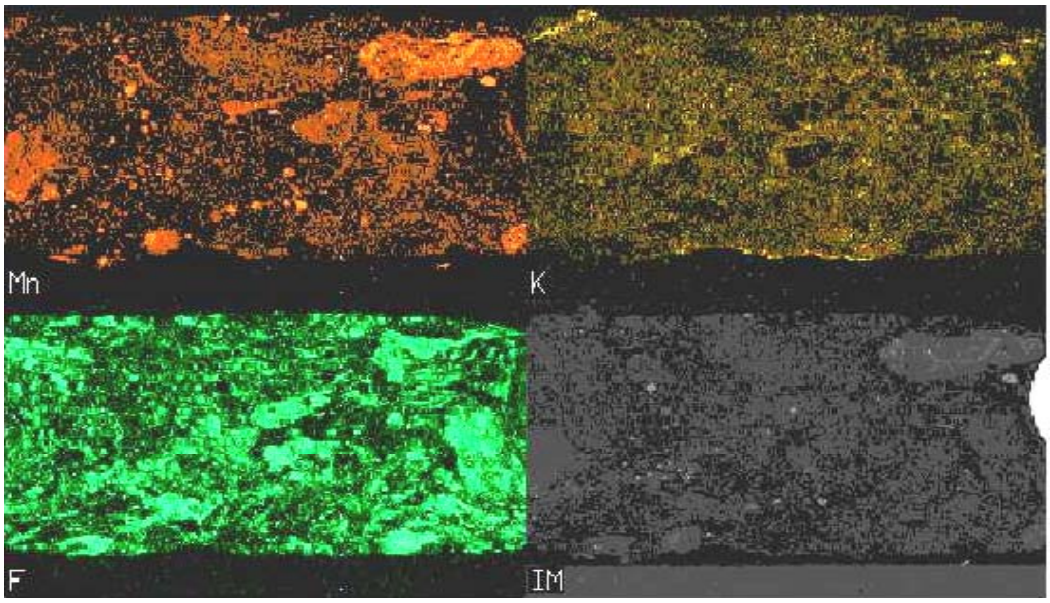

Figure V-17: SEM image at 100X magnification with EDAX analysis to determine the distribution of Mn, K, and F in the cathode plaque structure.

SEM ANALYSIS: ZINC PARTICLES

SEM analyses were completed on non-discharged Zn prior to cell assembly to gain insight into the physical characteristics of the zinc particles that are incorporated in the anode compartment and incorporated in Figures V-18 and V-19.

As evident by these images, the particles are oblong in shape and vary in particle size. The distribution of particle size prevents compact packing of the powder, which would lead to poor discharge results due to lack of pathways for OH^- diffusion. Significant gaps between particles associated with the particle size distribution is particularly evident in Figure V-19.

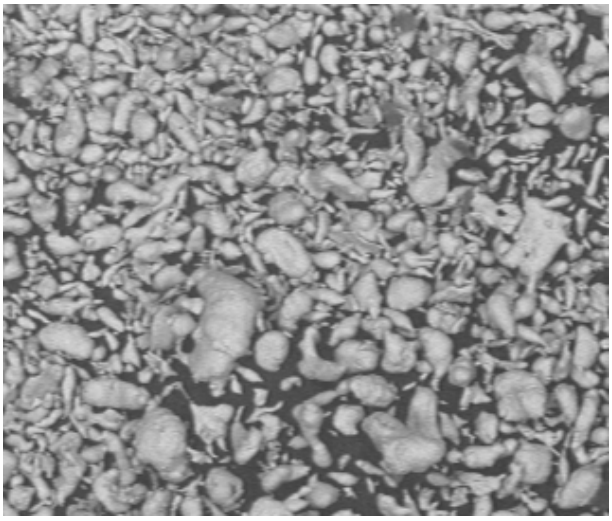

Figure V-18: SEM image at 100X magnification to evaluate physical appearance of Zn prior to discharge.

Figure V-19: SEM image at 1000X magnification to evaluate physical appearance of Zn prior to discharge.

CHAPTER VI
CONCLUSIONS
AND
RECOMMENDATIONS FOR FURTHER STUDY

CONCLUSIONS

In this thesis, the assembly, transport, and kinetic characteristics of a Zinc/Air (Zn/Air) primary cell were reviewed. From basic principles of operation for a Zn/Air primary cell and anodic and cathodic reaction assumptions supported via a literature, basic kinetic and transport expressions were developed for the anode, cathode, and electrolyte. The combination of these results leads to an overall formula for the cell polarization.

Based upon input parameters that were selected as a function of known cell design components, the literature review, and fitting, it is possible to evaluate the design of a Zn/Air cell. The predicted service life, polarization response, and anodic limiting current density were three parameters examined. As a result of modeling simulations, it was determined that the selection of the diffusion coefficient for OH^- within the ash layer played a significant role on the prediction of service life. The selection of the reference cathodic exchange current density had effect on the running voltage associated with the discharge curve. The overall slope of the discharge curve was impacted by the selection of the reference anodic exchange current density.

The simulations indicated excellent agreement with experimental results across a range of discharge currents (1mA, 4mA, and 10mA). The predicted service life for all discharge rates was within less than 0.5% of the experimental results. The most deviation occurred within the discharge slope at the highest discharge rate. This observation was

attributed to the assumptions associated with the development of the time-dependent anodic limiting current density.

RECOMMENDATIONS FOR FURTHER STUDY

The mathematical model developed in this study exhibits fairly good agreement with experimental data for continuous current discharge at 1mA, 4mA, and 10mA. However, there is some discrepancy with the respective performance predictions and also between model assumptions and evaluation of cross-sectioned cells. There are various ways in which this work can be expanded:

1) Carefully investigate the values of the parameters chosen and validate them independently through experimentation where possible.
2) The model proposed is a one-dimensional model. It accounts for diffusion, mass transport, and reaction kinetics in the radial direction of the Zn particles. To expand this work, diffusion limitations in the direction normal to the separator should also be investigated. Further change in the OH^- diffusivity in the anode chamber as void volume decreases should be included.
3) Incorporate in the model a parameter that accounts for the formation of the ZnO barrier along the separator. This would account for variations of discharge slope at high discharge currents (see Figure V-6) and could be simulated as an overpotential that is dependent upon discharge current density. Figure VI-1 is a modified image of the transport zones that would aid in visualization and definition for modeling incorporating barrier formation. This is an approximate

manner of accounting for OH^- diffusional limitations in the direction perpendicular to the separator.

4) This model assumes the direct oxidation of Zn to ZnO. As discussed in the thesis, zincate is an intermediate species that is formed. The formation of this species has an impact on the overall cell performance both in terms of the number of overall electrons involved in the reaction as well as the formation of the ZnO layer. This is not accounted for in this model and the exclusion of this likely impacts the overall accuracy of prediction for this model.

5) Directly account for the dynamic change in bulk transfer coefficient changes.

6) Include prediction of OH^- conductivity as a function of electrolyte concentration.

7) Account for the transient changes in electrolyte concentration.

8) Account for the effect of relative humidity (RH) and complete simulations using various RH and temperatures.

9) Investigate non-constant current discharge model, i.e., for a constant resistance or power.

10) Investigate non-constant discharge models, i.e., pulsed discharge current, resistance, or power.

11) Account for the diffusion of electrolyte into the cathode plaque over time. This phenomena eventually leads to flooding of the cathode plaque.

12) Adjust parameters in the model to determine an optimum cell.

13) Utilize the performance characteristics of various cell manufacturers to assess the design differences that may lead to performance and design improvements.

14) More careful investigation of the mechanism and kinetics of anode and cathode reactions must be made.

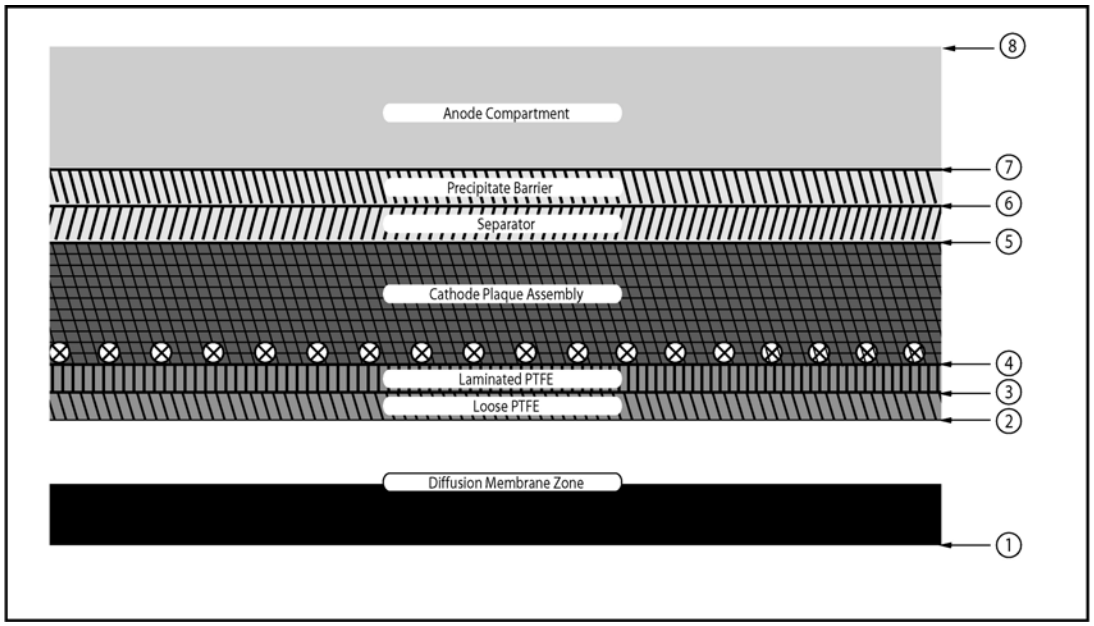

Figure VI-1: Defined transport regions for completion of modeling work incorporating barrier formation.

REFERENCES

1. S. Bender, J. Cretzmeyer, and T. Reise, *Handbook of Batteries*, 2nd ed., D. Linden, Editor, p. 13.1 - 13.5, McGraw-Hill, New York (1995).

2. W. G. Sunu, D. N. Bennion, "Transient and Failure Analysis of the Porous Zinc Electrode", *J. Electrochem. Soc.*, **127**, 2007-2016 (1980).

3. K. Kinoshita, *Electrochemical Oxygen Technology*, John Wiley and Sons, Inc., New York (1992).

4. Q. C. Horn and Y. Shao-Horn, "Morphology and Spatial Distribution of ZnO formed in Discharged Alkaline Zn/MnO_2 AA Cells", *J. Electrochem. Soc.*, **150**, A652-A658 (2003).

5. J. S. Fordyce and R. L. Baum, "Vibrational Spectra of Solutions of Zinc Oxide in Potassium Hydroxide", *J. Chem. Phys.*, **43**, 843 (1965).

6. G. H. Newman and G. E. Blomgren, "NMR Study of Complex Ions in the Aqueous ZnO-KOH System", *J. Chem. Phys.*, **43**, 2744 (1965).

7. R. W. Powers and M. W. Breiter, "The Anodic Dissolution and Passivation of Zinc in Concentrated Potassium Hydroxide Solutions", *J. Electrochem. Soc.*, **116**, 719-728 (1969).

8. R. W. Powers, "Film Formation and Hydrogen Evolution on the Alkaline Zinc Electrode", *J. Electrochem. Soc.*, **118**, 685-695 (1971).

9. S. U. Falk and A. Salkind, *Alkaline Storage Batteries*, p. 606, John Wiley and Sons, Inc, New York (1969).

10. E. Yeager, J. A. Molla, and S. Guta, "The Electrochemical Properties of Graphite and Carbon", *Proc. Electrochemical Society*, p. 132, **84-5** (1984).

11. R. E. Davis, G. L. Horvath, and C. W. Tobias, "The solubility and diffusion coefficient of oxygen in potassium hydroxide solutions", *Electrochemica Acta* **12**, 287-297 (1967).

12. G. Prentice, *Electrochemical Engineering Principles*, p. 159, Prentice Hall, New Jersey (1991).

13. J. Huot, "Advances in Zinc Batteries", Noranda Advanced Materials, 137-153.

14. J. Huot and E. Boubour, "Electrochemical performance of gelled zinc alloy powders in alkaline solutions, *J. Power Sources*, **65**, 81-85 (1997).

15. H. Yang, Y. Cao, X. Ai, and L. Xiao, "Electrochemical performance of gelled zinc alloy powders in alkaline solutions", *J. Power Sources*, **128**, 97-101 (2004).

16. C. Cachet, B. Saidani, and R. Wiart, "The Behavior of Zinc Electrodes in Alkaline Electrolytes - II. A Kinetic Analysis of Anodic Dissolution", *J. Electrochem. Soc.*, **139**, 644-655 (1992).

17. R. W. Powers, "Anodic Films on Zinc and the Formation of Cobwebs", *J. Electrochem. Soc.*, **116**, 1652-1658 (1969).

18. W. Glaeser, "Gas Evolution Data on Very-Low-Mercury-Content Zinc Powders for Alkaline Batteries", 265-296.

19. M. Meeus, Y. Strauven, and L. Groothaert, "New Developments in Reduction of Mercury Content in Zinc Powder For Alkaline Dry Batteries", 281-299.

20. H. Yoshizawa and A. Miura, "Mercury Free Alkaline Manganese Batteries", *Progress in Batteries and Battery Materials*, **12**, 132-139 (1993).

21. G. Che, B. B. Lakshmi, C. R. Martin, and E. R. Fisher, "Metal-Nanocluster-Filled Carbon Nanotubes: Catalytic Properties and Possible Applications in Electrochemical Energy Storage and Production", *Langmuir*, **15**, 750-758 (1999).

22. C. Y. Mak, H. Y. Cheh, G. S. Kelsey, and P. Chalilpoyil, "Modeling of Cylindrical Alkaline Cells - Part I. Quasi-Equilibrium Analysis", *J. Electrochem. Soc.*, **138**, 1607-1610 (1991).

23. C. Y. Mak, H. Y. Cheh, G. S. Kelsey, and P. Chalilpoyil, "Modeling of Cylindrical Alkaline Cells - Part II. Secondary Current Distribution", *J. Electrochem. Soc.*, **138**, 1611-1615 (1991).

24. J. Chen and H. Y. Cheh, "Modeling of Cylindrical Alkaline Cells - Part III. Mixed-Reaction Model for the Anode", *J. Electrochem. Soc.*, **140**, 1205-1213 (1993).

25. J. Chen and H. Y. Cheh, "Modeling of Cylindrical Alkaline Cells - Part IV. Dissolution-Precipitation Model for the Anode", *J. Electrochem. Soc.*, **140**, 1214-1218 (1993).

26. E. J. Podlaha and H. Y. Cheh, "Modeling of Cylindrical Alkaline Cells - Part V. High Discharge Rates", *J. Electrochem. Soc.*, **141**, 15-27 (1994).

27. E. J. Podlaha and H. Y. Cheh, "Modeling of Cylindrical Alkaline Cells - Part VI. Variable Discharge Rates", *J. Electrochem. Soc.*, **141**, 28-35 (1994).

28. E. J. Podlaha and H. Y. Cheh, "Modeling of Cylindrical Alkaline Cells - Part VII. Wound Cell Model", *J. Electrochem. Soc.*, **141**, 1751-1758 (1994).

29. Y. Zhang and H. Y. Cheh, "Modeling of Cylindrical Alkaline Cells - Part VIII. Solution of the Model by Exploiting Its Differential Algebra Equation Structure", *J. Electrochem. Soc.*, **146**, 850-856 (1999).

30. Y. Zhang and H. Y. Cheh, "Modeling of Cylindrical Alkaline Cells - Part IX. A Rigorous Mathematical Model for Sensitivity Analysis", *J. Electrochem. Soc.*, **146**, 3566-3570 (1999).

31. J. J. Kriegsmann and H. Y. Cheh, "The effect of cathode porosity on the performance of a cylindrical alkaline cell", *J. Power Sources*, **77**, 127-135 (1999).

32. J. J. Kriegsmann and H. Y. Cheh, "The effect of active material loading on the performance of a cylindrical alkaline cell", *J. Power Sources*, **79**, 262-270 (1999).

33. J. J. Kriegsmann and H. Y. Cheh, "The importance of the equilibrium zincate ion concentration in modeling a cylindrical alkaline cell", *J. Power Sources*, **84**, 52-62 (1999).

34. J. J. Kriegsmann and H. Y. Cheh, "A binary electrolyte model of a cylindrical alkaline cell", *J. Power Sources*, **84**, 114-125 (1999).

35. J. J. Kriegsmann and H. Y. Cheh, "The importance of the cathode specific interfacial area in modeling a cylindrical alkaline cell", *J. Power Sources*, **85**, 190-202 (1999).

36. Y. Zhang and H. Y. Cheh, "Random and uncertainty analysis of cylindrical alkaline cells", *J. Power Sources*, **87**, 174-185 (1999).

37. Y. Zhang and H. Y. Cheh, "A Two-Dimensional Mathematical Model of a Zn-MnO_2 Alkaline Cell", *Chinese Battery Industry Journal* (Dianchi Gongye), in press.

38. L. Pisani, M. Valentini, and G. Murgia, "Analytic Pore Scale Modeling of the Reactive Regions of Polymer Electrolyte Fuel Cells", *J. Electrochem. Soc.*, **150**, A1549-A1559 (2003).

39. T. Thampan, S. Malhotra, J. Zhang, and R. Datta, "PEM fuel cell as a membrane reactor", *Catalysis Today*, **67**, p. 15-32 (2001).

40. Z. Mao and R. E. White, "Mathematical Modeling of a Primary Zinc/Air Battery", *J. Electrochem. Soc.*, **139**, 1105 (1992).

41. A. J. Appleby and J. Marie, "Kinetics of Oxygen Reduction on Carbon Materials in Alkaline Solution", *Electrochemica Acta*, **24**, pp. 195-202 (1979).

42. E. Yeager, J. A. Molla, and S. Guta, "The Electrochemical Properties of Graphite and Carbon", *Proc. Electrochemical Society*, p. 132, **84-5** (1984).

43. T. Thampan, Ph.D. Dissertation*, Design and Development of Higher Temperature Membranes for PEM Fuel Cells*, Worcester Polytechnic Institute, May 2003.

44. S. Murkerjee, S. Shrinivasan, "Enhanced electrocatalysis of oxygen reduction on platinum alloys in proton exchange membrane fuel cells", *J. Electroanal. Soc.*, **357**, 201-224 (1993).

45. H. S. Fogler, *Elements of Chemical Reaction Engineering*, p. 582-587, Prentice Hall, New Jersey (1992).

46. Personal notes of Dr. Huk Cheh, February 1997.

47. E. Yeager, "Dioxygen Electrocatalysis: Mechanisms in Relation to Catalytic Structure", *J. Molecular Catalysis*, **38**, 5-25 (1986).

48. J. Meyers, M. Doyle, R. Darling, and J. Newman, "The Impedance Response of a Porous Electrode Composed of Intercalation Particles", *J. Electrochem. Soc.*, **147**, 2930-2940 (2000).

49. Y. Sato, M. Takahashi, H. Asakura, T. Yoshida, K. Tada, and K. Kobayakawa, "Gas evolution behavior of Zn alloy powder in KOH solution", *J. Power Sources*, **38**, 317-325 (1992).

50. E. D. Farmer and A. H. Webb, "Zinc passivation and the effect of mass transfer in flowing electrolyte", *J. Applied Electrochem.*, **2**, 123-136 (1972).

51. T. P. Dirske, "Electrode Migration and Reaction Processes Occurring In Alkaline-Zinc Batteries", Technical Report AFAPL-TR-69-90, Air Force Aero Propulsion Laboratory, Wright-Patterson Air Force Base, 1969.

52. P. Vanysek, *CRC Handbook of Chemistry and Physics*, 73rd Edition, D. Linde Ed., 8-21 - 8-31, CRC Press, Boca Raton (1993).

53. J. Bockris, Z. Nagy, and A. Danjanovic, "On the Deposition and dissolution of Zinc in Alkaline Solutions", *J. Electrochem. Soc.*, **119**, 285-295 (1972).

54. N. A. Hampson, G. A. Herdman, and R. Taylor, "Some Kinetic and Thermodynamic Studies of the System Zn/OH", *J. Electrochem. Soc.*, **25**, 9-18 (1970).

55. C. Cachet, V. Stroder, and R. Wiart, "The Kinetics of the Zinc Electrode in Alkaline Zincate Solutions", *Electrochemica Acta*, **27**, 903-908 (1982)

56. M. Liu, G. M. Cook, and N. P. Yao, "Transient Current Distributions in Porous Zinc Electrodes in KOH Electrolytes", *J. Electrochem. Soc.*, **129**, 239-246 (1982).

57. M. J. Isaacson, F. R. McLarnon, and E. J. Cairns, "Current Density and ZnO Precipitation-Dissolution Distribution in Zn-ZnO Porous Electrodes and Their Effect on Material Redistribution: A Two-Dimensional Mathematical Model", *J. Electrochem. Soc.*, **137**, 2014-2020 (1990).

58. M. E. H. Assad and Tuula Noponen, "Performance Characteristics of Porous Air Electrodes", Helsinki University of Technology, Laboratory of Applied Thermodynamics, 1-40 (1995).

59. *Lange's Handbook of Chemistry*, 14th Edition, J. Dean Ed., McGraw-Hill Inc, New York (1992).

APPENDIX
MATHEMATICA PROGRAMING CODE FOR 1mA, 4 mA, and 10mA DISCHARGE SIMULATION

```
<< Graphics`Graphics`

<<Graphics`MultipleListPlot`

(*INCLUDE EFFECT OF ASH LAYER EXPANSION*)

$TextStyle={FontSize->16};
(*EQUATIONS*)

v=v0-etaA+etaC-etaB-i RI;

etaB=i (LB/s0 tr1); (*tr1 = transference no.*)

etaA=R T/(alphaA F) ArcSinh[(i/(2 iA0))/(1-i/iAL)];

etaC=-R T/(alphaC F) ArcSinh[(i/(2 iC0))/(1-i/iCL)];

iAL= (gMA) 2 F P1D C1B;

iCL=4 F P3E C3S;

iA0=(\[Xi]A)^2 (gMA) (C1B/C1Bref) Exp[-EA/1.987 (1/T-1/Tref)] iA0ref;

iC0= (gMC) (C3S/C3Sref) Exp[-EC/1.987 (1/T-1/Tref)] iC0ref;

gMA= mMA SMA;

gMC= mMC SMC;

SMA=3/(rhoMA RMA);

SMC=3/(rhoMC RMC);

(*permeability of anode ash film, cm/s*)
P1D=
  K1D D1D \[Xi]A/(RMA(1-\[Xi]A)); (*1 =
    OH*)

(*permeability of O2, cm/s*)
P3E=K3E D3E/LE;(*3 = O2*)

\[Xi]A= (1- qA)^(1/3);

QmaxA = 2 (mMA/rhoMA)(F/ViA);

 qA= (t i)/QmaxA;     (*qA=Qt/QmaxA*)
```

```
tmaxA= QmaxA/(3600 i) ;

mMA=LA \[Epsilon]MA rhoMA;

mMC=LC \[Epsilon]MC rhoMC;

t=t1 3600;

i=i1/1000;

(*Diffusion of O2 thr GDL, cm2/s*)
          D3E=(1-qwC)^1.5*D3G;

qwC=0.0;

D3G=1/D3Ginv;

\!\(\(D3Ginv =
      pN2\/D\_\(13  e\) +
        pW\/D\_\(12  e\) + \(1\/D\_k1e\) \((\(1 + \(B\_0\/\[Eta]\) \
\((pN2\/D\_k3e + pW\/D\_k2e)\)\)\/\(1 + \(B\_0\/\[Eta]\) \((pO\/D\_k1e + \
pW\/D\_k3e + pN2\/D\_k2e)\)\))\);\)\)

\!\(\(\( (*\ Parameter\ Values*) \)\(\n\)\(D\_\(13  e\) = D\_\(31  e\);
  D\_\(12  e\) = D\_\(21  e\); D\_\(32  e\) = D\_\(32  e\);\)\)\)

\!\(\(\( (*Values\ of\ Diffusion\ Coefficients\ pD \((atm\ cm2/
           s)\)*) \)\(\n\)\(\(D\_\(12  e\) = K1*0.37\ \((T/353)\)^1.823;\)\n
  \(D\_\(13  e\) = K1*0.279\ \((T/353)\)^1.823;\)\n
  \(D\_\(23  e\) = K1*0.387\ \((T/353)\)^1.823;\)\)\)\)\)

\[Eta]=1.6 10^-10 (*viscosity of air at T =80C (atm s)*);

(*mean free speed*)
(*O2*)
MWO2=32;
v1=(8*82.06*T/((22/7)*MWO2))^0.5;

MWH2O=18;
v2=(8*82.06*T/((22/7)*MWH2O))^0.5;

MWN2=28;
v3=(8*82.06*T/((22/7)*MWN2))^0.5;

\!\(\(D\_k1e = K1*2/3*ap*v1;\)\)
```

\!\(\(D_k2e = K1*2/3*ap*v2;\)\)

\!\(\(D_k3e = K1*2/3*ap*v3;\)\)

\!\(\(B_0 = K1*\((ap^2)\)/8;\)\)

\!\(\(K1 = \[Epsilon]\/\[CapitalGamma];\)\)

(*pore size*)
ap=1.065(10^-4) (* cm*);

\[Epsilon]=0.5;

\[CapitalGamma]=1/(\[Epsilon])^.5;

pW=Exp[11.676-3816.44/(T-46.13)];

C3S=pO/(82.057 T);

pO=xO (pS-pW);

pN2=(1-xO)(pS-pW);

(*PARAMETERS*)

D1D= 0.5 10^(-8); (*Diff of OH in ash layer*)

K1D=1;

K3E=(82.057 T)/H3;

H3=1.33 10^6 Exp [-666/T];

RMA = 1.25 10^(-2);

RMC = 1.5 10^(-7);

\[Epsilon]MA = 0.3436; (*Vol fraction of Zn in anode*)

\[Epsilon]MC = 0.1765; (*Vol fraction of Carbon*)

rhoMA = 7.14;

mMC=1.13 10^-2;(*mass of Carbon/cm2*)

```
rhoMC=1.8; (*density of XC-72*)

xO=0.21;

pS=1.0;

C3Sref=3.4 10^(-6);

ViA = 9.16;

C1B=8 10^-3;

C1Bref=8 10^-3;

v0=1.654;

R=8.3143;

F=9.6487 10^4;

s0=0.45; (*S/cm*)

tr1 = 0.78;

Tref=293;

LB=1.016 10^(-2);

LA=3.233 10^(-1); (*75% of Anode Can Height*)

LC=3.556 10^(-2); (*Catalyst Layer Thickness*)

LE=2 10^(-2);

iC0ref= 1.0 10^(-11);

iA0ref= 1.0 10^(-4);

EA=4300;  (*Activation Energy, used for simulations with temperature variation*)

EC=4300; (*Activation Energy, used for simulations with temperature variation*)

alphaA=1/2;

alphaC=1/2;
```

T=293;

RI= 0.0;

1mA Discharge Simulation

i1=1.0/0.438; (*mA/cm2*)

Discharge Plot
Plot[v, {t1, 1, 284.21},
PlotRange->{{0, 300}, {0, 1.6}},
Frame->True, AspectRatio->0.8]

Anodic Limiting Current Density Plot
Plot[iAL 1000, {t1, 250, 285},
PlotRange->{{250, 300}, {0, 15}},
Frame->True, AspectRatio->0.8]

Data Importation
datamat=ReadList["1mA Discharge - Average.txt",Number,RecordLists\[Rule]True]

average=ListPlot[datamat,PlotRange\[Rule]{{0,300}, {0,1.6}},Frame\[Rule]True,
  AspectRatio\[Rule]0.8,PlotJoined\[Rule]True,
  PlotStyle\[Rule]Dashing[{0.02}]];

Combined Discharge Plot
combined=Show[average,
  Plot[v,{t1,1,284.21},PlotRange\[Rule]{{0,300},{0,1.6}},Frame\[Rule]True,
    AspectRatio\[Rule]0.8]]

Polarization Plot for 50% Discharge
t1=tmaxA/2;

Plot[v, {i1, 0,4.52},
PlotRange->{{1 10^-7, 5}, {0, 1.6}},
Frame->True, AspectRatio->0.8]

4mA Discharge Simulation

i1=4.0/0.438; (*mA/cm2*)

Discharge Plot
Plot[v, {t1, 1, 67.945},
PlotRange->{{0, 80}, {0, 1.6}},
Frame->True, AspectRatio->0.8]

Anodic Limiting Current Density Plot
```
Plot[iAL 1000, {t1, 50, 70},
PlotRange->{{50, 75}, {0, 15}},
Frame->True, AspectRatio->0.8]
```

Data Importation
```
datamat=ReadList["4mA Discharge - Average.txt",Number,RecordLists\[Rule]True]

average=ListPlot[datamat,PlotRange\[Rule]{{0,80},{0,1.6}},Frame\[Rule]True,
    AspectRatio\[Rule]0.8,PlotJoined\[Rule]True,
    PlotStyle\[Rule]Dashing[{0.02}]];
```

Combined Discharge Plot
```
combined=Show[average,
   Plot[v,{t1,1,67.945},PlotRange\[Rule]{{0,80},{0,1.6}},Frame\[Rule]True,
    AspectRatio\[Rule]0.8]]
```

10mA Discharge Simulation

```
i1=10.0/0.438; (*mA/cm2*)
```

Discharge Plot
```
Plot[v, {t1, 1, 22.885},
PlotRange->{{0, 25}, {0, 1.6}}, FrameLabel->{"Time, h", "V"},
Frame->True, AspectRatio->0.8]
```

Anodic Limiting Current Density Plot
```
Plot[iAL 1000,{t1,20,30},PlotRange\[Rule]{{20,30},{0,20}},Frame\[Rule]True,
  AspectRatio\[Rule]0.8]
```

Data Importation
```
datamat=ReadList["10mA Discharge - Average.txt",Number,
   RecordLists\[Rule]True]

average=ListPlot[datamat,PlotRange\[Rule]{{0,25},{0,1.6}},Frame\[Rule]True,
    AspectRatio\[Rule]0.8,PlotJoined\[Rule]True,
    PlotStyle\[Rule]Dashing[{0.02}]];
```

Combined Discharge Plot
```
combined=Show[average,
   Plot[v,{t1,1,22.85},PlotRange\[Rule]{{0,25},{0,1.6}},Frame\[Rule]True,
    AspectRatio\[Rule]0.8]]
```

Combined Simulated Discharge Plot
```
Show[%91, %99,%106]
```

Polarization Curve for 25% Discharge

```
t1=tmaxA/4;

Plot[v, {i1, 0,34.12},
PlotRange->{{1 10^-7, 40}, {0, 1.6}},
Frame->True, AspectRatio->0.8]
```